Effect of Nonuniform Seismic Input on Arch Dams

Thesis by
Paul Scott Nowak

In Partial Fulfillment of the Requirements
for the Degree of
Doctor of Philosophy

California Institute of Technology
Pasadena, California
1989
(Submitted September 21, 1988)

Acknowledgements

I would like to thank my advisor and friend, John Hall, for being the mentor I hope to be. His endless help, motivation and guidance will always be appreciated.

I would also like to thank my wife, Linda, for her unending patience, love and friendship.

Finally, I would like to thank the members of the 1988 SOPS championship softball team; Gary Balas, Bill Donlon, Craig Monroe, Linda Nowak,
Sy Shimabukuro, M.P. Sitlington, Don Wassink, Kris Wood, and Laurie Wood. Their friendship these last four years will never be forgotten.

Abstract

Standard earthquake analyses of civil engineering structures use uniform ground motions even though considerable variations in both amplitude and phase can occur along the foundation interface for long-span bridges and large dams. The objective of this thesis is to quantify the effect that these nonuniformities have on the structural response.

The nonuniform, free-field motions of the foundation interface are assumed to be caused by incident plane body waves. The medium in which these waves travel is a linear, elastic half-space containing a canyon of uniform cross section in which the structure is placed. The solutions for the free-field motions that are due to incident SH, P and SV waves are calculated using the boundary element method.

An analysis of Pacoima (arch) dam located near Los Angeles, California, is performed for both uniform and nonuniform excitations. The important effect of nonuniformities in the free-field motions, sometimes leading to a decrease in the dam response and sometimes to an increase, is quantified.

Contents

List of Figures

List of Tables

Chapter 1

Introduction

Seismic analyses of civil engineering structures typically use uniform, free-field motions at the foundation interface as the earthquake loading. However, significant variations in amplitude and phase can occur along the interface if its spatial extent is large; this is certainly true for long-span bridges and large dams. The objective of this thesis is to quantify the effect that these nonuniformities have on the response of concrete arch dams.

The state of the art in computing the earthquake response of a three-dimensional dam assumes uniform, free-field motions and employs a finite block of foundation rock, usually assumed massless, which is fixed at its far boundary. Omission of foundation mass eliminates the artificial foundation modes that arise from the finite extent of the foundation and that may tend to dominate the response. Foundation radiation damping can be included approximately in such a representation through equivalent damping ratios assigned to the modes of the dam-water-foundation system [10] or through equivalent hysteretic damping assigned to the dam [19]. More rigorous mathematical treatment of dam-foundation interaction would include the foundation mass and would either provide transmitting boundaries to prevent reflected waves or extend the foundation mesh far enough from the dam to allow travelling waves to be absorbed by material damping. However, construction of accurate transmitting

boundaries for complicated, three-dimensional canyon geometries is beyond the current state of the art, and extension of the foundation mesh for wave absorption is computationally infeasible.

In addition to the foundation interaction problem, a remaining important task is to define and incorporate a realistic, nonuniform free-field input. The few instances where motions at points near the interface between the dam and foundation were recorded during an earthquake indicate that the motion is far from uniform, more so for the higher frequency components [26,24,6,28,27,25,1,35,8,7]. (Note that the relative amounts of variation present in the free-field motion and due to dam-foundation interaction are unknown.) Only a few analytical studies employing nonuniform input to the dam have been reported : [40,14,11] for two-dimensional systems and [5,14,45,9,46] for three-dimensional arch dams. All agree that nonuniformity in seismic input is important. Also of concern is nonuniform seismic input to the water. A few studies have been made with two-dimensional systems, using variations of the ground motion in the direction of the stream [39,29,21]. Again, significant effects are noted.

Only references [45,9,46] mentioned above represent serious studies for arch dams. However, the reduction in the dam response in [45] caused by an incident wave excitation compared to uniform excitation seemed rather excessive, and studies [9] and [46], which showed larger stresses that were due to nonuniform seismic input, considered only phase variations in the free-field motions because of the time lag of the travelling wave. Further, neither [45] nor [46] considered reservoir water, and [45] employed only excitations in the stream direction. Thus, further investigation of the effects of nonuniform seismic input is needed.

In this study, a frequency domain investigation into the effects of nonuniform

earthquake excitation on the linear response of a three-dimensional arch dam-water-foundation system (Pacoima dam) is performed. The analysis consists of two parts. First, the free-field motions of the canyon walls are obtained by the direct boundary element method after making some simplifying assumptions about the canyon geometry and the earthquake mechanism. In the second part of the analysis, the frequency domain response of the dam-water-foundation system is computed by the finite element method, using the previously determined free-field excitations. To quantify the effect of nonuniform seismic input more concisely, the frequency domain responses are converted into the time domain in the form of standard deviations of the response to a random input with an earthquake-like frequency content.

Details of the finite element analysis of the dam-water-foundation system are presented in Chapter 2. Then, Chapter 3 describes the boundary element procedure for calculating the free-field motions that are due to incident SH, P and SV waves. Frequency and time domain responses for Pacoima dam near Los Angeles, California, for various incident waves are presented in Chapter 4. Conclusions and recommendations for future work follow in Chapter 5.

Chapter 2

Formulation for Linear Dam Response

2.1 Basic Equations

A desirable way to specify the earthquake input to a structure is through free-field motions, i.e., those motions that would occur in the foundation during the earthquake if the structure were not present. Such a specification is valid if no nonlinearity occurs outside the structure. The structure response can be obtained by superposing two solutions as shown in Figure 2.1. The presence of water, as for a dam, is discussed later.

In the first problem (problem 1), the earthquake occurs with the structure disconnected from the foundation (so that the foundation moves at the free-field motions with a traction-free surface), and the structure is subjected to a special set of body forces and surface tractions defined so that the surface that was connected to the foundation also moves at the free-field motions. In the second problem (problem 2), in which the structure and foundation are joined together, the structure is subject to the negative of the body forces from problem 1 as well as to a line load applied along the foundation interface equal to the negative of the surface tractions from problem 1. Superposition of problems 1 and 2 leaves the incident wave on the structure-foundation system with no body forces on the structure and with continuous displacements and

tractions across the foundation interface. Note that if the free-field motions are not uniform, then the first solution involves nonzero strains in the structure, and, thus, this superposition procedure can not be used in the case of a nonlinear structure.

The requirements for problem 1, that the foundation interface of the structure move at the free-field motions, can be satisfied in an infinite number of ways. However, the most convenient one avoids the solution of a dynamic problem and is known as the pseudo-static solution (denoted by superscript S1) obtained from

$$\begin{bmatrix} K_{dd} & K_{di} \end{bmatrix} \begin{Bmatrix} u_d^{S1}(t) \\ u_i^{S1}(t) \end{Bmatrix} = \{0\}, \tag{2.1}$$

where $[K]$ = the stiffness matrix of the structure (say, from a finite element discretization) partitioned into degrees of freedom off (subscript d) and on (subscript i) the foundation interface, $\{u^{S1}(t)\}$ = nodal displacement vector containing the specified free-field motions $\{u_i^{ff}(t)\}$ in $\{u_i^{S1}(t)\}$; i.e.,

$$\{u_i^{S1}(t)\} = \{u_i^{ff}(t)\}, \tag{2.2}$$

and t = time. Note that only the upper partitioned part of $[K]$ appears in Equation 2.1. $\{u_d^{S1}(t)\}$ is computed as

$$\{u_d^{S1}(t)\} = -[K_{dd}]^{-1}\,[K_{di}]\,\{u_i^{ff}(t)\}. \tag{2.3}$$

The set of special forces applied to the structure in problem 1 can be obtained by inserting $\{u^{S1}(t)\}$ into the matrix equation of motion of the structure :

$$\begin{Bmatrix} f_d^{S1}(t) \\ f_i^{S1}(t) \end{Bmatrix} = \begin{bmatrix} K_{dd} & K_{di} \\ K_{di}^T & K_{ii} \end{bmatrix} \begin{Bmatrix} u_d^{S1}(t) \\ u_i^{S1}(t) \end{Bmatrix} + \begin{bmatrix} C_{dd} & C_{di} \\ C_{di}^T & C_{ii} \end{bmatrix} \begin{Bmatrix} \dot{u}_d^{S1}(t) \\ \dot{u}_i^{S1}(t) \end{Bmatrix} + \begin{bmatrix} M_{dd} & M_{di} \\ M_{di}^T & M_{ii} \end{bmatrix} \begin{Bmatrix} \ddot{u}_d^{S1}(t) \\ \ddot{u}_i^{S1}(t) \end{Bmatrix}, \tag{2.4}$$

where $[C]$ and $[M]$ are the structure's damping and mass matrices. Neglecting the small damping term and employing Equations 2.2 and 2.3 reduces Equation 2.4 to

$$\begin{Bmatrix} f_d^{S1}(t) \\ f_i^{S1}(t) \end{Bmatrix} = \begin{bmatrix} 0 & 0 \\ K_{di}^T & K_{ii} \end{bmatrix} \begin{Bmatrix} u_d^{S1}(t) \\ u_i^{ff}(t) \end{Bmatrix} + \begin{bmatrix} M_{dd} & M_{di} \\ M_{di}^T & M_{ii} \end{bmatrix} \begin{Bmatrix} \ddot{u}_d^{S1}(t) \\ \ddot{u}_i^{ff}(t) \end{Bmatrix}. \quad (2.5)$$

In problem 2, the special forces of Equation 2.5 are removed from the dam-foundation system. Thus,

$$\begin{bmatrix} K_{dd} & K_{di} & 0 \\ K_{di}^T & K_{ii}+\tilde{K}_{ii} & \tilde{K}_{if} \\ 0 & \tilde{K}_{if}^T & \tilde{K}_{ff} \end{bmatrix} \begin{Bmatrix} u_d^2(t) \\ u_i^2(t) \\ u_f^2(t) \end{Bmatrix} + \begin{bmatrix} C_{dd} & C_{di} & 0 \\ C_{di}^T & C_{ii}+\tilde{C}_{ii} & \tilde{C}_{if} \\ 0 & \tilde{C}_{if}^T & \tilde{C}_{ff} \end{bmatrix} \begin{Bmatrix} \dot{u}_d^2(t) \\ \dot{u}_i^2(t) \\ \dot{u}_f^2(t) \end{Bmatrix} +$$

$$\begin{bmatrix} M_{dd} & M_{di} & 0 \\ M_{di}^T & M_{ii}+\tilde{M}_{ii} & \tilde{M}_{if} \\ 0 & \tilde{M}_{if}^T & \tilde{M}_{ff} \end{bmatrix} \begin{Bmatrix} \ddot{u}_d^2(t) \\ \ddot{u}_i^2(t) \\ \ddot{u}_f^2(t) \end{Bmatrix} = -\begin{Bmatrix} f_d^{S1}(t) \\ f_i^{S1}(t) \\ 0 \end{Bmatrix}, \quad (2.6)$$

where the $(\tilde{\ })$ denotes matrix quantities associated with the foundation region, and the subscript f refers to foundation degrees of freedom off the structure-foundation interface. For an infinite domain, $[\tilde{K}_{ff}]$, $[\tilde{C}_{ff}]$ and $[\tilde{M}_{ff}]$ could include terms representing a transmitting boundary. However, because such treatments are difficult for the three-dimensional canyon geometries associated with dams, only the stiffness of the foundation is included here $\left([\tilde{C}], [\tilde{M}] = [0]\right)$. Actually, foundation radiation effects are also approximately included as mentioned later. Such treatment has not prevented good agreement from being obtained in correlations with forced vibration test data on a number of concrete arch dams [15,32,31,33]. Omission of $[\tilde{C}]$ and $[\tilde{M}]$ at this stage allows the f degrees of freedom to be condensed out, and Equation 2.6 reduces to

$$\begin{bmatrix} K_{dd} & K_{di} \\ K_{di}^T & K_{ii}+\tilde{K}_{ii} \end{bmatrix} \begin{Bmatrix} u_d^2(t) \\ u_i^2(t) \end{Bmatrix} + \begin{bmatrix} C_{dd} & C_{di} \\ C_{di}^T & C_{ii} \end{bmatrix} \begin{Bmatrix} \dot{u}_d^2(t) \\ \dot{u}_i^2(t) \end{Bmatrix} +$$

$$\begin{bmatrix} M_{dd} & M_{di} \\ M_{di}^T & M_{ii} \end{bmatrix} \begin{Bmatrix} \ddot{u}_d^2(t) \\ \ddot{u}_i^2(t) \end{Bmatrix} = -\begin{Bmatrix} f_d^{S1}(t) \\ f_i^{S1}(t) \end{Bmatrix}, \tag{2.7}$$

where $[\bar{K}_{ii}]$ is the foundation stiffness matrix condensed to the interface degrees of freedom, localized to preserve the bandedness of the matrices [13].

If foundation interaction is not included, then the "i" equations in Equations 2.5 and 2.7 drop out, and the free-field displacements affect only the pseudo-static component of the solution ; i.e., they do not appear on the right hand side of the dynamic problem ("d" equations of Equation 2.7). This situation is desirable because it enables the effect of the uncertainties in the free-field displacements, which may be significant if they are obtained by integrating accelerograms, to be kept track of more easily. To accomplish this when foundation interaction is included, decompose $\{u^2(t)\}$ into another pseudo-static part, $\{u^{S2}(t)\}$, and the remaining (dynamic) part, $\{u^D(t)\}$, as

$$\{u^2(t)\} = \{u^{S2}(t)\} + \{u^D(t)\}. \tag{2.8}$$

This pseudo-static part is computed from

$$\begin{bmatrix} K_{dd} & K_{di} \\ K_{di}^T & K_{ii} + \bar{K}_{ii} \end{bmatrix} \begin{Bmatrix} u_d^{S2}(t) \\ u_i^{S2}(t) \end{Bmatrix} = \begin{bmatrix} 0 & 0 \\ K_{di}^T & K_{ii} \end{bmatrix} \begin{Bmatrix} u_d^{S1}(t) \\ u_i^{ff}(t) \end{Bmatrix}, \tag{2.9}$$

where the right hand side is the displacement term in Equation 2.5. The pseudo-static solution

$$\{u^S(t)\} = \{u^{S1}(t)\} + \{u^{S2}(t)\} \tag{2.10}$$

can be interpreted as the response of a massless structure to the earthquake with foundation interaction included. Substitution of Equation 2.5 into Equation 2.7 and

using Equations 2.8, 2.9 and 2.10 results in

$$\begin{bmatrix} K_{dd} & K_{di} \\ K_{di}^T & K_{ii} + \bar{K}_{ii} \end{bmatrix} \begin{Bmatrix} u_d^D(t) \\ u_i^D(t) \end{Bmatrix} + \begin{bmatrix} C_{dd} & C_{di} \\ C_{di}^T & C_{ii} \end{bmatrix} \begin{Bmatrix} \dot{u}_d^D(t) \\ \dot{u}_i^D(t) \end{Bmatrix} + \begin{bmatrix} M_{dd} & M_{di} \\ M_{di}^T & M_{ii} \end{bmatrix} \begin{Bmatrix} \ddot{u}_d^D(t) \\ \ddot{u}_i^D(t) \end{Bmatrix} = -\begin{Bmatrix} f_d^S(t) \\ f_i^S(t) \end{Bmatrix}, \tag{2.11}$$

where

$$\begin{Bmatrix} f_d^S(t) \\ f_i^S(t) \end{Bmatrix} = \begin{bmatrix} M_{dd} & M_{di} \\ M_{di}^T & M_{ii} \end{bmatrix} \begin{Bmatrix} \ddot{u}_d^S(t) \\ \ddot{u}_i^S(t) \end{Bmatrix}, \tag{2.12}$$

and where a damping term has been neglected from the right hand side.

The total solution is obtained as

$$\{u(t)\} = \{u^S(t)\} + \{u^D(t)\} \tag{2.13}$$

from Equations 2.2, 2.3, 2.9, 2.10 and 2.11-2.12.

The formulation for the response of a dam with water in contact with the upstream face also employs a superposition of pseudo-static and dynamic components. Earthquake loading to the dam and water is again expressed in terms of free-field motions, defined as those occurring with both the dam and water absent. The pseudo-static response $\{u^S(t)\}$ of the dam is taken to be that from Equations 2.2, 2.3, 2.9 and 2.10, which were derived without water. The associated response of the water is that due to the motion $\{u^S(t)\}$ along the boundary at the dam and to the earthquake excitation of the reservoir floor and sides; it is a dynamic response computed considering interaction between the water and foundation, which, however, is assumed not to affect the free-field motions at the dam-foundation interface. The dynamic component of the dam response is generated by removing the applied forces in the pseudo-static solution. As a simplification for the dynamic problem, interaction be-

tween the dam and the water through the foundation is neglected (following [23,22]); this neglect is consistent with the above assumption in the pseudo-static solution.

To include water compressibility, a frequency domain solution is most convenient. In the frequency domain, to obtain a response $r(t)$ to an excitation $p(t)$, the Fourier components of $r(t)$, defined as

$$r(\omega) = \int_{-\infty}^{\infty} r(t)\, \exp(i\omega t)\, dt, \tag{2.14}$$

where ω = frequency, are obtained frequency by frequency from the Fourier transform of the equations of motion. The right side of these equations contains the Fourier components of $p(t)$, defined as

$$p(\omega) = \int_{-\infty}^{\infty} p(t)\, \exp(i\omega t)\, dt. \tag{2.15}$$

The function $r(\omega)$ is transformed to the time domain by

$$r(t) = \frac{1}{2\pi} \int_{-\infty}^{\infty} r(\omega)\, \exp(-i\omega t)\, d\omega. \tag{2.16}$$

The Fourier components of the dam response are obtained by superposing pseudo-static and dynamic solutions

$$\{u(\omega)\} = \{u^S(\omega)\} + \{u^D(\omega)\}. \tag{2.17}$$

The pseudo-static solution $\{u^S(\omega)\}$ is frequency dependent since $\{u_i^{ff}(\omega)\}$ is, and is found from

$$\{u^S(\omega)\} = \{u^{S1}(\omega)\} + \{u^{S2}(\omega)\} \tag{2.18}$$

$$\{u_d^{S1}(\omega)\} = -[K_{dd}]^{-1}[K_{di}]\{u_i^{ff}(\omega)\} \tag{2.19}$$

$$\{u_i^{S1}(\omega)\} = \{u_i^{ff}(\omega)\} \tag{2.20}$$

$$\begin{bmatrix} K_{dd} & K_{di} \\ K_{di}^T & K_{ii} + \bar{K}_{ii} \end{bmatrix} \begin{Bmatrix} u_d^{S2}(\omega) \\ u_i^{S2}(\omega) \end{Bmatrix} = \begin{bmatrix} 0 & 0 \\ K_{di}^T & K_{ii} \end{bmatrix} \begin{Bmatrix} u_d^{S1}(\omega) \\ u_i^{ff}(\omega) \end{Bmatrix}. \tag{2.21}$$

The forces required to constrain the dam motion during the earthquake to the pseudo-static motion $\{u^S(\omega)\}$ are

$$\{f^S(\omega)\} = -\omega^2[M]\{u^S(\omega)\} - \{R^S(\omega)\} - \{R^C(\omega)\}, \tag{2.22}$$

where a viscous term has been omitted and where $-\omega^2\{u^S(\omega)\}$ is the Fourier transform of $\{\ddot{u}^S(t)\}$; $\{R^S(\omega)\}$ = vector of water forces on the dam generated by the pseudo-static accelerations $-\omega^2\{u^S(\omega)\}$ of the dam (water-foundation interaction included); and $\{R^C(\omega)\}$ = similar vector generated by the free-field accelerations at the reservoir floor and sides (stationary dam, water-foundation interaction included). Removal of the forces $\{f^S(\omega)\}$ from the dam-water-foundation system produces the dynamic response $\{u^D(\omega)\}$ of the dam from the solution of

$$\begin{bmatrix} K_{dd} - i\omega C_{dd} - \omega^2 M_{dd} - \omega^2 \hat{M}_{dd}(\omega) & K_{di} - i\omega C_{di} - \omega^2 M_{di} - \omega^2 \hat{M}_{di}(\omega) \\ K_{di}^T - i\omega C_{di}^T - \omega^2 M_{di}^T - \omega^2 \hat{M}_{di}^T(\omega) & K_{ii} + \bar{K}_{ii} - i\omega C_{ii} - \omega^2 M_{ii} - \omega^2 \hat{M}_{ii}(\omega) \end{bmatrix}$$

$$\begin{Bmatrix} u_d^D(\omega) \\ u_i^D(\omega) \end{Bmatrix} = -\begin{Bmatrix} f_d^S(\omega) \\ f_i^S(\omega) \end{Bmatrix}, \tag{2.23}$$

where $[\hat{M}(\omega)]$ is the frequency dependent, added mass matrix of the water.

Computational details for $[\hat{M}(\omega)]$, $\{R^S(\omega)\}$ and $\{R^C(\omega)\}$ follow [22,23], which employ a finite element discretization of the pressure wave equation for the water. A transmitting boundary is used at the upstream end of the water mesh to represent an infinite reservoir, and a partially absorbing boundary based on one-dimensional wave propagation is applied along the reservoir floor and sides to approximately model water-foundation interaction. Also, the response $\{u^D(\omega)\}$ is expressed in terms of eigenvectors of the dam-foundation system (generalized coordinates), which are assigned appropriate values of modal damping to represent viscous effects as well as foundation radiation. Thus, the damping matrix $[C]$ in Equation 2.23 need not

be formed. The added mass matrix $[\hat{M}(\omega)]$ is computed directly for the generalized coordinates.

2.2 Free-field Motions

The free-field motions are assumed to result from plane body waves incident to the canyon at various angles. For an actual canyon geometry and an arbitrary angle of incidence, solution for the free-field motions would be very difficult. Therefore, for simplicity, it is further assumed that the canyon is straight and of unvarying cross section and that the incident waves propagate normal to the axis of the canyon. These assumptions reduce the free-field problem to a two-dimensional one (Figure 2.2). Thus, incident SH waves produce the stream component of the excitation, and incident P and SV waves produce the perpendicular components, vertical and cross-stream. No variations in the free-field motions in the direction of the stream result from this procedure; any must be arbitrarily imposed.

Solution of the free-field problem is carried out by the direct boundary element method in an infinite two-dimensional half-space as described in Chapter 3. A frequency domain solution is employed. While foundation mass was omitted in section 2.1, it is, of course, included in the free-field problem.

In order to assess the effect of nonuniformity in the free-field motions on the dam response, the case of uniform free-field motion is also examined. This requires that some calibration be performed between the uniform excitation and the incident wave excitation, which is accomplished using a half-space with a horizontal free-surface (Figure 2.3). The motion used for the uniform excitation case, which is applied as a free-field motion everywhere along the canyon, approximately coincides with that occurring at point Q in Figure 2.3 (at the intersection of the canyon centerline and the

horizontal free surface) due to the incident wave in the calibration half-space. Thus, account is taken of reflections of the incident waves. For the results presented in Chapter 4, six excitations are employed as listed in Table 2.1: three for stream motion (U-S, SH0 and SH60) and three for cross-stream-vertical motion (U-CV, SVP0 and P60) where the vertical motion is approximately half that of the cross-stream. A single specification of ground motion (scaled amplitude-wise according to the factors given in the table) is used for all stream motions, the horizontal and vertical components of case U-CV, the P and SV waves in case SVP0, and the P wave in case P60. With reference to the calibration half-space, it would have been desirable to impart different frequency contents to the horizontal and vertical components of motion, but this is not possible for an excitation like P60, where a single incident wave produces both components, so no differences were employed.

2.3 Time domain results

To establish results in the time domain, the time history of the excitation (incident wave or uniform, free-field motion) is specified and transformed into the frequency domain. For the incident wave excitation, the free-field problem is then solved frequency by frequency as described in Chapter 3 to produce the free-field motions at the canyon surface. Once the frequency domain responses of the dam are computed by the procedures of Section 2.1, they are transformed to the time domain by Equation 2.16. Since the resulting responses of the dam will be sensitive to the frequency characteristics of the time history chosen for the excitation, a number of analyses for different time histories may have to be performed before some "average" features of the response become apparent. To avoid this process, the standard deviation (σ_r) over time of some response $r(t)$, which for the problem being solved has a zero mean,

is computed. The formula employed is based on

$$\sigma_r = \left(\int_{-\infty}^{\infty} |H_r(\omega)|^2 \, S(\omega) \, d\omega \right)^{\frac{1}{2}}, \tag{2.24}$$

where $H_r(\omega)$ is the transfer function (the Fourier transform $r(\omega)$ of the response divided by Fourier transform $p(\omega)$ of the excitation), and $S(\omega)$ is the power spectral density function for a stationary time history.

To impart earthquake-like frequency characteristics to the excitation, $S(\omega)$ is taken to be proportional to $|F(\omega)|^2$, where $|F(\omega)|$ is the modulus of the average Fourier transform of horizontal ground motion on rock near a magnitude 7.5 earthquake, as taken from [37] (Figure 2.4). The function $|F(\omega)|$ represents the frequency distribution of the excitation (incident SH, P, SV waves or uniform, free-field motions); no distinction other than amplitude is made for horizontal and vertical components of the excitation, as mentioned in Section 2.2. Thus,

$$\sigma_r = \left(\int_{-\infty}^{\infty} |H_r(\omega)|^2 \, C \, |F(\omega)|^2 d\omega \right)^{\frac{1}{2}}, \tag{2.25}$$

where C = the constant of proportionality between $S(\omega)$ and $|F(\omega)|^2$ and is taken as

$$C \; = \; 1 \, / \, (2 \, \pi \, T_{eq}) \tag{2.26}$$

where T_{eq} is the duration of the earthquake motion.

Case	Type	Wave	Angle of Incid.	Dir. of Motion	Amplitude of Uniform Excitation or Incident Wave	Surface Amplitude of Incident Wave with Reflection
U-S	uniform	–	–	S	1	–
SH0	incident	SH	0°	S	$\frac{1}{2}$	1
SH60	incident	SH	−60°	S	$\frac{1}{2}$	1
U-CV	uniform	–	–	C,V	−1 (C), $\frac{1}{2}$ (V)	–
SVP0	incident	SV,P	0°	C,V	$-\frac{1}{2}$ (SV), $\frac{1}{4}$ (P)	−1 (C), $\frac{1}{2}$ (V)
P60	incident	P	−60°	C,V	$\frac{1}{2}$	−0.93 (C), 0.45 (V)

Table 2.1 : Input excitations for Pacoima dam

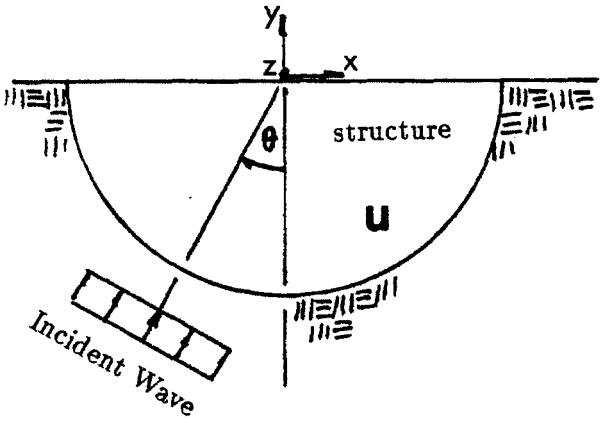

Structure subjected to incident wave

$\mathbf{u}$ = displacements of structure caused by incident wave = $\mathbf{u}^1 + \mathbf{u}^2$

=

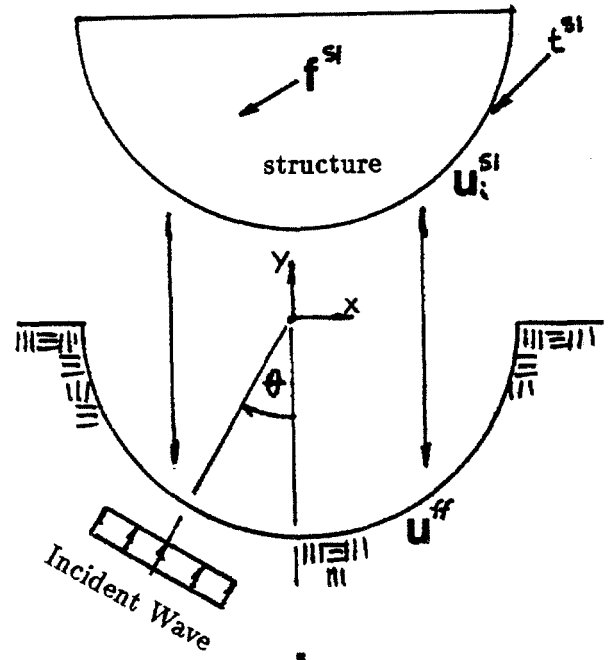

Problem 1

$\mathbf{u}^{ff}$ = free-field motions along canyon boundary, caused by incident wave

$\mathbf{f}^{S1}, t^{S1}$ = body forces and surface tractions to cause structure to deform pseudo-statically with $\mathbf{u}_i^{S1} = \mathbf{u}^{ff}$

+

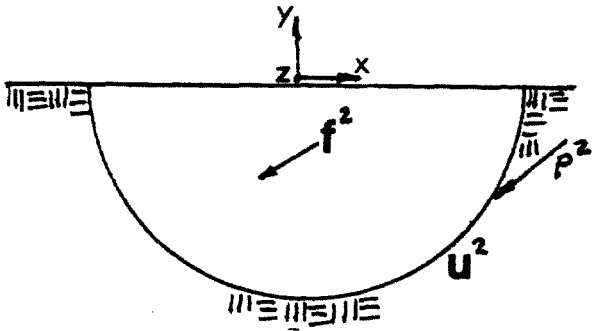

Problem 2

$\mathbf{u}^2$ = displacements caused by $\mathbf{f}^2$ and $\mathbf{p}^2$

$\mathbf{f}^2$ = applied body forces = $-\mathbf{f}^{S1}$

$\mathbf{p}^2$ = applied line load = $-\mathbf{t}^{S1}$

Figure 2.1 : Superposition problem for a structure's response

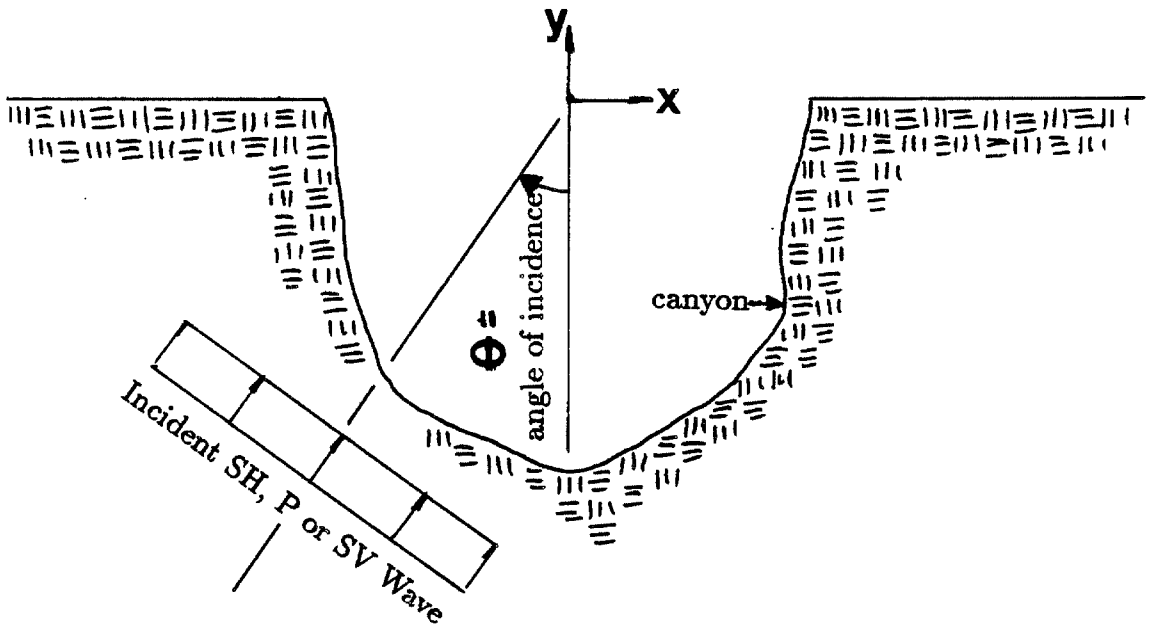

Figure 2.2 : Two-dimensional free-field problem with incident plane body wave

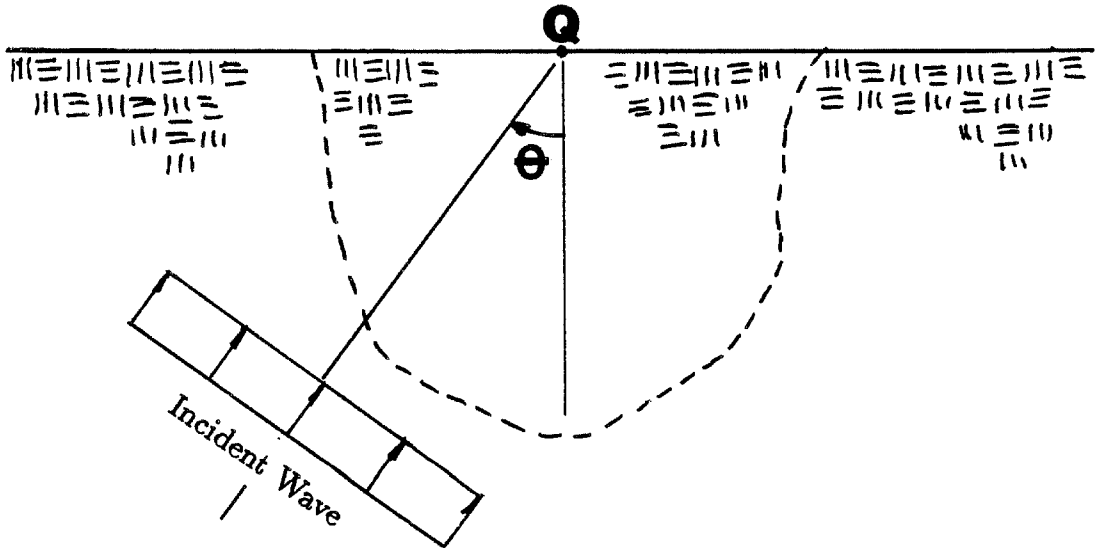

Figure 2.3 : Calibration problem

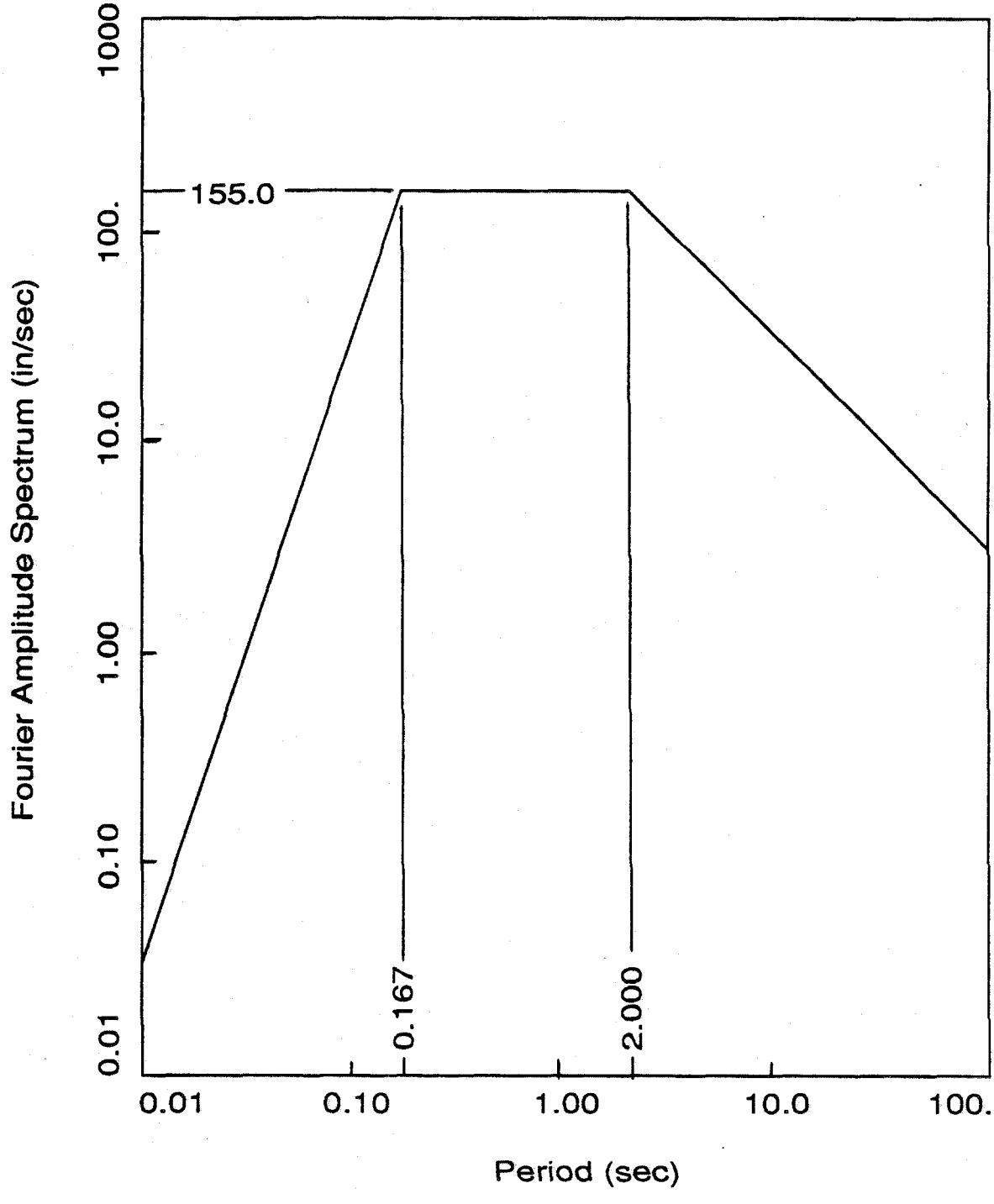

Figure 2.4: Fourier amplitude of horizontal component of ground motion corresponding to an M = 7.5 earthquake near the epicenter [37].

Chapter 3

Solution of the Free-Field Motions

3.1 Superposition Problem

The free-field motions of the canyon are assumed to be generated by incident plane waves in an infinite, linear, elastic, homogeneous, isotropic half-space, and are solved through the method of superposition. The cross section of the canyon (x-y plane) is uniform in the z direction, and all waves propagate normal to the axis of the canyon (z axis). In the superposition problem (Figure 3.1), the solution for an incident wave in the half-space (case I, horizontal surface) is added to the solution for the negative of the tractions $T_x^{\mathrm{I}}, T_y^{\mathrm{I}}, T_z^{\mathrm{I}}$ on the (fictitious) canyon boundary from case I applied to the real canyon (case II, canyon present). The sum of these two problems yields the free-field displacements $u_x^{ff}, u_y^{ff}, u_z^{ff}$ of the canyon caused by an incident wave with a traction-free surface along the canyon ($T_x^{ff}, T_y^{ff}, T_z^{ff} = 0$).

The solutions for the displacements and stresses in case I for incident SH, P and SV waves are given in Appendix B. For case II, the solutions are computed numerically by the direct boundary element method as outlined in the remainder of this chapter. All solutions are carried out in the frequency domain; that is, time variations are $e^{-i\omega t}$. Response quantities are to be interpreted as complex amplitudes of the $e^{-i\omega t}$ variations; for simplicity, the notation for the ω dependence is omitted.

3.2 Basic Equations (case II)

The problem outlined above is two-dimensional: antiplane shear for an incident SH wave and plane strain for incident P and SV waves. For case II, the equations of motion (without body forces) and boundary conditions are [16]

$$\mu\left(\frac{\partial^2 u_z^{\mathrm{II}}}{\partial x^2}+\frac{\partial^2 u_z^{\mathrm{II}}}{\partial y^2}\right)+\omega^2\rho u_z^{\mathrm{II}}=0 \qquad in\ \Omega^c \tag{3.1}$$

$$\left.\begin{array}{l} T_z^{\mathrm{II}}=-T_z^{\mathrm{I}} \qquad on\ \Gamma \\ T_z^{\mathrm{II}}=0 \quad \text{on the horizontal surface} \\ \text{radiation condition at infinity} \end{array}\right\} \tag{3.2}$$

for antiplane shear and

$$\left.\begin{array}{l} (\lambda+\mu)\left(\frac{\partial^2 u_x^{\mathrm{II}}}{\partial x^2}+\frac{\partial^2 u_y^{\mathrm{II}}}{\partial x\partial y}\right)+\mu\left(\frac{\partial^2 u_x^{\mathrm{II}}}{\partial x^2}+\frac{\partial^2 u_x^{\mathrm{II}}}{\partial y^2}\right)+\omega^2\rho u_x^{\mathrm{II}}=0 \\ (\lambda+\mu)\left(\frac{\partial^2 u_x^{\mathrm{II}}}{\partial x\partial y}+\frac{\partial^2 u_y^{\mathrm{II}}}{\partial y^2}\right)+\mu\left(\frac{\partial^2 u_y^{\mathrm{II}}}{\partial x^2}+\frac{\partial^2 u_y^{\mathrm{II}}}{\partial y^2}\right)+\omega^2\rho u_y^{\mathrm{II}}=0 \end{array}\right\} \quad in\ \Omega^c \tag{3.3}$$

$$\left.\begin{array}{l} \left.\begin{array}{l} T_x^{\mathrm{II}}=-T_x^{\mathrm{I}} \\ T_y^{\mathrm{II}}=-T_y^{\mathrm{I}} \end{array}\right\} on\ \Gamma \\ \left.\begin{array}{l} T_x^{\mathrm{II}}=0 \\ T_y^{\mathrm{II}}=0 \end{array}\right\} \text{on the horizontal surface} \\ \text{radiation condition at infinity} \end{array}\right\} \tag{3.4}$$

for plane strain, where

Ω^c = domain of half-space with canyon present

Γ = surface of canyon

ρ = density

ω = frequency (radians per second)

μ = shear modulus

λ = Lamé constant

and u and T denote displacement and surface traction, respectively.

To form the boundary integral equation, the weighted residual method and Green's theorem (twice) are applied to the equations of motion. The weighting functions, W_x, W_y, W_z, in the weighted residual method are chosen to satisfy

$$\mu\left(\frac{\partial^2 W_z}{\partial x^2}+\frac{\partial^2 W_z}{\partial y^2}\right)+\omega^2\rho W_z=\delta_z(x-x_s,y-y_s) \qquad in\ \Omega^h \tag{3.5}$$

$$\left.\begin{array}{l} T_z=0 \quad \text{on the surface} \\ \text{radiation condition at infinity} \end{array}\right\} \tag{3.6}$$

for the antiplane shear problem, and

$$\left.\begin{array}{l} (\lambda+\mu)\left(\frac{\partial^2 W_x}{\partial x^2}+\frac{\partial^2 W_y}{\partial x\partial y}\right)+\mu\left(\frac{\partial^2 W_x}{\partial x^2}+\frac{\partial^2 W_x}{\partial y^2}\right)+\omega^2\rho W_x=\delta_x(x-x_s,y-y_s) \\ (\lambda+\mu)\left(\frac{\partial^2 W_x}{\partial x\partial y}+\frac{\partial^2 W_y}{\partial y^2}\right)+\mu\left(\frac{\partial^2 W_y}{\partial x^2}+\frac{\partial^2 W_y}{\partial y^2}\right)+\omega^2\rho W_y=0 \end{array}\right\} \quad in\ \Omega^h \tag{3.7}$$

$$\left.\begin{array}{l} \left.\begin{array}{l} T_x=0 \\ T_y=0 \end{array}\right\} \text{on the horizontal surface} \\ \text{radiation condition at infinity} \end{array}\right\} \tag{3.8}$$

or

$$\left.\begin{array}{l} (\lambda+\mu)\left(\frac{\partial^2 W_x}{\partial x^2}+\frac{\partial^2 W_y}{\partial x\partial y}\right)+\mu\left(\frac{\partial^2 W_x}{\partial x^2}+\frac{\partial^2 W_x}{\partial y^2}\right)+\omega^2\rho W_x=0 \\ (\lambda+\mu)\left(\frac{\partial^2 W_x}{\partial x\partial y}+\frac{\partial^2 W_y}{\partial y^2}\right)+\mu\left(\frac{\partial^2 W_y}{\partial x^2}+\frac{\partial^2 W_y}{\partial y^2}\right)+\omega^2\rho W_y=\delta_y(x-x_s,y-y_s) \end{array}\right\} \quad in\ \Omega^h \tag{3.9}$$

$$\left.\begin{array}{l} \left.\begin{array}{l} T_x = 0 \\ T_y = 0 \end{array}\right\} \text{on the horizontal surface} \\ \text{radiation condition at infinity} \end{array}\right\} \tag{3.10}$$

for the plane strain problem, where Ω^h is the half-space without the canyon and $\delta_z(x - x_s, y - y_s)$ is the Dirac delta function in the z direction at point (x_s, y_s), etc. for δ_x and δ_y. The above weighting functions can be viewed as displacements that are due to the Dirac delta functions, which can be interpreted as line loads or sources. For this reason, the notation W_x, W_y, W_z is replaced by u_x, u_y, u_z. Restricting the point (x_s, y_s) to be outside the domain Ω^c results in the following integral equations:

$$\int_\Gamma T_z u_z^{\text{II}} d\Gamma = \int_\Gamma u_z T_z^{\text{II}} d\Gamma \tag{3.11}$$

for antiplane shear, and

$$\int_\Gamma \left(T_x u_x^{\text{II}} + T_y u_y^{\text{II}}\right) d\Gamma = \int_\Gamma \left(u_x T_x^{\text{II}} + u_y T_y^{\text{II}}\right) d\Gamma \tag{3.12}$$

for plane strain, where $u_z^{\text{II}}, u_x^{\text{II}}$ and u_y^{II} are the unknown case II displacements at the canyon surface; $T_z^{\text{II}}, T_x^{\text{II}}$ and T_y^{II} are the case II tractions on the canyon defined in Equations 3.2 and 3.4; u_z and T_z are the displacements and tractions at the (fictitious) canyon boundary from the solution of Equations 3.5 and 3.6 in Ω^h, and u_x, u_y, T_x and T_y are displacements and tractions at the (fictitious) canyon boundary from the solution of Equations 3.7 and 3.8 or Equations 3.9 and 3.10 in Ω^h. (Note that Equation 3.8 is the same as Equation 3.10.) Because the source solutions satisfy the traction-free condition on the half-space surface, the domain of integration in Equations 3.11 and 3.12 is only the surface of the canyon.

It is more convenient to place the source point (x_s, y_s) on the boundary Γ and, to avoid the singularity there, relocate the boundary inward and around the point (Figure 3.2). Equations 3.11 and 3.12 become

$$\int_{\Gamma-\Gamma^\epsilon} T_z u_z^{II} d\Gamma + \int_{\Gamma^s} T_z u_z^{II} d\Gamma^s = \int_{\Gamma-\Gamma^\epsilon} u_z T_z^{II} d\Gamma + \int_{\Gamma^s} u_z T_z^{II} d\Gamma^s \tag{3.13}$$

and

$$\begin{aligned} \int_{\Gamma-\Gamma^\epsilon} \left(T_x u_x^{II} + T_y u_y^{II}\right) d\Gamma \;\; + \;\; \int_{\Gamma^s} \left(T_x u_x^{II} + T_y u_y^{II}\right) d\Gamma^s = \\ \int_{\Gamma-\Gamma^\epsilon} \left(u_x T_x^{II} + u_y T_y^{II}\right) d\Gamma \;\; + \;\; \int_{\Gamma^s} \left(u_x T_x^{II} + u_y T_y^{II}\right) d\Gamma^s. \end{aligned} \tag{3.14}$$

The final step is to take the limit of the above integrals as $r_s \to 0$, so that the relocated boundary approaches the true canyon boundary Γ. The results are

$$\begin{aligned} \lim_{r_s \to 0} \left(\int_{\Gamma-\Gamma^\epsilon} T_z u_z^{II} d\Gamma \right) + u_z^{II}(x_s, y_s) \lim_{r_s \to 0} \left(\int_{\Gamma^s} T_z d\Gamma^s \right) = \\ \lim_{r_s \to 0} \left(\int_{\Gamma-\Gamma^\epsilon} u_z T_z^{II} d\Gamma + \int_{\Gamma^s} u_z T_z^{II} d\Gamma^s \right) \end{aligned} \tag{3.15}$$

and

$$\begin{aligned} \lim_{r_s \to 0} \left(\int_{\Gamma-\Gamma^\epsilon} \left(T_x u_x^{II} + T_y u_y^{II}\right) d\Gamma \right) + u_x^{II}(x_s, y_s) \lim_{r_s \to 0} \left(\int_{\Gamma^s} T_x d\Gamma^s \right) \\ + u_y^{II}(x_s, y_s) \lim_{r_s \to 0} \left(\int_{\Gamma^s} T_y d\Gamma^s \right) = \\ \lim_{r_s \to 0} \left(\int_{\Gamma-\Gamma^\epsilon} \left(u_x T_x^{II} + u_y T_y^{II}\right) d\Gamma + \int_{\Gamma^s} \left(u_x T_x^{II} + u_y T_y^{II}\right) d\Gamma^s \right). \end{aligned} \tag{3.16}$$

The above formulations are merely statements of the Reciprocal Theorem and involve the solution of the case II problem in Ω^c as one set of loads and displacements, and the solution in Ω^h for the line sources as the other set of loads and displacements. There are four main terms present in Equations 3.15 and 3.16: tractions $T_x^{II}, T_y^{II}, T_z^{II}$ applied to the canyon which are obtained analytically in Ω^h (see Section 3.1), the displacements $u_x^{II}, u_y^{II}, u_z^{II}$ caused by these tractions (see Section 3.4 for the boundary element solution in Ω^c), and the displacements u_x, u_y, u_z and tractions T_x, T_y, T_z at

the fictitious boundary of the canyon caused by the line sources and obtained by solving Equations 3.5 to 3.10 in Ω^h (see Section 3.3).

3.3 Solution of the Source Problem

The solution of Equations 3.5 and 3.6 for the displacements u_z and tractions T_z in the antiplane shear problem (SH case) is obtained through the method of images. A line load and its image in an infinite full-space are placed symmetrically about the plane y = 0 at points (x_s, y_s) and $(x_s, -y_s)$. The displacements and stresses from these two line loads are then added together, yielding the surface y = 0 (the fictitious surface of the half-space) traction free. A summary of the method of images for an antiplane shear line load is given in Figure 3.3, and results appear in Appendix C.1.

The method of images does not work completely in the plane strain (P or SV) case, as only one of the two tractions on the fictitious half-space surface can be eliminated when superposing the image solution. Therefore, a superposition procedure is necessary: case A in the full-space, where the line load and its image (actually, the negative image) are applied so that $T_y^A(x, y = 0)$ for δ_x, δ_{-x} and $T_x^A(x, y = 0)$ for δ_y, δ_{-y} on the fictitious half-space surface become zero, and case B in the half-space, where the nonzero tractions $T_x^A(x, y = 0)$ for δ_x, δ_{-x} and $T_y^A(x, y = 0)$ for δ_y, δ_{-y} are removed from the surface; i.e., $T_x^B(x, y = 0) = -T_x^A(x, y = 0)$ and $T_y^B(x, y = 0) = 0$ for δ_x, δ_{-x} and $T_y^B(x, y = 0) = -T_y^A(x, y = 0)$ and $T_x^B(x, y = 0) = 0$ for δ_y, δ_{-y}. Calculation of the displacements and stresses of case A is performed analytically, while those of case B are conveniently obtained through a spatial Fourier transform. The procedure for line load δ_x is summarized in Figure 3.4; that for δ_y is similar.

The inverse Fourier transform from which the displacements and stresses of case B in the plane strain problem are computed has the form [12]:

$$g^B(x,y) = -\frac{K_s}{2\pi}\int_{-\infty}^{\infty} h(\beta,y_s)\; g(\beta,y)\; \exp\left(i\beta K_s(x-x_s)\right)\, d\beta, \qquad (3.17)$$

where

$g^B(x,y)$ = either the displacement or stress response from case B

K_s = shear wave number = $\omega/C_s = 1/L_s$

C_s = shear wave speed = $\sqrt{\mu/\rho}$

L_s = shear wavelength

β = spatial Fourier transform parameter

= (L_s / transform wavelength)

$h(\beta,y_s)\cdot\exp(-i\beta K_s x_s)$

= spatial Fourier transform of

$T_x^A(x,y=0)$ for δ_x, δ_{-x} or $T_y^A(x,y=0)$ for δ_y, δ_{-y}

$g(\beta,y)$ = transfer function for displacement or stress due to

$T_x(x,y=0) = \exp(i\beta K_s x)$ for δ_x, δ_{-x} or

$T_y(x,y=0) = \exp(i\beta K_s x)$ for δ_y, δ_{-y}.

The transfer function $g(\beta,y)$ can be expressed as

$$g(\beta,y) = \hat{g}(\beta,y)/\Re \qquad (3.18)$$

where

$$\Re = (2\beta^2-1)^2 - 4\beta^2\alpha\gamma, \qquad (3.19)$$

and $\alpha = \sqrt{\beta^2-1}$ (negative root if $\beta < 1$, positive root if $\beta > 1$), $\gamma = \sqrt{\beta^2-\chi^2}$ (negative root if $\beta < \chi$, positive root if $\beta > \chi$), $\chi = C_s/C_p$, and C_p = P wave speed $= \sqrt{(\lambda+2\mu)/\rho}$. Expressions for $h(\beta,y_s)$ and $\hat{g}(\beta,y)$ are contained in Appendix D.1.

The inverse Fourier transform (Equation 3.17) is integrated numerically, noting that the integrand is either even or odd in the integration parameter β; therefore, only the $\beta \geq 0$ portion need be considered (Appendix D.2). Further, the integrand is either real or imaginary for β greater than β_s (transform wavelength = shear wavelength; note $\beta_s = 1.0$). The upper limit of integration, β_{max}, is chosen to produce a negligible truncation error and is selected to be that given by a transform wavelength equal to 1/6 the sum of the depth of the source point and the depth of the response point; i.e.,

$$\beta_{max} = \frac{6.0\, C_s}{\omega\,(y + y_s)}. \tag{3.20}$$

The sampling increment $\Delta\beta$ of the integrand varies and is finer near β_p (transform wavelength = P wave wavelength; note $\beta_p = 0.612$ for Poisson's ratio (ν) = 0.20), β_s, and β_r (transform wavelength = Rayleigh wavelength; note $\beta_r = 1.0977$ for $\nu = 0.20$) because of rapid variations of the integrand there. Up to $\beta' = \beta_r + 0.0081$, the sampling points (total of 256) are specified individually based on $\nu = 0.20$; for $\nu \neq 0.20$, they are adjusted to fit the different values for β_p and β_r. Beyond β', the spacing of the sampling points increases with β as $\Delta\beta = \beta/150$.

The actual integration is done in several parts. Between $\beta = 0$ and the first sampling point below β_r ($\beta_r - \Delta$, where $\Delta = 0.0001$) and between $\beta_r + \Delta$ and β'' (where $\Delta\beta$ first exceeds $[2\pi/10K_s(x - x_s)]$), the integrand is approximated as a quadratic across every $\Delta\beta$ pair using the three sampling points and integrated analytically. Between $\beta_r - \Delta$ and $\beta_r + \Delta$, care must be taken with the pole in the integrand; i.e., the denominator term $\Re$ (Equation 3.18) goes to zero at $\beta = \beta_r$. This portion of the integral is evaluated as the Cauchy principal value and includes the residue of the integrand at the pole. Approximating the numerator as linear between $\beta_r - \Delta$ and β_r and between β_r and $\beta_r + \Delta$ and linearizing $\Re$ about β_r permits the Cauchy

principal value to be obtained analytically, a sufficiently accurate procedure with the chosen value of Δ. Results of the integration between $\beta_r - \Delta$ and $\beta_r + \Delta$ are included in the expressions in Appendix D.2. The final part of the integration is between β'' and β_{max}, where the $\cos(\beta K_s(x - x_s))$ or $\sin(\beta K_s(x - x_s))$ term (see Appendix D.2) varies rapidly enough to make the quadratic approximation of the entire integrand inaccurate (more than 1/10 of a wavelength in $\Delta\beta$, which defines β''). Therefore, the cos or sin term is separated out and integrated analytically with the rest of the integrand, which is approximated as quadratic (again using the three sampling points over each $\Delta\beta$ pair). A summary of the integration scheme appears in Figure 3.5.

3.4 Solution of the Integral Equation

The displacements $u_x^{II}, u_y^{II}, u_z^{II}$ in Equations 3.15 and 3.16 are linearly interpolated within boundary elements (Figure 3.6) from discrete values at the nodes (Figure 3.6), which become the unknowns of the problem [4]. For the antiplane shear problem, algebraic equations in terms of the nodal displacements are generated by applying the line source δ_z to each node and performing the integration in Equation 3.15, resulting in n equations for the n unknowns, where n is the number of nodes. For the plane strain problem, $2n$ equations are generated for the $2n$ unknowns by applying the line loads δ_x and δ_y to each node and performing the integrations in Equation 3.16. Solution of the algebraic equations by matrix factorization yields the displacements $u_x^{II}, u_y^{II}, u_z^{II}$ at the nodes.

For a line source applied at a particular node (node s), the integration in Equations 3.15 and 3.16 over $\Gamma - \Gamma^\epsilon$ for all elements not adjacent to this node is performed by three-point Gauss quadrature. Within adjacent elements, where this integral must be evaluated in the limit as $r_s \to 0$, account must be taken of the singularities that occur

in the line load displacements and tractions. Four procedures are needed, depending on whether the integrand contains the $u_k T_k^{II}$ term or the $T_k u_k^{II}$ term, $k = x, y, z$, and whether node s is at the top of the canyon on the horizontal free surface (nodes 1 and n, Figure 3.6) or below the horizontal free surface.

$u_k T_k^{II}$, node s below top of canyon. The Hankel functions present in the line source displacements (Appendix C) are expressed as the sum of singular terms ($\ln(r_s)$ and for the plane strain displacements, $1/r_s$) and a series of nonsingular terms [2], and are combined according to the expressions in the Appendix. This produces $u_k = st + ns$ where st = a constant times $\ln(r_s)$ (Appendix E, $1/r_s$ cancels) and ns = nonsingular series; the singular term is independent of frequency ω. The term $(st \times T_k^{II})$ is integrated analytically after T_k^{II} is approximated as a quadratic, using the three Gauss points as sampling points; $(ns \times T_k^{II})$ is integrated by three-point Gauss quadrature.

$u_k T_k^{II}$, node s at top of canyon. Closed form expressions for the displacements due to a line load at the surface of a half-space, such as in Appendix C for a buried line load, are available only for $\omega = 0$. However, an integration scheme similar to that above can still be employed, since the singular term st is independent of frequency ω and, thus, known (constant times $\ln(r_s)$, Appendix E), and since the nonsingular part ns can be obtained at the Gauss points by ns = u_k - st, where u_k is computed by the inverse Fourier transform (see Section 3.3).

$T_k u_k^{II}$, node s below top of canyon. Expansion of the Hankel functions in the line load tractions along $\Gamma - \Gamma^\epsilon$, and combination according to the expressions in Appendix C produces $T_k = st + ns$, where st = constant times $(1/r_s)$ (independent of ω). However, for the antiplane shear problem, the constant of the singular

term is zero along $\Gamma - \Gamma^\epsilon$; thus, no contribution to Equation 3.15 from the term $T_z u_z^{II}$ results. Such is not the case in plane strain, where the terms to be integrated are $(st + ns)(r_s/l)$ and $(st + ns)(1 - (r_s/l))$, and where l = the length of the adjacent element, and u_k^{II}, $k = x$ or y has been expressed in terms of the linear interpolation functions. Except for $st \times 1$, all terms are integrable, and three-point Gauss quadrature is used. For $st \times 1$, however, the constants of the singular terms for the two adjacent elements are equal but of opposite sign, so no contribution results except at the end of the longer element, if the adjacent elements differ in length. No singularity occurs in this region, and analytical integration is used.

$T_k u_k^{II}$, **node s at top of canyon.** The line load traction T_z is again zero, as in the case above. For plane strain, the $\omega = 0$ solutions for T_x and T_y are also zero along $\Gamma - \Gamma^\epsilon$ except at $r_s = 0$, where a delta function (line force) exists. Although no closed form solutions for T_x and T_y exist for $\omega > 0$, it will be similar, but with an added continuous nonsingular variation along the adjacent element. Thus, noting that the line force at $r_s = 0$ does not enter into the integrand along $\Gamma - \Gamma^\epsilon$, Gauss quadrature (three points) is used where T_x and T_y are computed at the Gauss points by the inverse Fourier transform (see Section 3.3).

The integration over Γ^s, also in the limit as $r_s \to 0$, is performed analytically using the expressions of Appendix E for Γ^s. Results for the terms on the left side of Equations 3.15 and 3.16 are bounded and appear in Appendix F. The limits of the Γ^s integrals on the right side of Equations 3.15 and 3.16 are zero, since the line source displacements are singular only as $\ln(r_s)$.

3.5 Comparison with Previous Solutions

To verify the computer program used to generate the free-field motions, a number of comparisons were made with previously obtained solutions (Figure 3.7). The antiplane shear problem has been solved analytically [38,44] and numerically [43,34,41, 42], and exact displacements from an incident SH wave on a semicircular canyon have been tabled [41] for various values of the ratio of the canyon diameter to the shear wavelength (denoted by $\psi_s = D/L_s$). For horizontal incidence ($\theta = 90°$), results from the boundary element program at $\psi_s = 4.0$ came within 11% of the exact solution for 23 equally spaced nodes and were within 3% for 45 nodes (Table 3.1). These percentages were obtained by dividing the greatest difference in the two solutions by the maximum amplitude in the exact solution. Also included in Reference [41] are results from a numerical, boundary matching scheme, where the case II solution was obtained using compressional and shear wave line sources in a half-space placed inside the (fictitious) canyon boundary, and where a least squares minimization of the error in the generated tractions was used to define the source strengths. Although these values were superior to the boundary element ones, their accuracy depends on the source locations, and the presented results were from optimum locations determined by trial.

The major set of results for the plane strain problem consists of plotted displacements due to incident P, SV and Rayleigh waves on circular and elliptical canyons obtained by the boundary matching scheme [41]. Incidentally, although this solution technique was adequate for the present purposes, it was felt that an independent verification was desirable, and thus, the direct boundary element procedure was implemented. Good agreement to the plotted results in Reference [41] for the incident P and SV waves was obtained (Figure 3.8). During the present investigation, a de-

scription of an indirect boundary element method for the plane strain case applicable to layered domains has appeared [30]. Its results, as well as those of an earlier investigation in which the free-surface condition on the half-space was only approximately satisfied [18], showed good agreement to the results of [41].

In addition to the above check of the plane strain problem, three other tests were performed. The first used an analytical solution for P and SV waves incident onto a circular cavity in a full-space. The accuracy of the boundary element values (exact values from [41]) was similar to that obtained in the SH verification study. Superior performance of the optimized boundary matching procedure [41] was again noted. Since this test problem did not exercise portions of the boundary element program dealing with the horizontal surface of the half-space, in particular the inverse Fourier transform, this part of the program was separated out and used to solve the problem of a uniformly distributed load on the surface of a half-space between $x = \pm b$. Numerical results for a viscoelastic material appear in Reference [12] and agreed about as well as could be expected, best for the least viscous material, considering that the boundary element computations were performed with a nonviscous material. The third test problem (Figure 3.9) simultaneously exercised most of the program and utilized a set of tractions $T_k^B, k = x, y$ applied to a semicircular canyon in a half-space. These tractions equalled those ($T_k^A, k = x, y$) along the surface of a fictitious semicircular canyon in a half-space subjected to a concentrated line load (P_x or P_y) at $x = 0$, $y = 0$ and computed by the separate program for the inverse Fourier transform mentioned above. Since the loaded region lay entirely within the fictitious canyon boundary, perfectly accurate computations would lead to equal sets of displacements u_k^A and u_k^B, $k = x, y$, at the location of the canyon boundary. Although numerical errors are present in both solutions, the displacements from solution A can be considered exact,

and the boundary element values compare well and exhibit convergence (Table 3.2).

3.6 Artificial Resonances

One difficulty encountered in the boundary element solutions of the exterior problems considered here is the presence of artificial resonances. This phenomenon is demonstrated for the antiplane shear problem of a semicircular canyon subjected to a vertically incident SH wave (Figure 3.10). Sample displacement responses appear in Figure 3.12 for a 17 and a 33 node discretization. The plotted results were obtained at a constant increment of $\Delta\psi_s$ equal to 0.013. Note that the finer discretization narrows the resonances.

The frequencies of the artificial resonances were the same as the natural frequencies of the material cut out of the half-space to form the canyon, fixed at the canyon boundary Γ (Figure 3.11), hereafter referred to as the interior region. These frequencies equal the roots of $J_n(\omega R/C_s)$, $n = 0, 2, 4, ...$, where R = canyon radius, and are denoted by ω_{nm}, $m = 1, 2, 3, ...$. The mode shape of the interior region corresponding to ω_{nm} is $J_n(\omega_{nm} r/C_s)\cos(n\theta)$, where r, θ are cylindrical coordinates (Figure 3.11).

The cause of the artificial resonances for the problem of Figure 3.10 can be seen by examining Equation 3.15,

$$\lim_{r_s \to 0}\left(\int_{\Gamma-\Gamma^\epsilon} T_z u_z^{II} d\Gamma\right) + u_z^{II}(x_s, y_s) \lim_{r_s \to 0}\left(\int_{\Gamma^s} T_z \, d\Gamma^s\right) = \lim_{r_s \to 0}\left(\int_{\Gamma-\Gamma^\epsilon} u_z T_z^{II} d\Gamma\right), \quad (3.21)$$

where a final term has been dropped (see Section 3.4). To show analytically that this equation degenerates at a frequency equal to a natural frequency of the interior region of Figure 3.11, express the applied tractions as a Fourier series and consider any single term

$$T_z^{\mathrm{II}} = a_j \cos(j\theta),\ j = 0, 2, 4, \ldots . \tag{3.22}$$

Because of the axisymmetric geometry, the resulting displacements will be

$$u_z^{\mathrm{II}} = b_j \cos(j\theta),\ j = 0, 2, 4, \ldots \tag{3.23}$$

where b_j is unknown. In the terms of Equation 3.21 involving integration over $\Gamma - \Gamma^\epsilon$, only the $\cos(j\theta)$ component of the traction T_z and displacement u_z due to the line source will contribute; thus, one needs only consider

$$T_z = c_j \cos(j\theta),\ j = 0, 2, 4, \ldots \tag{3.24}$$

$$u_z = d_j \cos(j\theta),\ j = 0, 2, 4, \ldots . \tag{3.25}$$

Substitution of Equations 3.22 to 3.25 into 3.21, integrating, and taking the limit yields

$$\left.\begin{aligned} \left(R\pi c_j + \tfrac{1}{2}\right) b_j &= R\pi d_j a_j \ \text{ for } j = 0 \\ \left(R\tfrac{\pi}{2} c_j + \tfrac{1}{2}\cos(j\theta_s)\right) b_j &= R\tfrac{\pi}{2} d_j a_j \ \text{ for } j > 0, \end{aligned}\right\} \tag{3.26}$$

an equation for b_j, where θ_s is θ where the line source is applied. Through a rather tedious argument not presented here, it can be shown that as $\omega \to \omega_{jm}$ for any m, $d_j \to 0$ for $j \geq 0$, $c_j \to (-1/(2R\pi))$ for $j = 0$ and $c_j \to (-1/(R\pi))\cos(j\theta_s)$ for $j > 0$. Thus, Equation 3.26 degenerates to

$$0 \cdot b_j = 0. \tag{3.27}$$

The limit solution is well behaved, but cannot be computed except in the limit. More general treatment would reveal that the degeneracy occurs in the plane strain problem

and for arbitrary canyon geometries, but not for solution of the interior problem and not for source applications away from the canyon boundary Γ.

The degeneracy seen above as $\omega \rightarrow \omega_{jm}$ also occurs with the matrix equation generated when u_z^{II} is interpolated within boundary elements from nodal values. The matrix equation becomes singular and the right hand side becomes deficient in load to the mode associated with ω_{jm}. However, because of the discretizations involved, these two states are not reached at exactly the same frequency, and the occurrence of the matrix singularity when the right hand side is not completely deficient causes an artificial resonance in the shape $\cos(j\theta)$. To overcome this difficulty, responses are interpolated within the zones of the artificial resonances, using the undisturbed responses outside the zones. This interpolation requires that the discretization be fine enough to narrow the resonances enough so that the true responses can be traced. For the Pacoima dam analysis presented in the next chapter, the highest frequency considered (12.5 Hz.) corresponded to $\psi_s = 6.0$ in Figure 3.12 so, with a 22 node discretization, the interpolation was easily accomplished.

Angle θ to node (rad.)	u_z (23 node mesh)	u_z (45 node mesh)	u_z (exact)
$\pi/2$	(+3.522,−0.358)	(+3.861,−0.182)	(+3.978,−0.151)
$5\pi/22$	(−4.075,+0.577)	(−3.928,+0.528)	(−3.872,+0.530)
$3\pi/22$	(+3.122,−2.021)	(+3.107,−2.079)	(+3.076,−2.096)
$\pi/11$	(−2.843,+1.218)	(−2.939,+1.531)	(−2.942,+1.612)
0.00	(+2.419,−0.062)	(+2.667,−0.113)	(+2.735,−0.115)
$-\pi/22$	(−1.438,−0.848)	(−1.571,−1.074)	(−1.621,−1.150)
$-3\pi/22$	(+0.595,+1.263)	(+0.329,+1.291)	(+0.257,+1.313)
$-5\pi/22$	(−0.081,−0.786)	(+0.363,−0.795)	(+0.461,−0.790)
$-\pi/2$	(−0.343,+1.085)	(−0.320,+0.532)	(−0.336,+0.387)

Table 3.1 : Displacements (real part, imaginary part) for a horizontally incident ($\theta = 90°$) SH wave on a semicircular canyon ($\psi_s = 4.0$). See Figure 3.7. Exact solution from tables in [41].

Load (at (0,0))	Angle θ to node (rad.)	Disp. comp.	$\frac{u^B \cdot \mu}{P}$ (9 node mesh)	$\frac{u^B \cdot \mu}{P}$ (17 node mesh)	$\frac{u^A \cdot \mu}{P}$
P_x	$\frac{\pi}{2}$	x	(+0.057,−0.266)	(+0.059,−0.266)	(+0.060,−0.266)
		y	(−0.017,−0.152)	(−0.019,−0.150)	(−0.020,−0.150)
	$\frac{3\pi}{8}$	x	(+0.021,−0.249)	(+0.024,−0.247)	(+0.025,−0.247)
		y	(−0.058,−0.163)	(−0.055,−0.158)	(−0.054,−0.158)
	$\frac{\pi}{4}$	x	(+0.057,−0.216)	(+0.058,−0.214)	(+0.059,−0.214)
		y	(−0.079,−0.139)	(−0.076,−0.136)	(−0.075,−0.134)
	$\frac{\pi}{8}$	x	(+0.110,−0.179)	(+0.111,−0.176)	(+0.111,−0.176)
		y	(−0.056,−0.081)	(−0.055,−0.079)	(−0.054,−0.078)
	0.00	x	(+0.134,−0.164)	(+0.133,−0.164)	(+0.133,−0.164)
		y	(0.00,0.00)	(0.00,0.00)	(0.00,0.00)
P_y	$\frac{\pi}{2}$	x	(+0.020,+0.155)	(+0.020,+0.152)	(+0.020,+0.152)
		y	(+0.181,−0.181)	(+0.180,−0.179)	(+0.180,−0.178)
	$\frac{3\pi}{8}$	x	(−0.053,+0.035)	(−0.050,+0.034)	(−0.050,+0.034)
		y	(+0.167,−0.205)	(+0.167,−0.200)	(+0.167,−0.199)
	$\frac{\pi}{4}$	x	(−0.082,−0.022)	(−0.079,−0.021)	(−0.078,−0.021)
		y	(+0.108,−0.253)	(+0.108,−0.248)	(+0.108,−0.248)
	$\frac{\pi}{8}$	x	(−0.059,−0.026)	(−0.057,−0.026)	(−0.057,−0.025)
		y	(+0.045,−0.300)	(+0.046,−0.298)	(+0.046,−0.296)
	0.0	x	(0.00,0.00)	(0.00,0.00)	(0.00,0.00)
		y	(+0.019,−0.319)	(+0.020,−0.316)	(+0.020,−0.316)

Table 3.2 : Displacements (real part, imaginary part) for the third test problem of the P-SV program (see Figure 3.9), $\psi_s = 1.30, \nu = 0.2$.

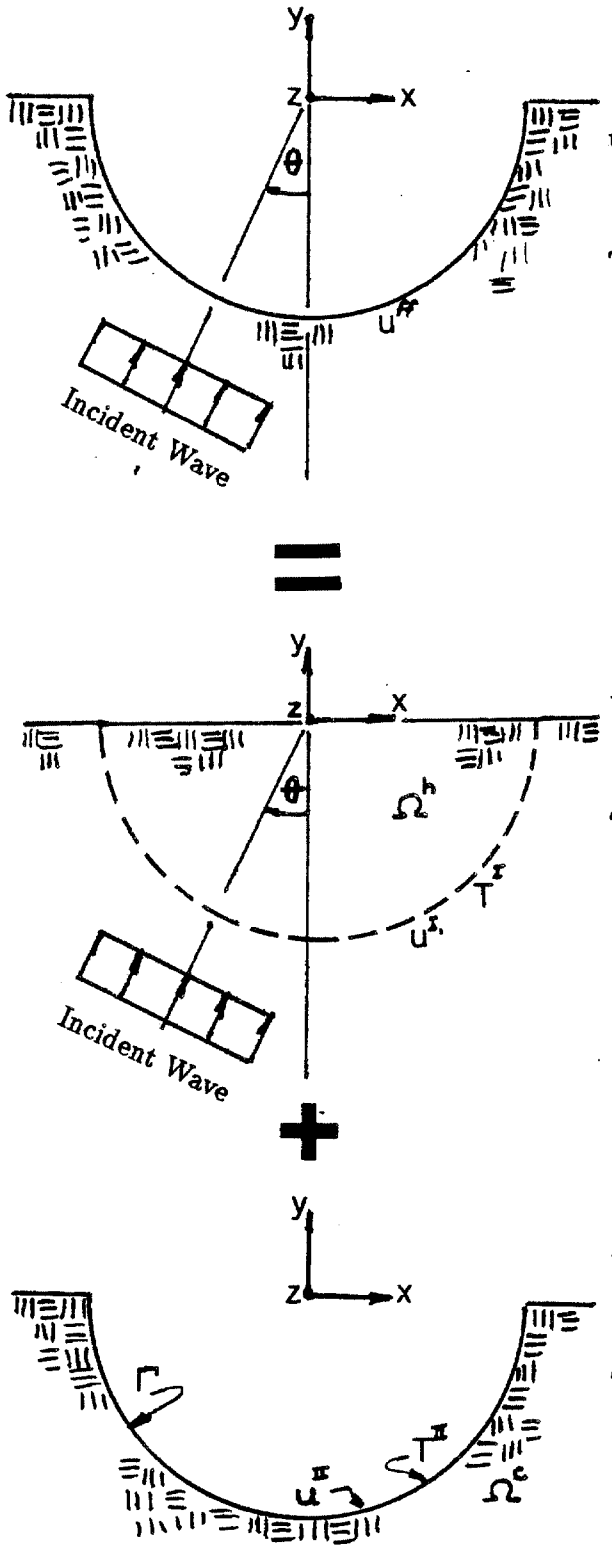

Free-Field Motions = Case I + Case II

$\mathbf{u}^{ff}$ = free-field displacements along canyon boundary = $\mathbf{u}^{I} + \mathbf{u}^{II}$

$\mathbf{T}^{ff}$ = free-field tractions on canyon surface = $\mathbf{T}^{I} + \mathbf{T}^{II} = \mathbf{0}$

Case I : solved analytically (Appendix B)

$\mathbf{u}^{I}$ = displacements along fictitious canyon boundary, caused by incident wave

$\mathbf{T}^{I}$ = tractions along fictitious canyon boundary, caused by incident wave

Case II : solved numerically by BEM

$\mathbf{u}^{II}$ = displacements along canyon boundary caused by $\mathbf{T}^{II}$

$\mathbf{T}^{II}$ = tractions applied to the canyon boundary = $-\mathbf{T}^{I}$

Figure 3.1 : Superposition problem for free-field motions

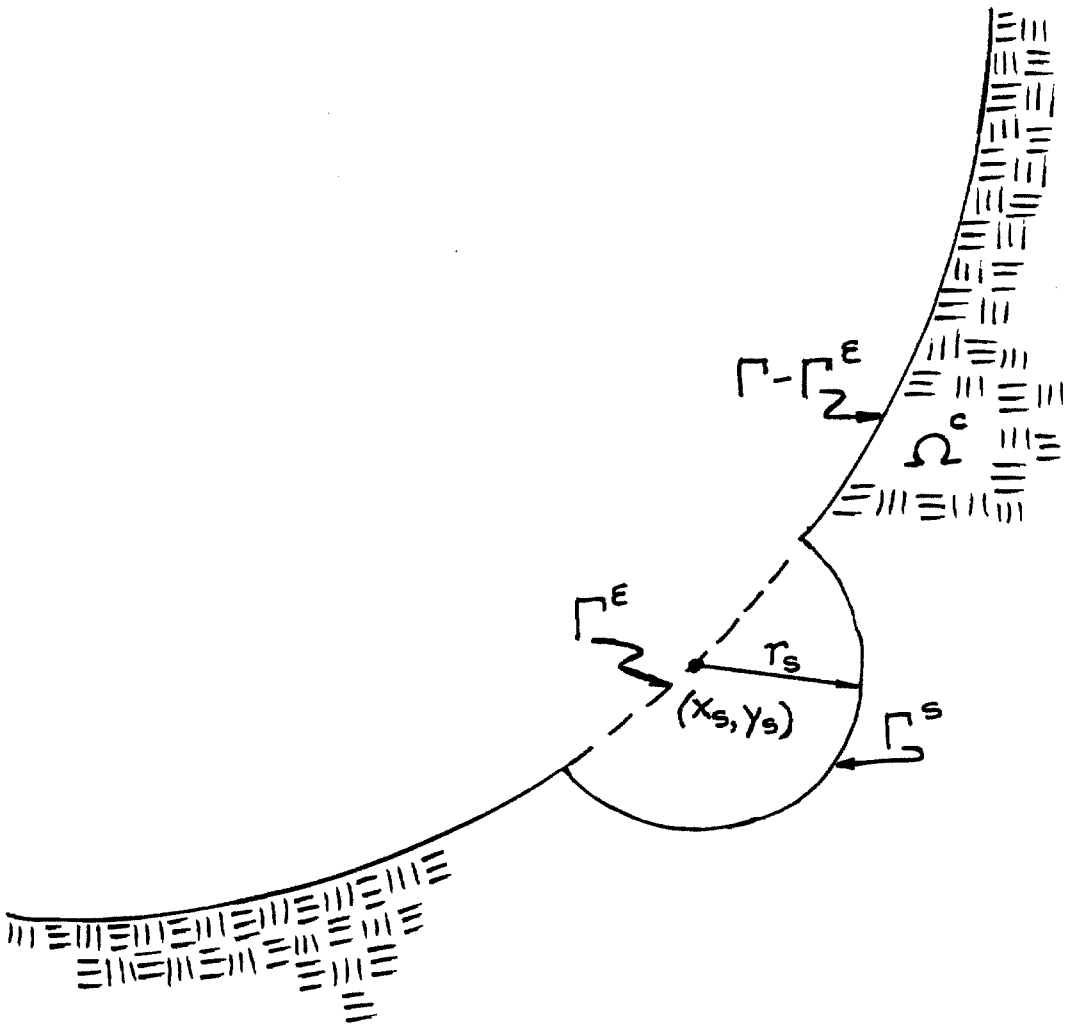

Figure 3.2 : Relocation of the canyon boundary around the point (x_s, y_s)

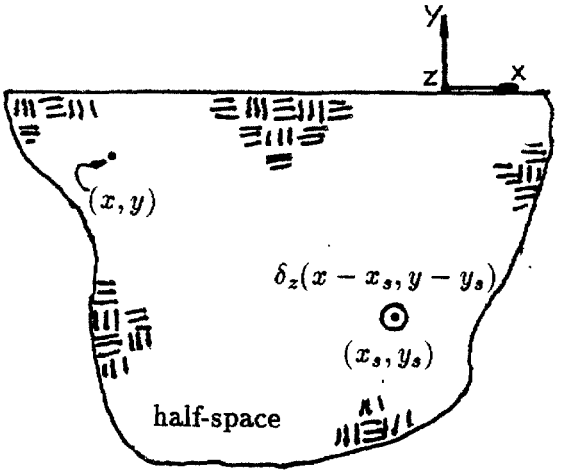

$g(x, y)$ = response due to δ_z

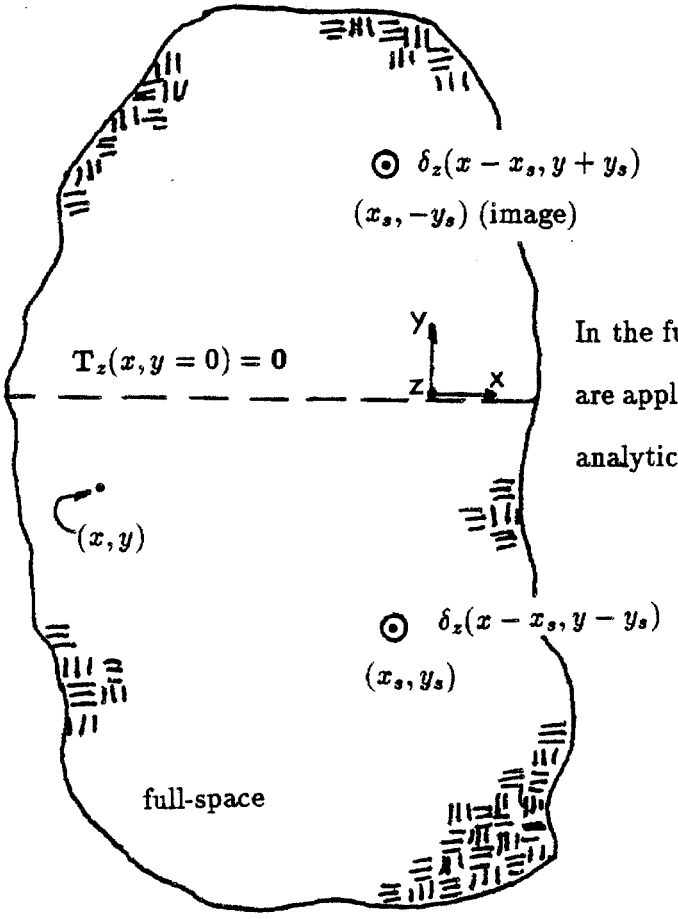

In the full-space, the line load and its image are applied. The response $g(x, y)$ is computed analytically (Appendix C.1).

Figure 3.3 : Solution for the line load δ_z in a half-space (antiplane shear)

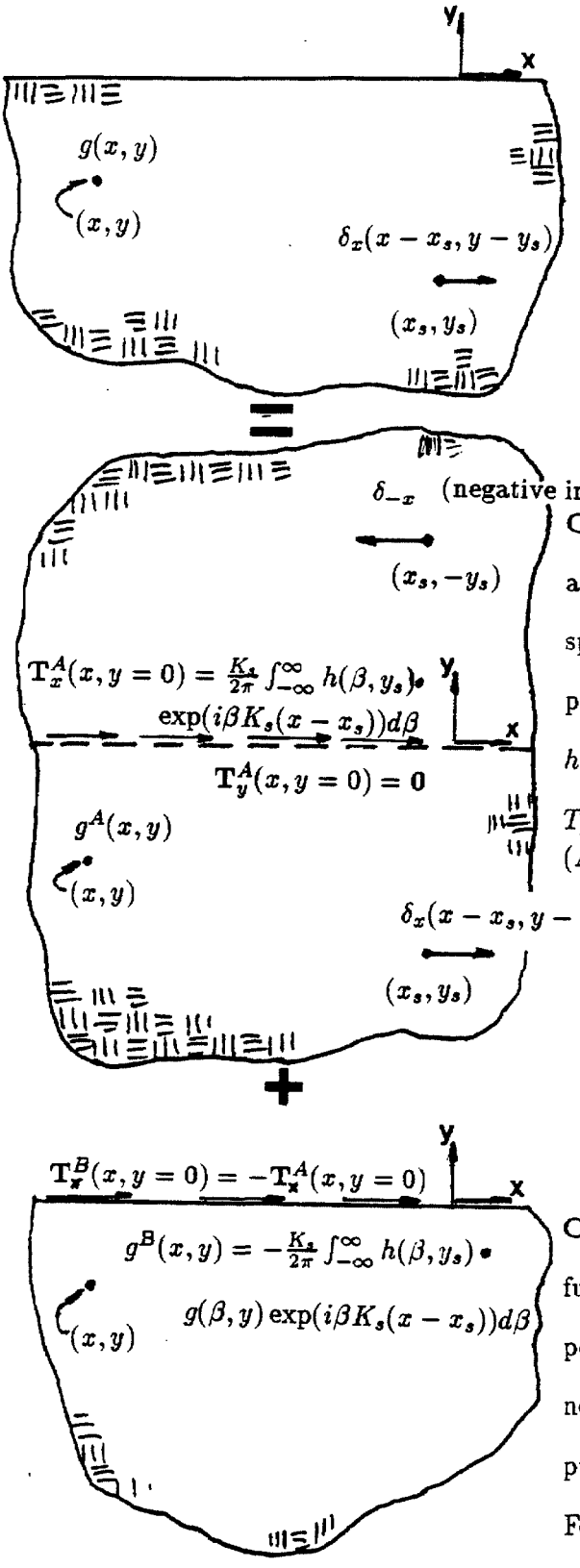

$g(x,y)$ = response due to δ_x

$= g^A(x,y) + g^B(x,y)$

Case A : In the full-space, the line load and its negative image are applied. The response $g^A(x,y)$ is computed analytically (Appendix C.2) as are the Fourier components $h(\beta, y_s)\cdot\exp(-i\beta K_s x_s)$ **of the residual traction** T_x^A at the fictitious surface of the half-space (Appendix D.1).

Case B : In the half-space , the transfer function $g(\beta, y)$ is computed analytically (Appendix D.1), and the response $g^B(x,y)$ to the negative of the surface tractions T_x^A is computed by a numerical integration of the inverse Fourier transform (Section 3.3).

Figure 3.4 : Superposition problem for line load δ_x in a half-space (plane strain)

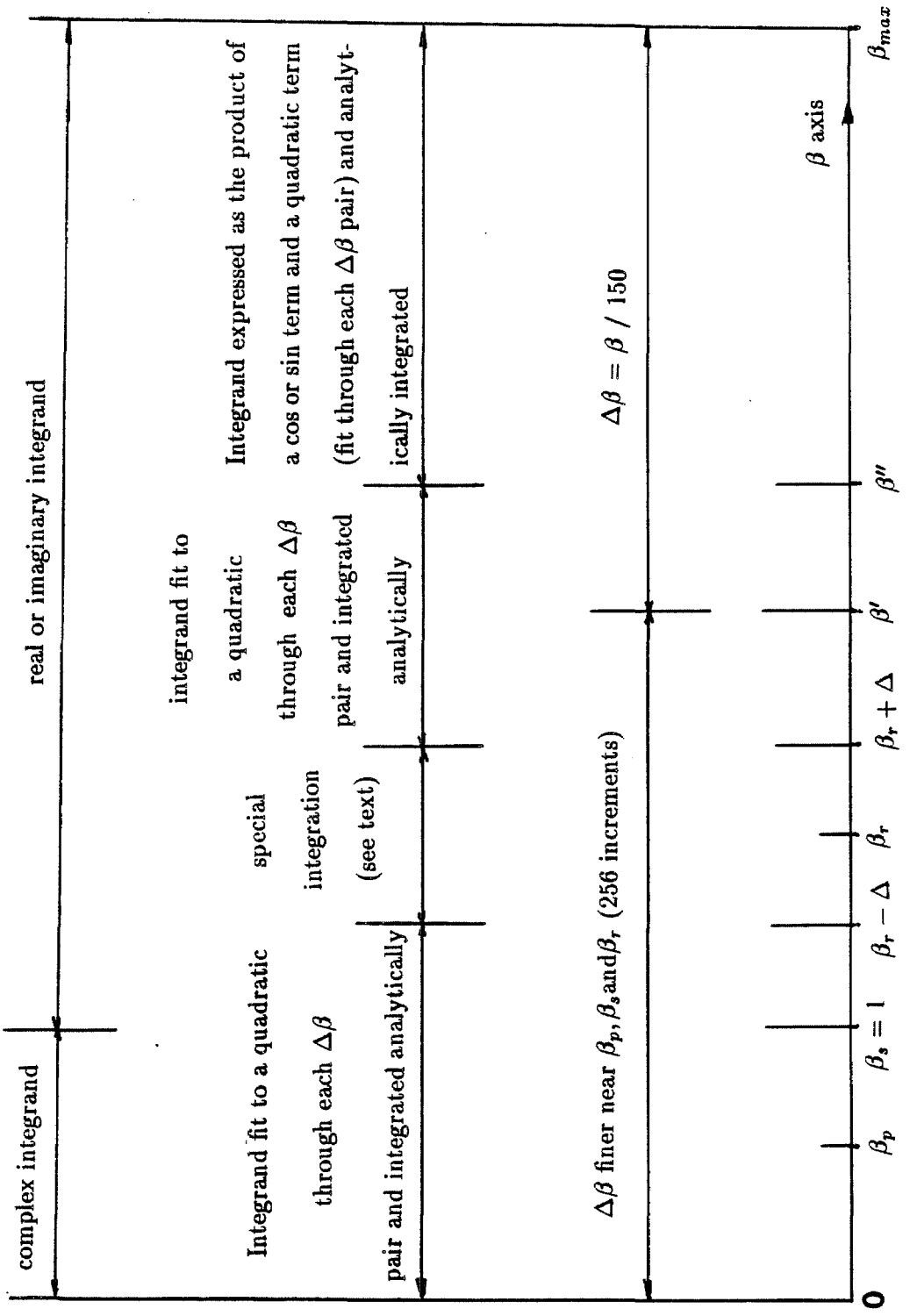

Figure 3.5 : Integration scheme for the inverse Fourier transform

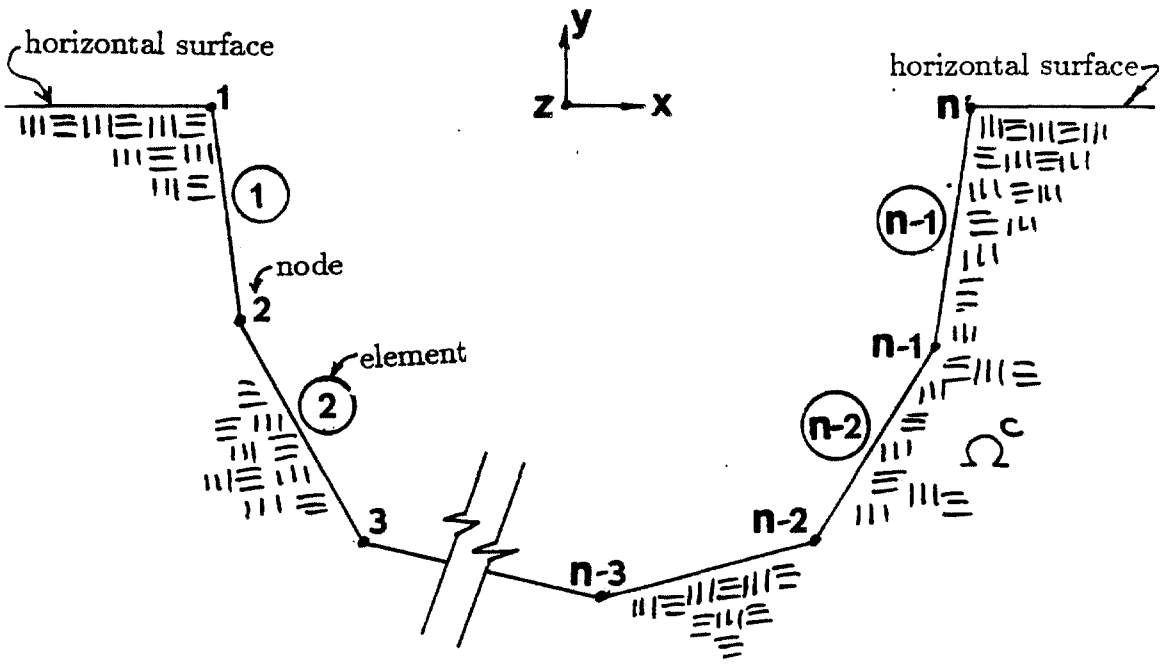

Figure 3.6 : Discretized canyon for the boundary element method

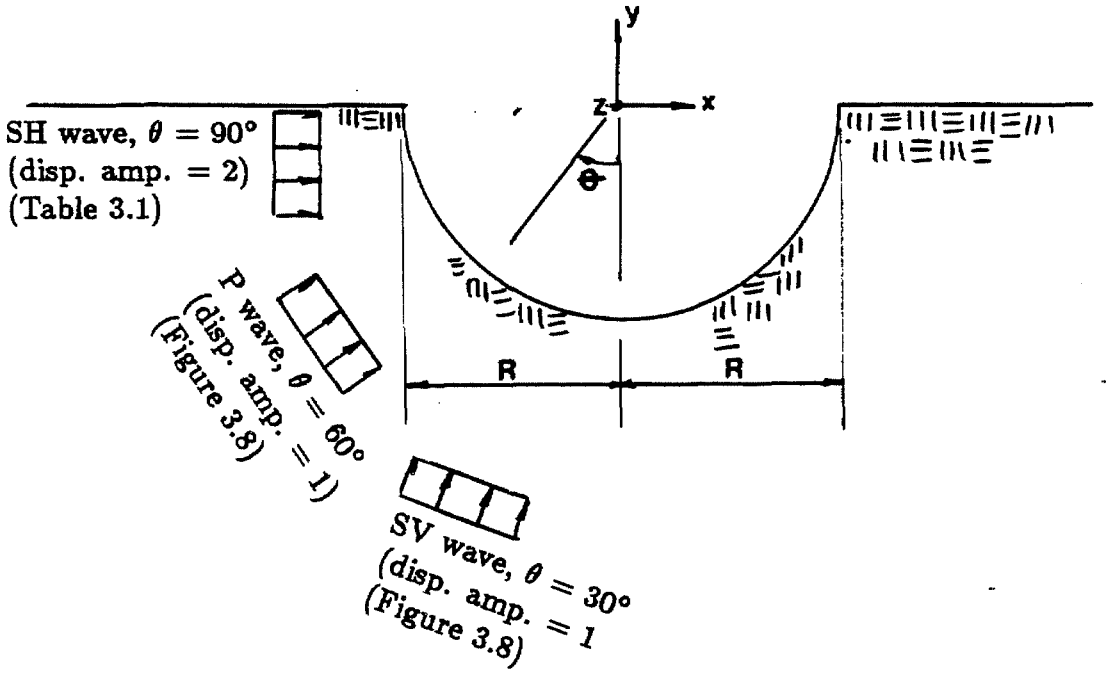

Figure 3.7: Cases involving incident waves on a semicircular canyon for which boundary element solutions are compared to those in [41].

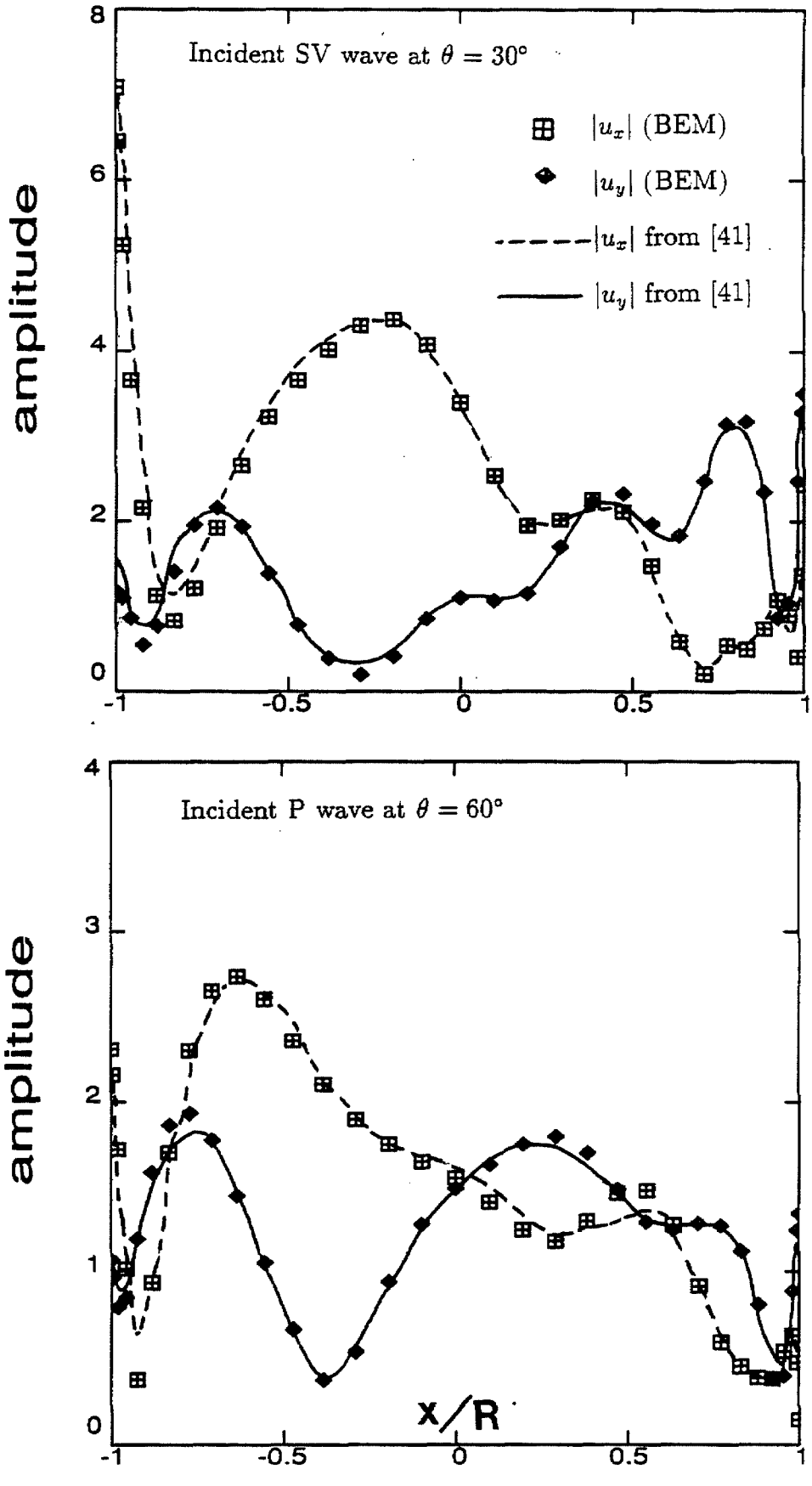

Figure 3.8: Comparison of displacement amplitudes at the surface of a semicircular canyon from the boundary element method (BEM) and from [41].

(See Figure 3.7.) ($\psi_s = 2.0$, uniform mesh of 33 nodes, $\nu = 1/3$)

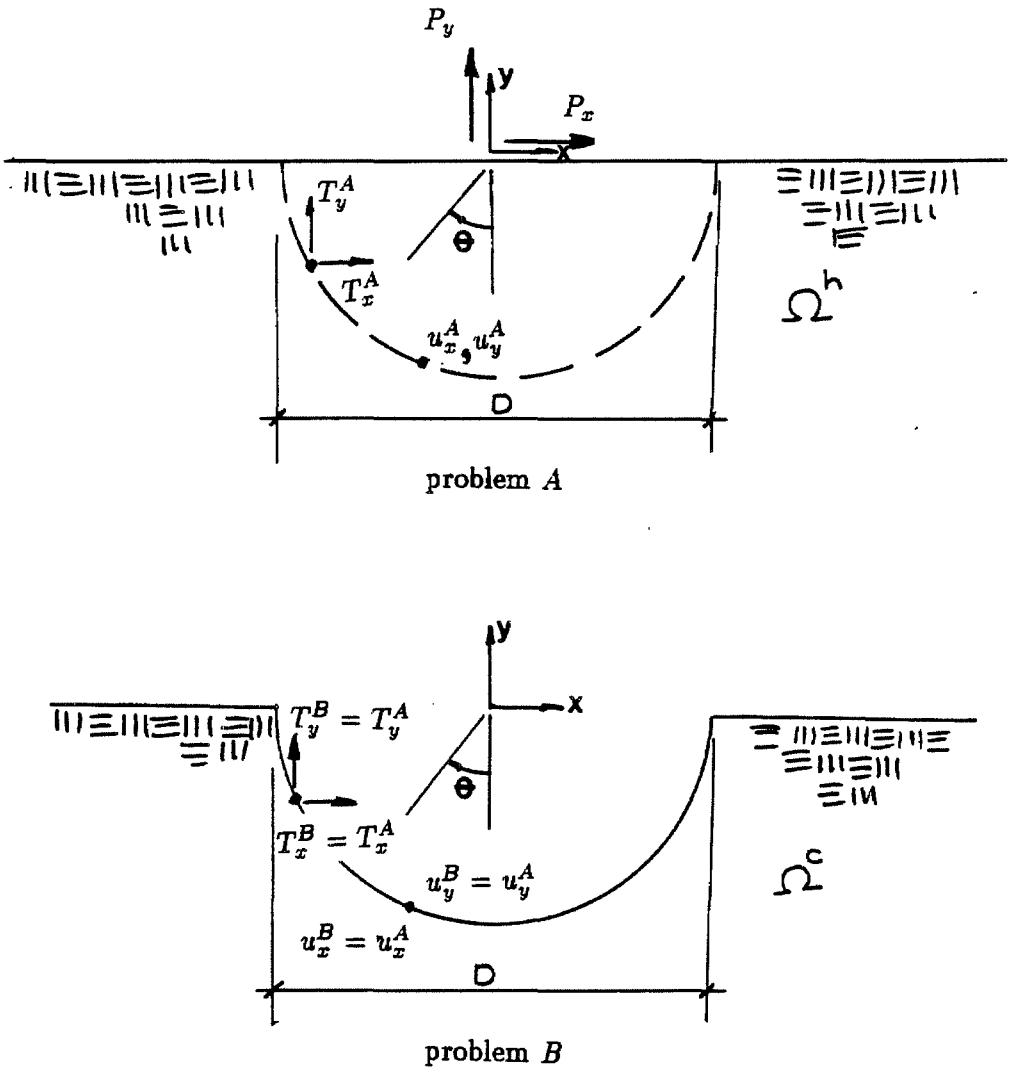

Figure 3.9: Verification of the P-SV program using a comparison solution obtained numerically (problem A). Problem B is solved by the boundary element technique.

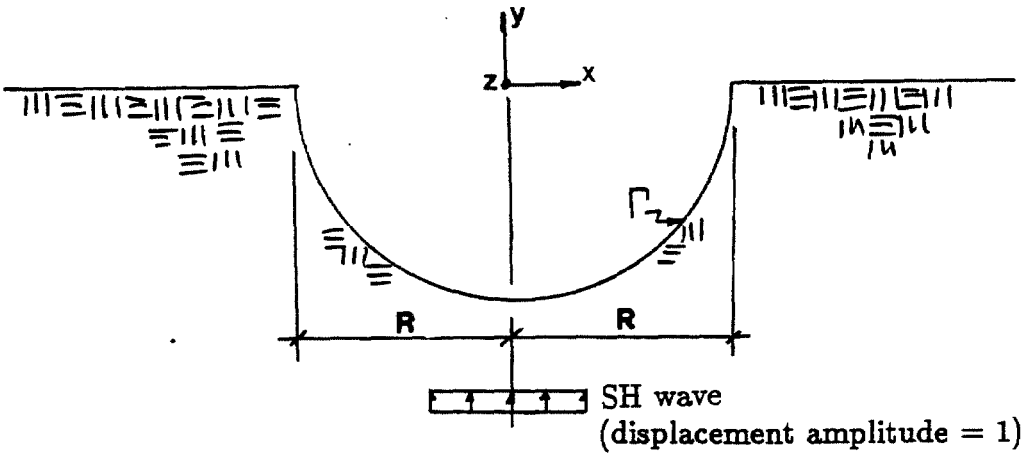

Figure 3.10: Semicircular canyon subjected to a vertically incident SH wave. Artificial resonance problem.

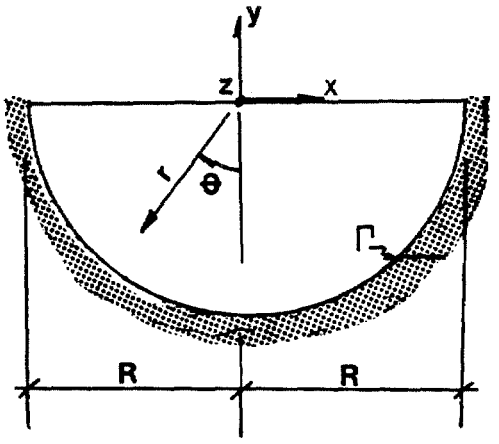

Figure 3.11 : Interior region fixed along canyon boundary

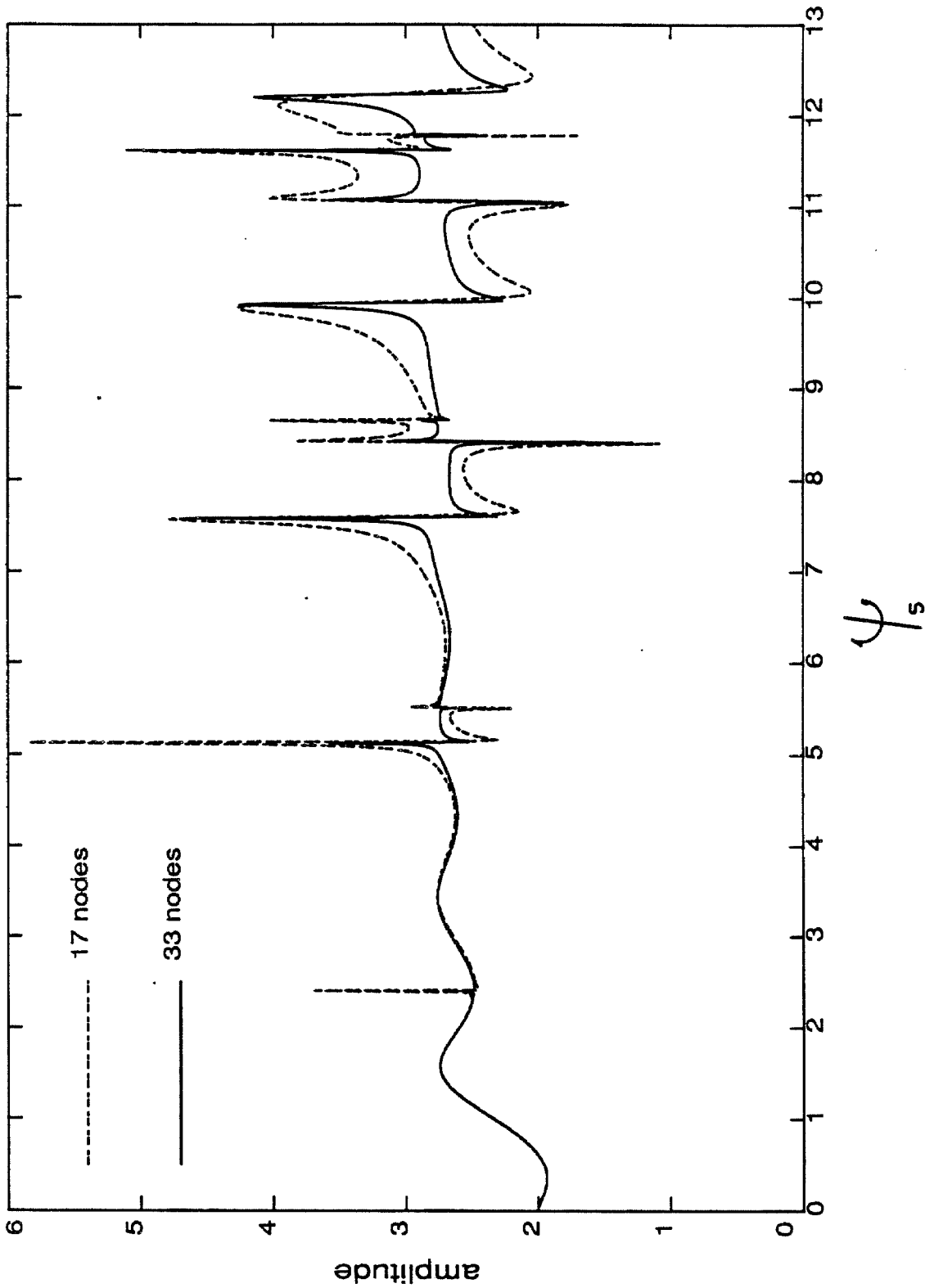

Figure 3.12: Sample displacement responses (node at top of canyon) for artificial resonance problem

Chapter 4

Results of Analysis of Pacoima Dam Subjected to Uniform and Nonuniform Seismic Input

4.1 Free-Field Motions

The free-field motions of the Pacoima dam canyon located near Los Angeles, California, are computed by the boundary element method. The canyon is assumed to be uniform in cross-section and to extend to infinity in the stream direction in an infinite, elastic, isotropic, homogeneous medium. The shape of the canyon coincides with the dam-foundation interface below the crest, and above, is defined using topographic maps of the region surrounding the dam. For the upper canyon, the shape is taken as the average of the topography over approximately 50 meters on each side the dam. The final canyon is 124 meters deep and 224 meters across (Figure 4.1). To calculate the free-field motions, the canyon boundary is discretized into 21 boundary elements as also shown in the figure. The properties of the canyon rock are E = 13,800 MPa, $\nu = 0.20$ and $C_s = 1475\ (m/s)$ as determined from in situ tests [20].

The free-field motions in the stream (S) direction are computed independently from those in the cross-stream (C) and vertical (V) directions. The stream motions are produced by SH waves normally incident to the axis of the canyon which, thus, have no variations in the stream direction. Normally, incident P and SV waves produce

the cross-stream and vertical motions that also vary only around the canyon. Six excitations are employed as shown in Table 2.1: uniform in the stream direction (U-S), incident SH wave at $\theta = 0°$ (SH0), incident SH wave at $\theta = -60°$ (SH60), uniform in cross-stream and vertical directions (U-CV), incident SV and P waves at $\theta = 0°$ (SVP0), and incident P wave at $\theta = -60°$ (P60). The last column in the table gives the sum of incident and reflected amplitudes at a horizontal, free surface; thus, the first three cases (stream excitation) are consistent, and the last three cases (C-V excitation) are approximately so. With this reference, amplitudes of the stream, cross-stream, and vertical components of motion are approximately 1, 1, and $\frac{1}{2}$, respectively.

Free-field motions of Pacoima canyon for the excitations listed in Table 2.1 were computed between 0.0 Hz. and 12.5 Hz. at an increment of 0.25 Hz. Interpolation is used within the zones of artificial resonances (see Section 3.6), which appeared near 6.50, 10.75 and 12.0 Hz. for the stream excitations and near 7.25, 8.50 and 10.50 Hz. for the C-V excitations. Figures 4.2 (stream excitation) and 4.3 (C-V excitation) show amplitude and phase variations around Pacoima canyon for the frequencies 0.0, 1.0, 3.0, 7.0 and 11.0 Hz. The sizable differences between the uniform and nonuniform motions which occur above 1.0 Hz. can be expected to cause significant differences in the dam response since the fundamental frequency of Pacoima dam is in the range from 4.0 to 5.0 Hz. (see next section). For example, the cross-stream component of motion at 3.0 Hz. under the P60 excitation varies from an amplitude of 1.7 at one bank to 0.3 at the other with about a 0.4 cycle phase difference (Figure 4.3e), compared to an in-phase motion of amplitude 1.0 for the uniform excitation.

Computation of the free-field motions was carried out on a VAXstation II. The CPU time for one incident SH wave for 45 frequencies was approximately 4 minutes.

One P-SV excitation required approximately 41 hours of CPU time. A large part of the increase is due to the integration required by the inverse Fourier transforms.

4.2 Discretization of Pacoima Dam, Foundation and Reservoir

Once the free-field motions of Pacoima canyon are determined, the structural response of Pacoima dam (assumed linear) is calculated as described in Chapter 2. Pacoima dam, its foundation, and the water are discretized by the finite element method as shown in Figures 4.4, 4.6 and 4.5, respectively. The dam, 111 meters in height, contains 51 8-node shell elements in its mesh. The foundation below the dam is taken to include all of the rock within approximately 150 meters of the foundation interface and is modeled with 280 8-node brick elements. The reservoir is modeled as infinite with compressible water and is discretized into 306 three-dimensional fluid elements with a transmitting boundary 180 meters from the upstream face of the dam. Only within this distance are the free-field excitations to the water applied. Material properties for the elements of the dam and foundation are E = 20,700 MPa (dam concrete) and 13,800 MPa (foundation rock), $\nu = 0.20$ (dam and foundation) and specific gravity = 2.40 (dam). A value of 5 % modal damping is chosen for the dam-foundation substructure, and a 0.85 reflection coefficient is taken along the floor and sides of the reservoir.

4.3 Results of Analysis

Pacoima dam is analyzed for the excitations given in Table 2.1, and the results are presented here. The analysis is performed in the frequency domain and then trans-

formed into the time domain as outlined in Chapter 2. The response of the dam is calculated for both a full and an empty reservoir.

As discussed in Chapter 2, the calculations employ eigenvectors of the dam-foundation system as generalized coordinates. The first 20 were included; the twentieth had a natural frequency of 22.0 Hz. Responses were computed at 83 frequencies, closely spaced around the resonant peaks, in the range from 0.0 to 12.0 Hz. Fundamental resonances of the system occurred at 5.1 Hz. (antisymmetric) and 5.2 Hz. (symmetric) without water and at 3.8 Hz. (symmetric) and 4.3 Hz. (antisymmetric) with water. The frequencies without water agree with measured values form forced vibration field tests at a low water level [20].

Frequency responses of various accelerations and stresses (no gravity effects) are shown in Figures 4.8 (stream excitation without water), 4.9 (C-V excitation without water), 4.10 (stream excitation with water) and 4.11 (C-V excitation with water) for the excitations given in Table 2.1. A key diagram (looking upstream) of Pacoima dam, showing the locations of elements and nodes in the finite element mesh of the dam for which results are presented, appears in Figure 4.7. The plots in Figures 4.8 thru 4.11 are arranged to facilitate comparison among the results for the three stream excitations and among the results for the three C-V excitations. Both total and pseudo-static responses are included for the incident wave excitations.

Major features of the results in Figures 4.8 to 4.11 are as follows.

- Greater response occurs with rather than without water, in agreement with numerous previous studies.

- The pseudo-static component of the response is largest near the perimeter of the dam, where it can be a significant fraction of the total response. This fraction is small in the interior of the dam except for the stresses at low frequencies, where

the pseudo-static component everywhere approaches infinity as the frequency approaches zero. Thus, the importance of the pseudo-static stresses can be quantified only in the time domain when the low frequency content of the motion is specified.

- Responses for the stream excitations are generally smaller for the incident wave input (SH0 and SH60) than for the uniform input (U-S). Such is not necessarily the case for the C-V excitation.

- Responses for the P60 C-V excitation show a large increase in the fundamental symmetric resonance. Investigation revealed that this increase was caused by the cross-stream component of the ground motion, which seems odd since experience with uniform ground motion associates symmetric response with stream ground motion and antisymmetric response with cross-stream ground motion. However, examination of Figure 4.3e shows that the cross-stream motion from the P60 excitation, having large amplitude and being about a half cycle out-of-phase bank to bank in the interval from 3.0 to 7.0 Hz., contains a large squeezing component that will excite the symmetric modes. This effect can be attributed to the near horizontal incidence of the P60 wave and thus is absent from the SVP0 excitation.

Other quantification of the effect of nonuniform seismic input can be obtained in the time domain. Recall from Chapter 2 that the computed time domain responses are standard deviations for a random excitation with an earthquake-like frequency content (magnitude 7.5, near the epicenter). Contours of these standard deviations for stress appear in Figures 4.12 (no water) and 4.13 (with water). Each figure contains six parts (one for each of the excitations in Table 2.1), and each part contains four

stress contours (total arch, pseudo-static (p-s) arch, total cantilever, and pseudo-static (p-s) cantilever). All stresses plotted are maxima from the upstream or downstream face and are normalized with respect to the total arch stress at the center crest for the case U-S with water (= 100). Contour intervals have values of 5 to 25 by 5 and from 30 upward by 10. A blank plot indicates that no stresses reached the 5% level. Note that the pseudo-static stresses for the uniform excitations are zero.

Two trends seen with the frequency responses of Figures 4.8 to 4.11, the effect of water to increase the dam response and the effect of incident waves for the stream excitation to reduce the dam response, are again evident in the stress contours of Figures 4.12 and 4.13. Time domain quantification of the pseudo-static component of the response shows it to be small, reaching only the 27% level at the ends of the upper arch (Figures 4.12e and 4.13e). Generally, the largest pseudo-static stresses occur near the foundation interface, where the dynamic component of the response (total minus pseudo-static) is small. The increase in amplitude of the fundamental symmetric resonance for the P60 excitation shows up strongly. In fact, the P60 excitation with water (Figure 4.13f) produces the largest response of any case; the arch stress at the center crest reaches the 122% level. The completely different response generated by the P60 excitation compared to the two other C-V ones, U-CV and SVP0, is revealed by Figures 4.12d to 4.12f (no water), where the response to P60 is predominantly symmetric and those to U-CV and SVP0 are predominantly antisymmetric.

To condense the results, averages of the total arch stresses along the crest, expressed as a percentage of the average for case U-S with water (= 100), are computed and presented in Table 4.1. These values are a simple quantification of the effects of nonuniform seismic input and the presence of water: 89% (U-S), 47% (SH0), 66% (SH60), 46% (U-CV), 48% (SVP0) and 62% (P60) without water, and 100% (U-S),

62% (SH0), 73% (SH60), 78% (U-CV), 63% (SVP0) and 122% (P60) with water.

The responses in Figures 4.12 and 4.13 are only relative values and, as such, are independent of the constant C in Equation 2.25. From Equation 2.26, selection of the duration T_{eq} permits the actual responses to the input of Figure 2.4 to be obtained. With $T_{eq} = 15$ seconds, the 100 level in Figures 4.12 and 4.13 corresponds to 13 MPa. This, of course, indicates that cracking and/or joint opening will play an important role in the response due to strong earthquake ground motions [13], even when reduced responses are produced by some of the incident wave excitations.

Computation for the analysis of Pacoima dam was performed on a VAXstation II. CPU time for the six excitations (Table 2.1) for 83 frequencies was approximately 22.5 hours for the no water case, and 34 hours for the case of the full reservoir.

	Full Reservoir	Empty Reservoir
U-S	100	89
SH0	62	47
SH60	73	66
U-CV	78	46
SVP0	63	48
P60	122	62

Table 4.1 : Average of standard deviations of total arch stress along the crest expressed as a percent of the average for excitation U-S with a full reservoir.

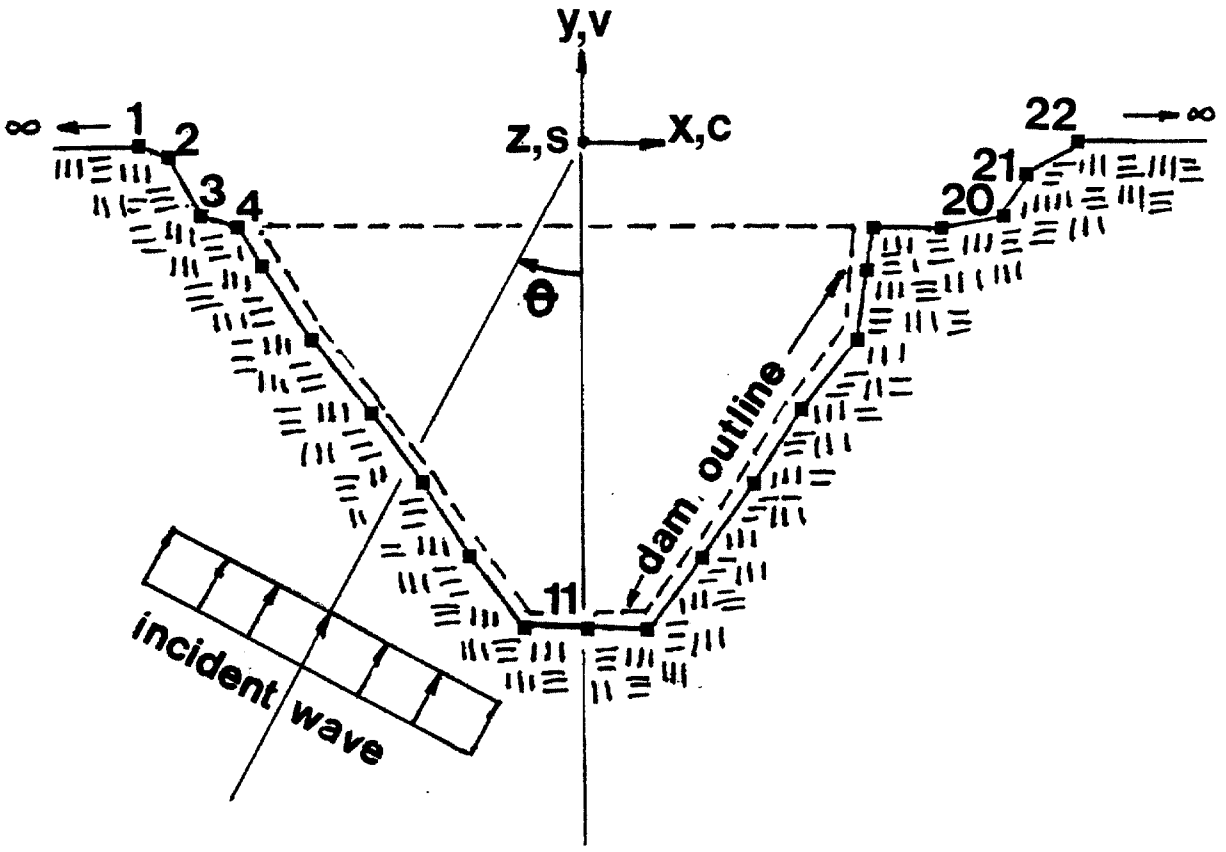

Figure 4.1 Boundary element mesh of Pacoima canyon

Figure 4.2 : Stream free-field motions (amplitude and phase variations) along Pacoima canyon for excitations given below.

Figure 4.2a : Excitation U-S

Figure 4.2b : Excitation SH0

Figure 4.2c : Excitation SH60

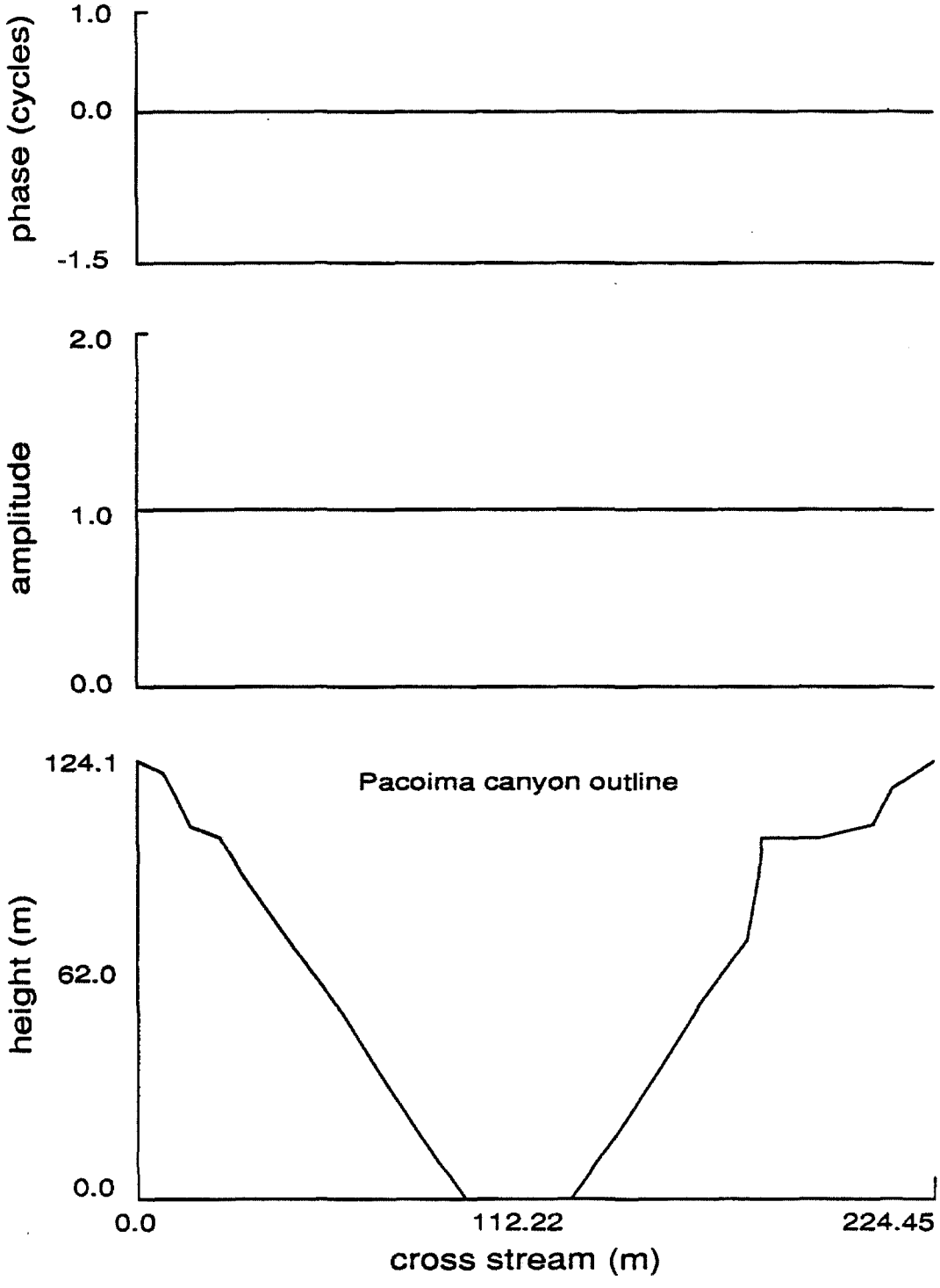

Figure 4.2a : stream free-field motions, Case U-S

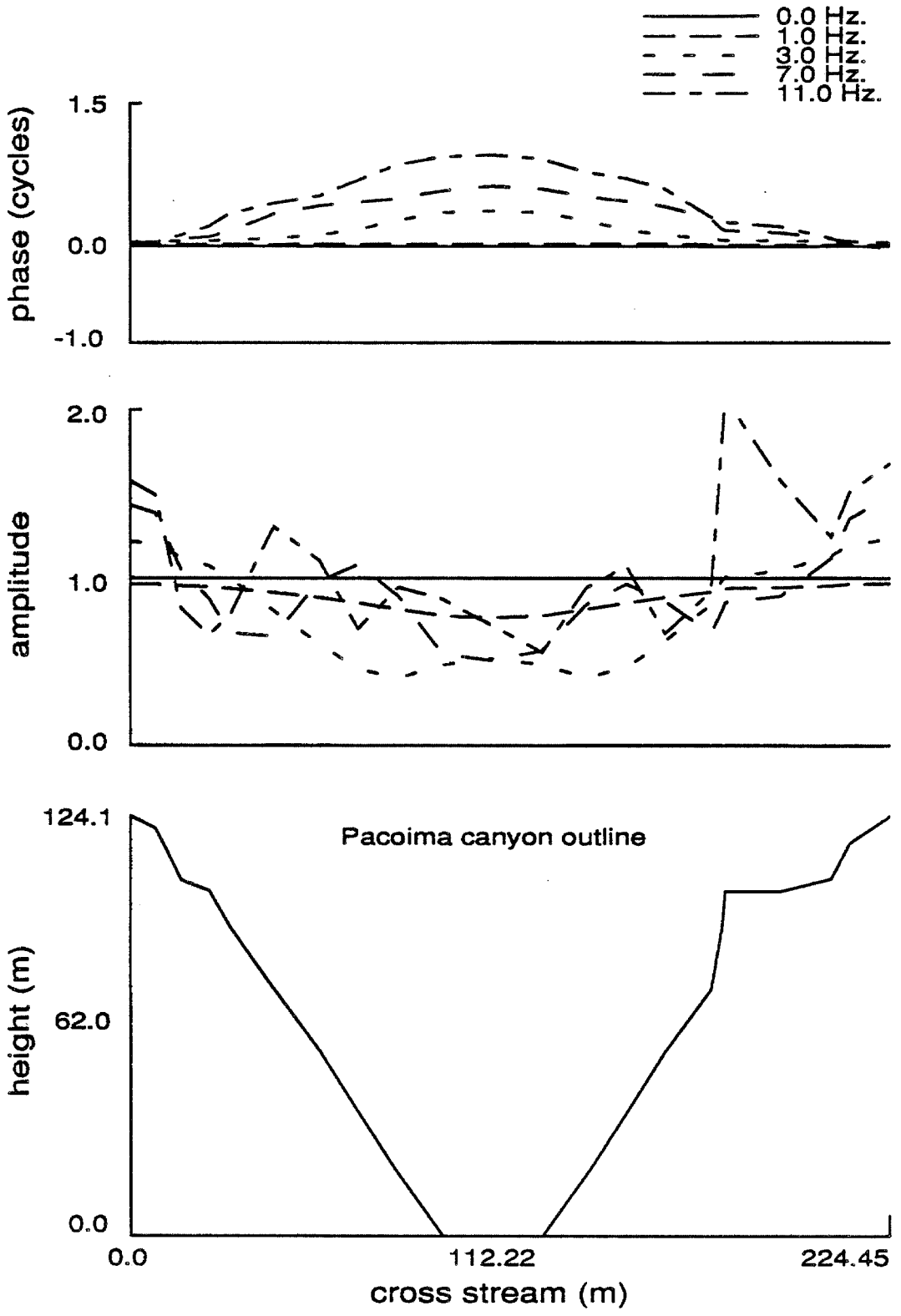

Figure 4.2b : stream free-field motions, Case SH0

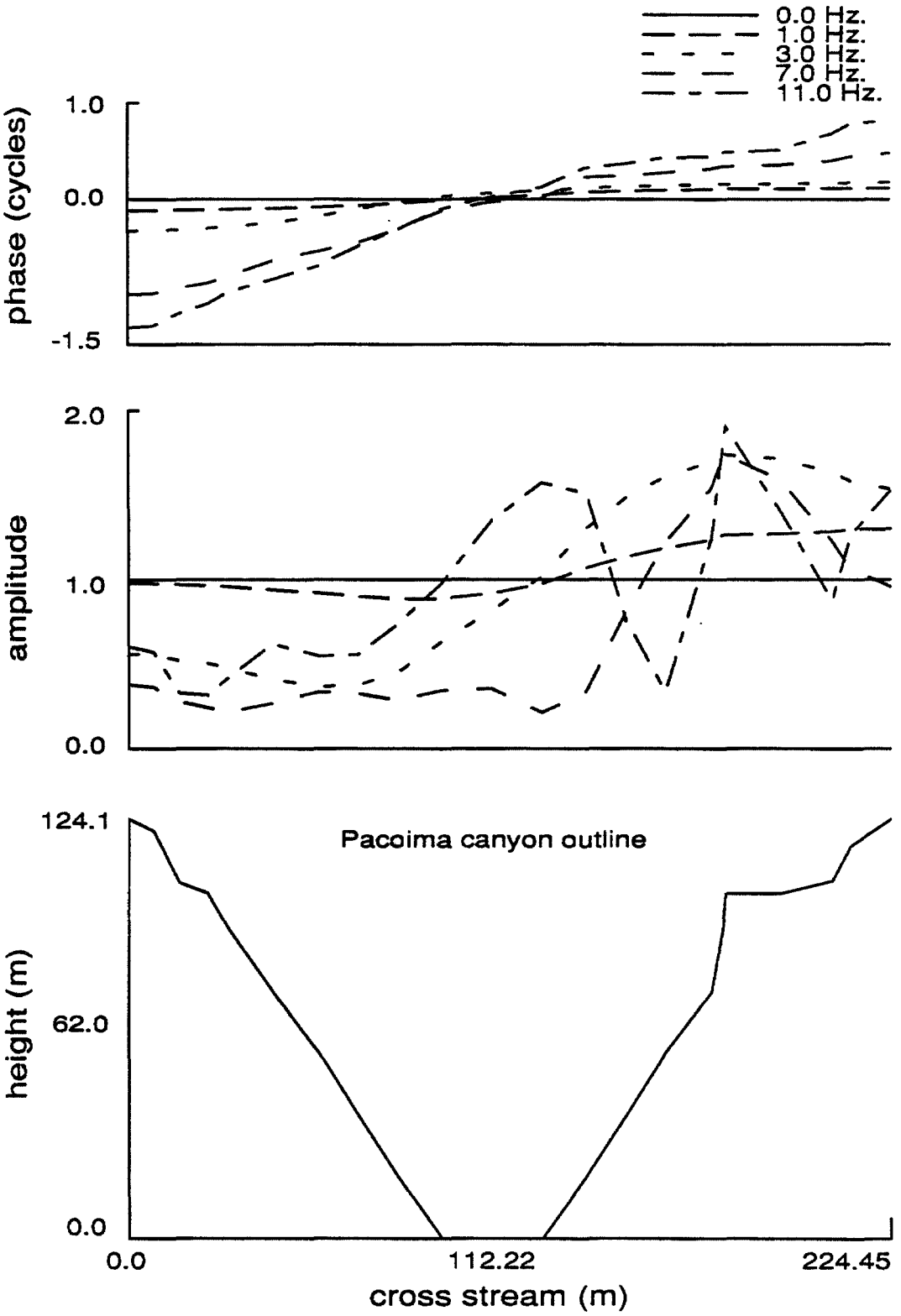

Figure 4.2c : stream free-field motions, Case SH60

Figure 4.3 : Cross-stream and vertical free-field motions (amplitude and phase variations) along Pacoima canyon for excitations given below.

Figure 4.3a : Excitation U-CV, cross-stream motions

Figure 4.3b : Excitation U-CV, vertical motions

Figure 4.3c : Excitation SVP0, cross-stream motions

Figure 4.3d : Excitation SVP0, vertical motions

Figure 4.3e : Excitation P60, cross-stream motions

Figure 4.3f : Excitation P60, vertical motions

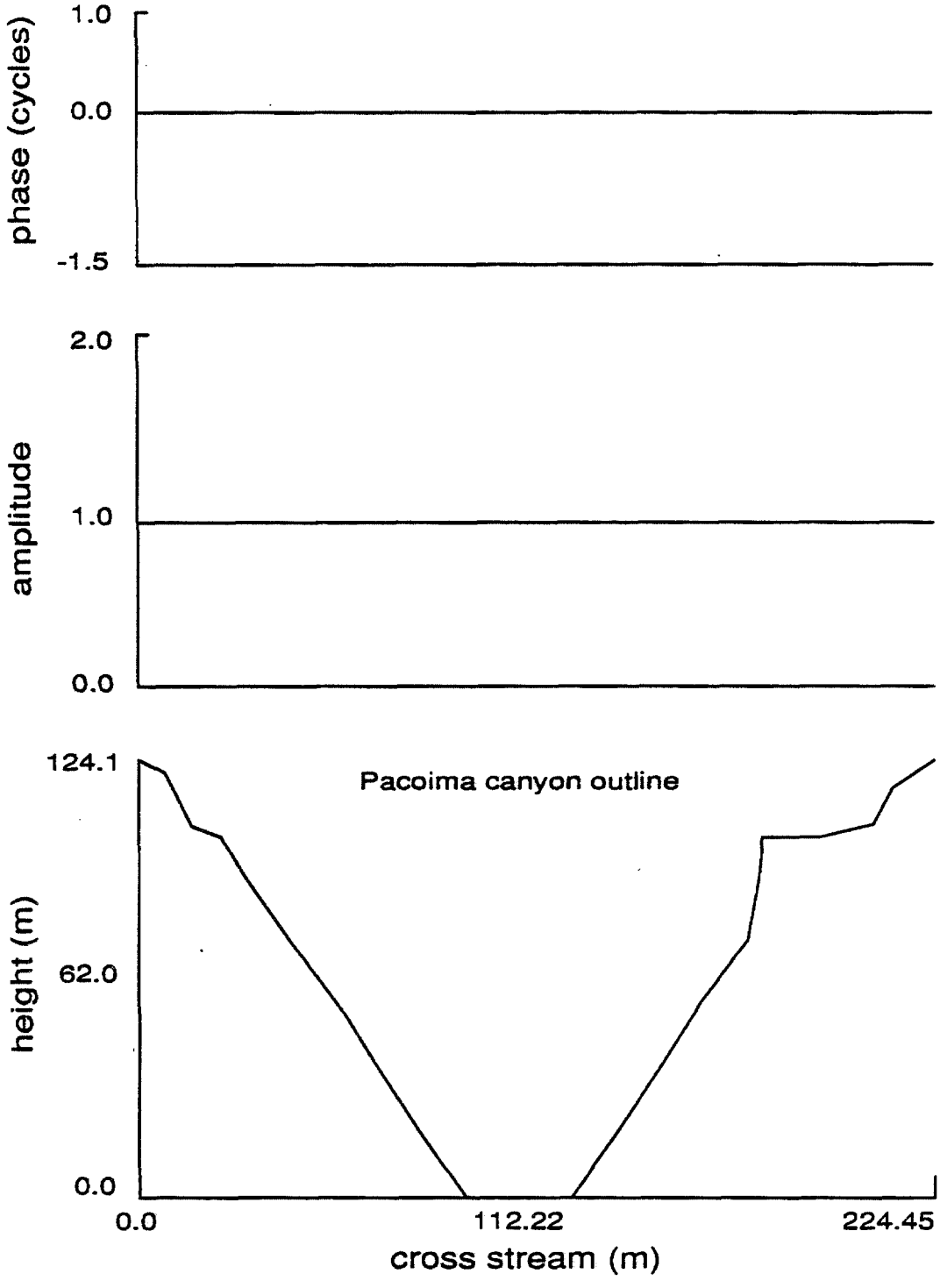

Figure 4.3a : cross-stream free-field motions, Case U-CV

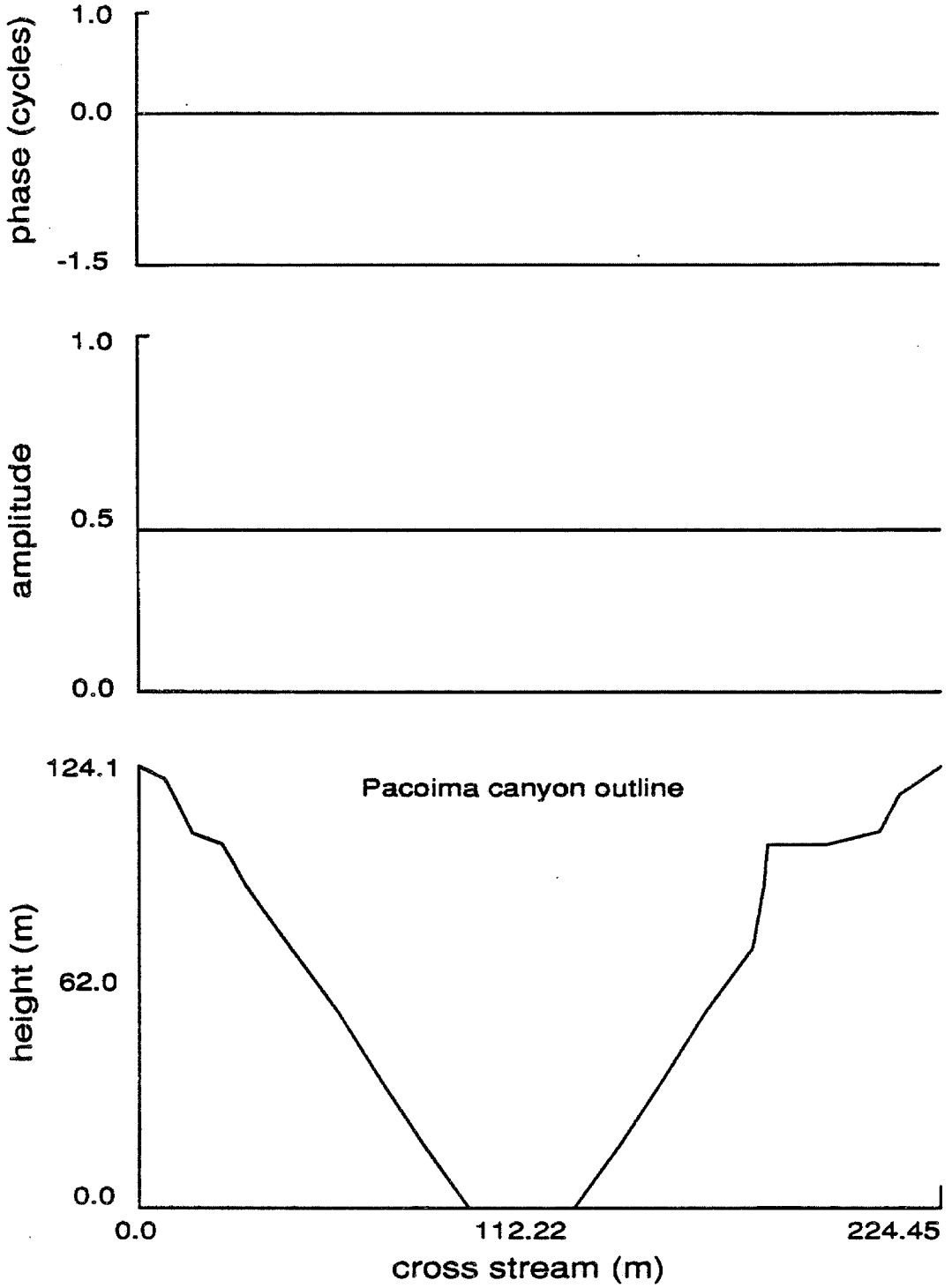

Figure 4.3b : vertical free-field motions, Case U-CV

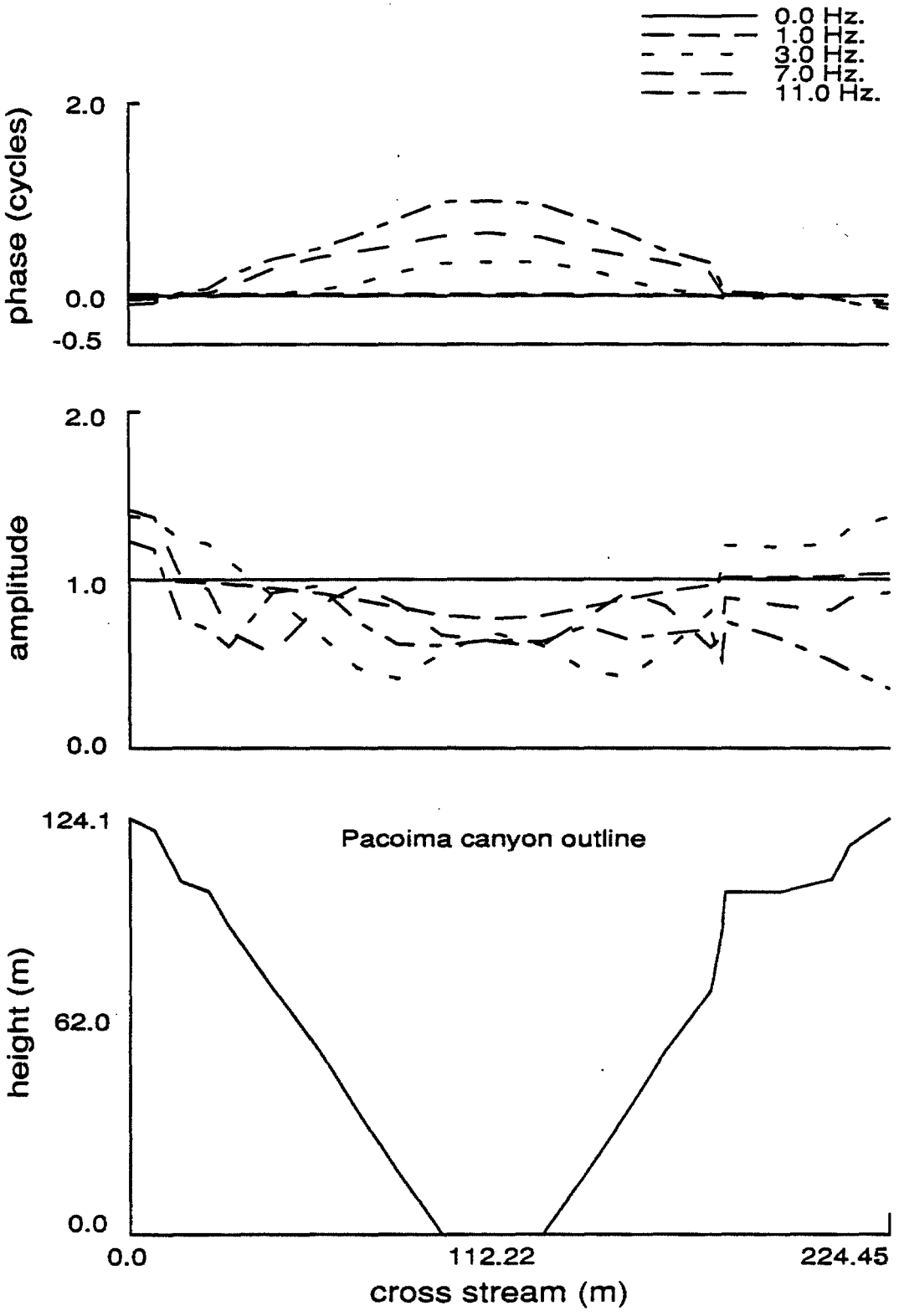

Figure 4.3c : cross-stream free-field motions, Case SVP0

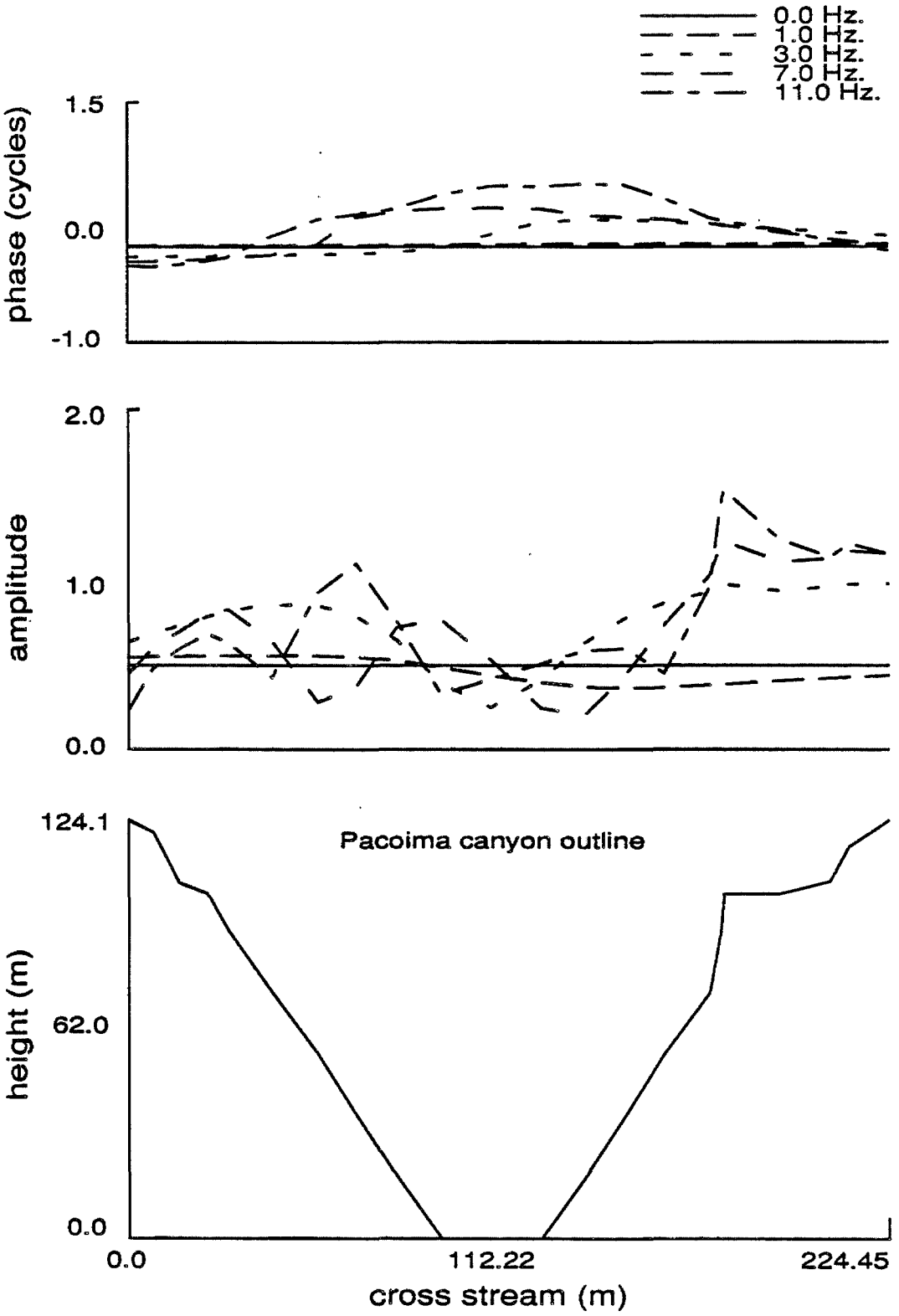

Figure 4.3d : vertical free-field motions, Case SVP0

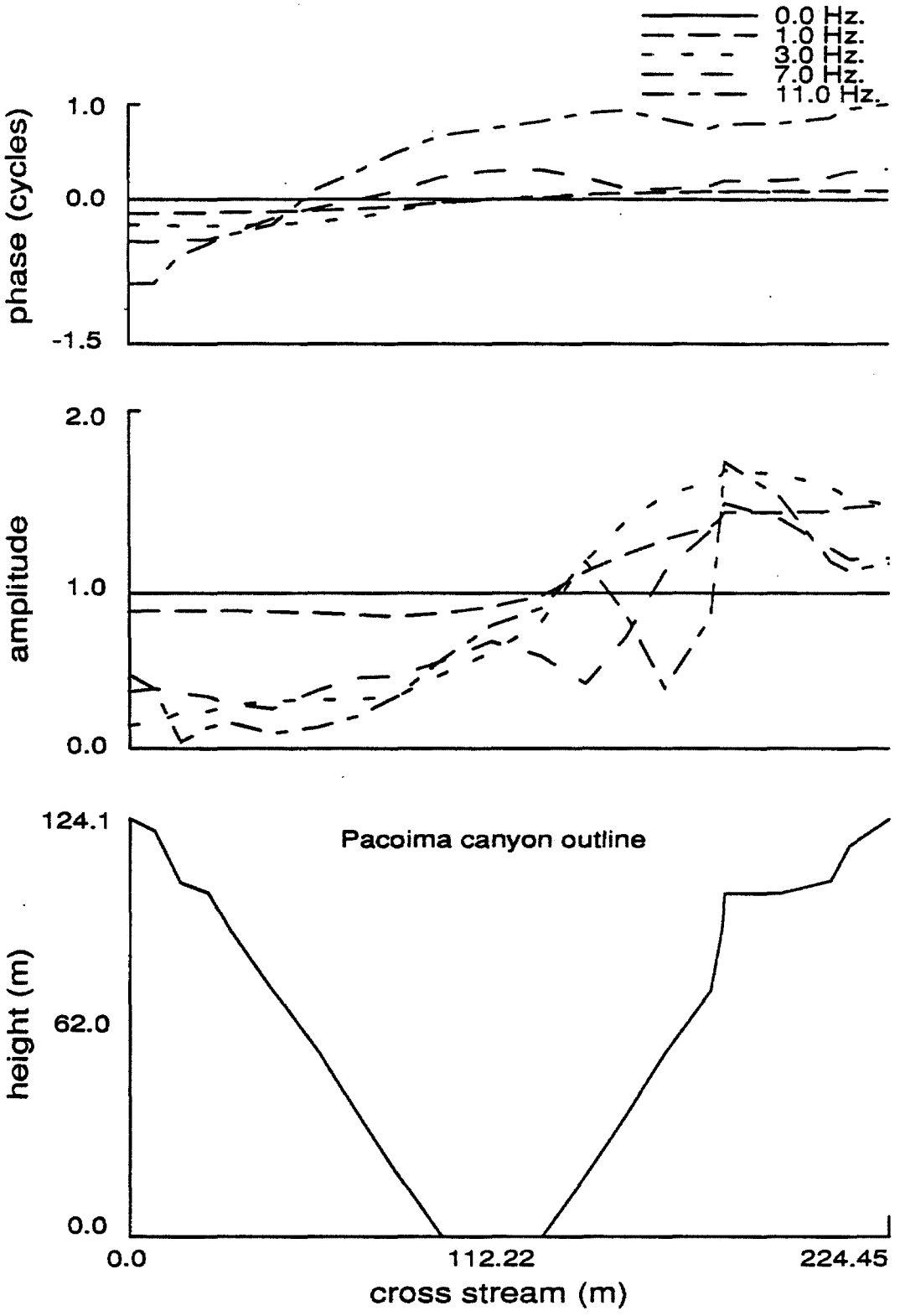

Figure 4.3e : cross-stream free-field motions, Case P60

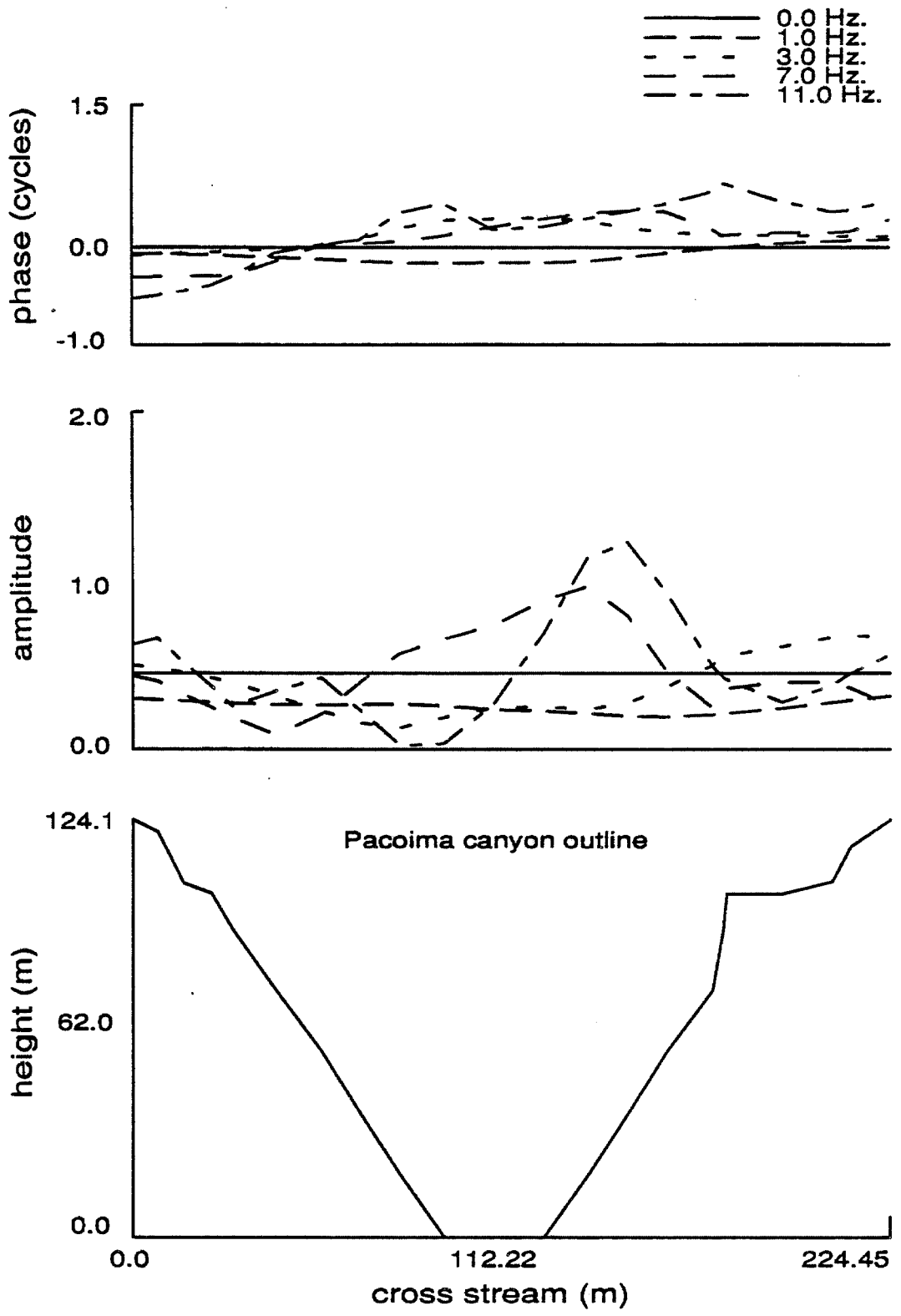

Figure 4.3f : vertical free-field motions, Case P60

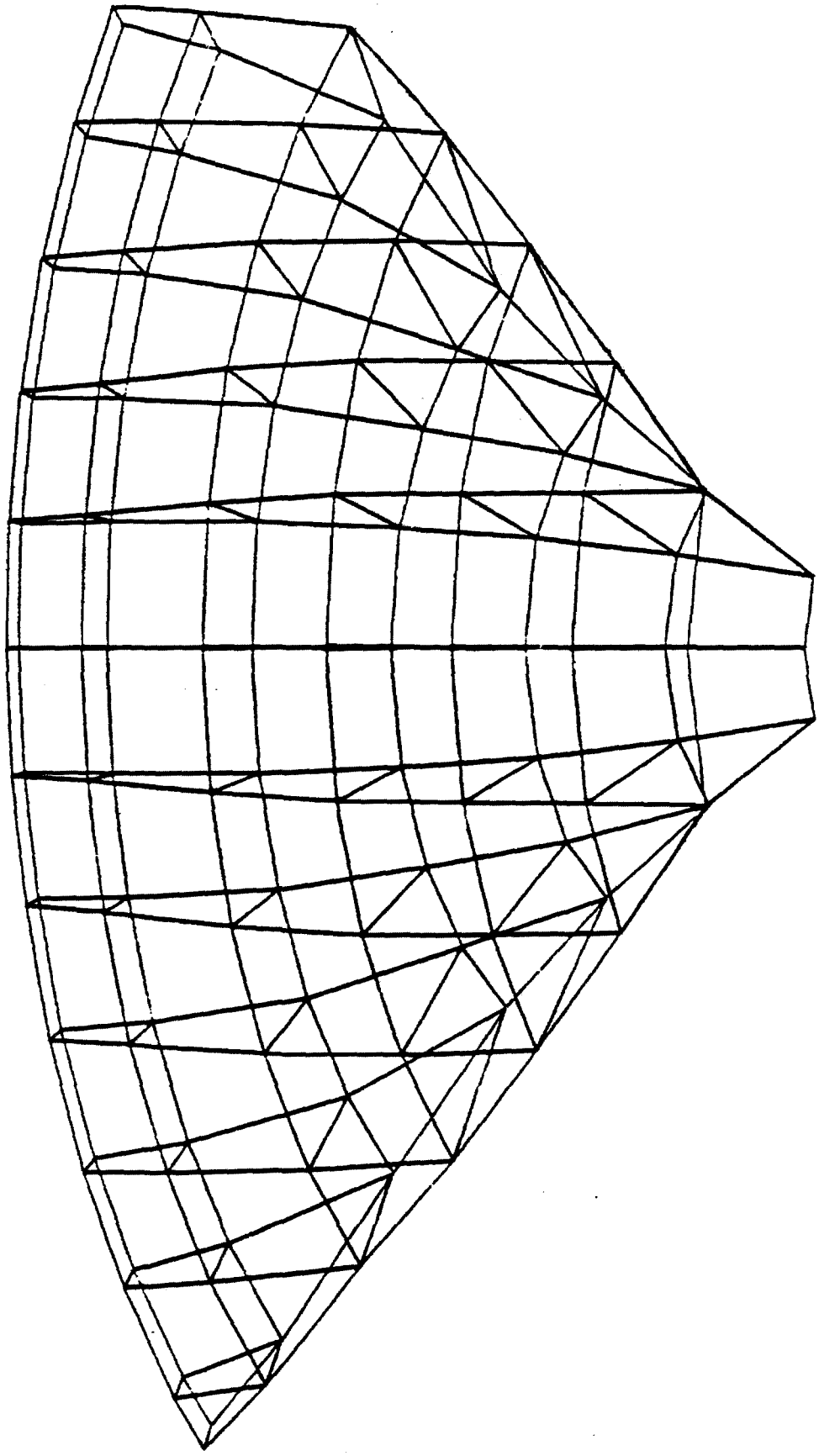

Figure 4.4 : Dam mesh

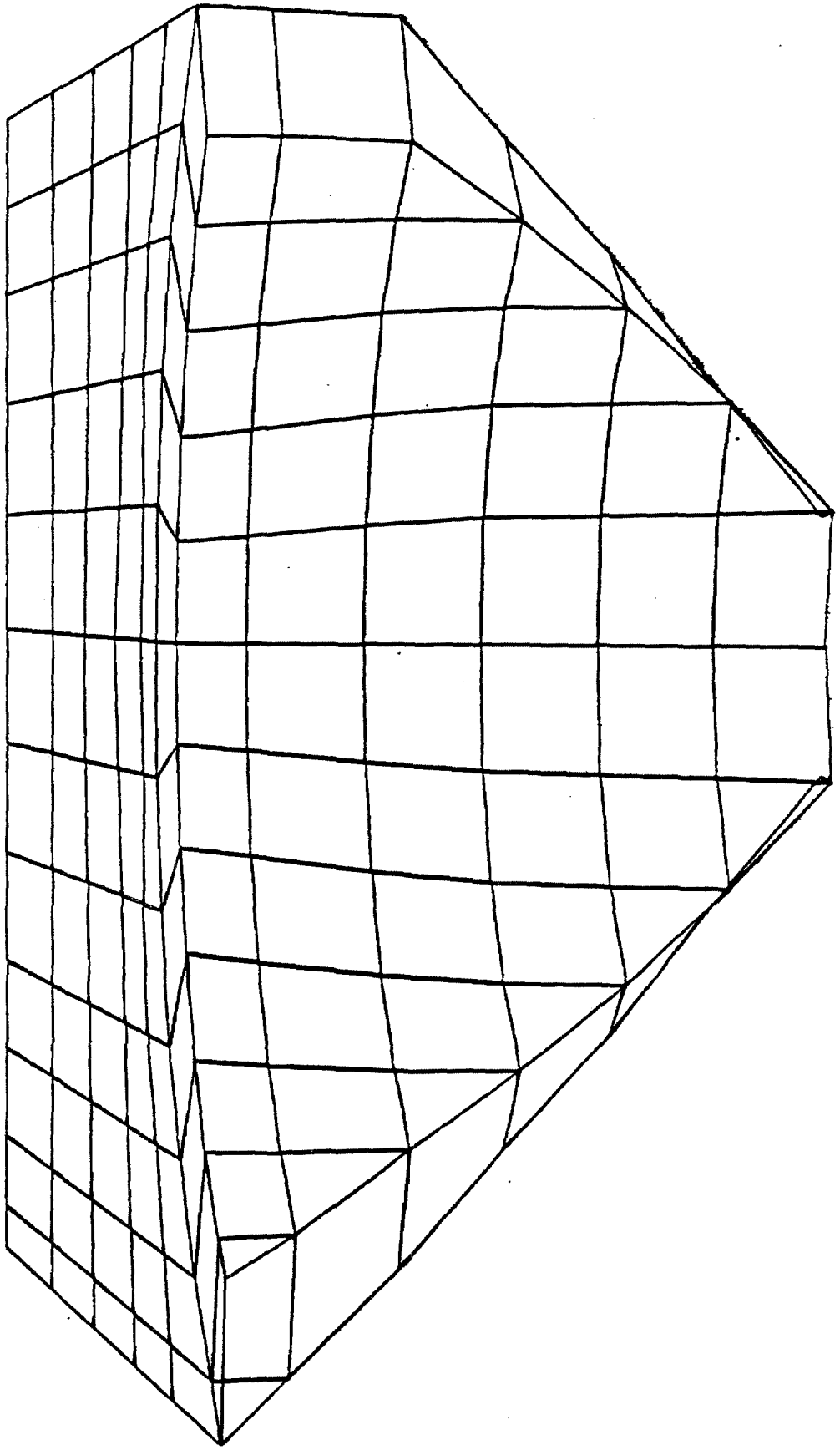

Figure 4.5 : Water mesh

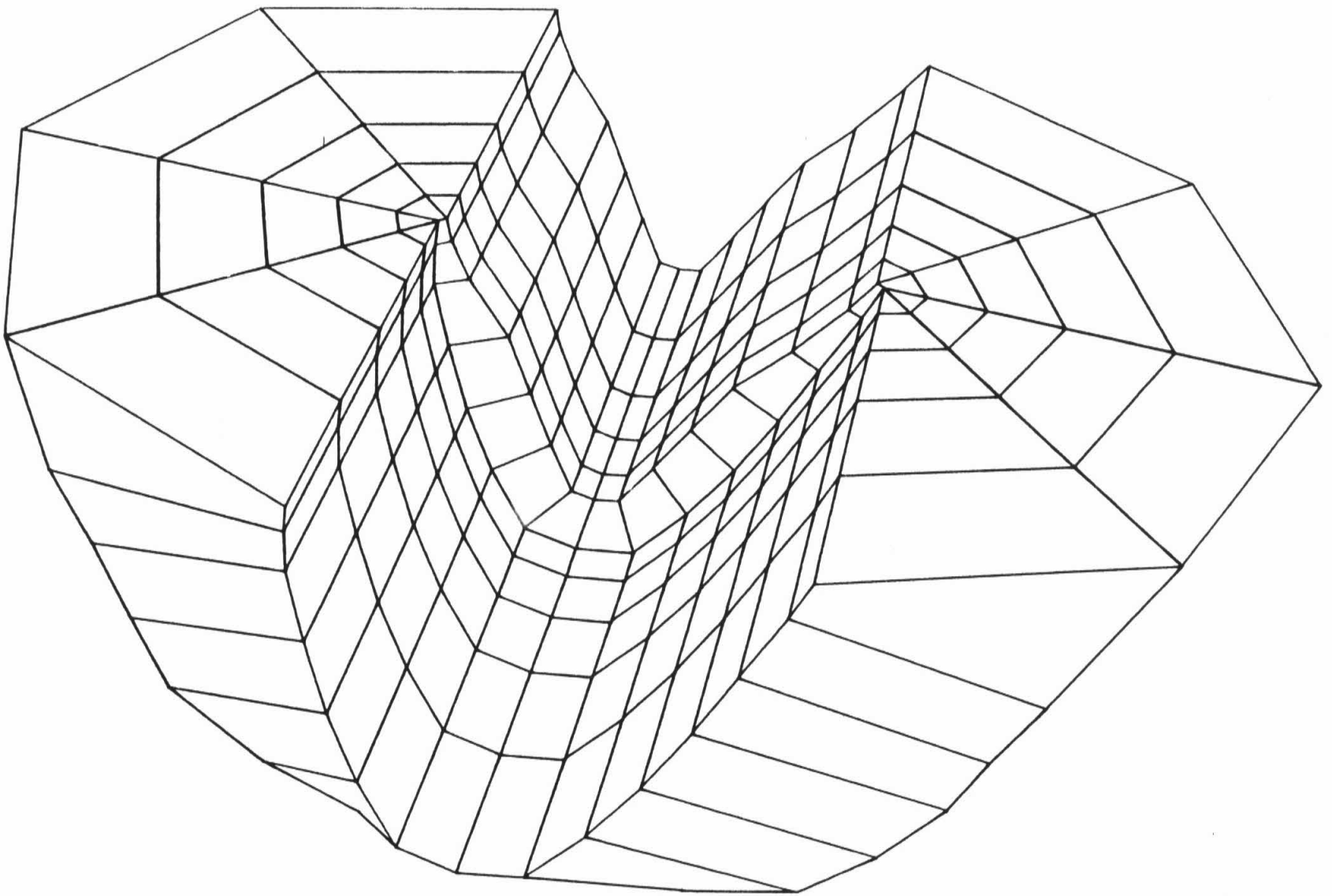

Figure 4.6 : Foundation mesh

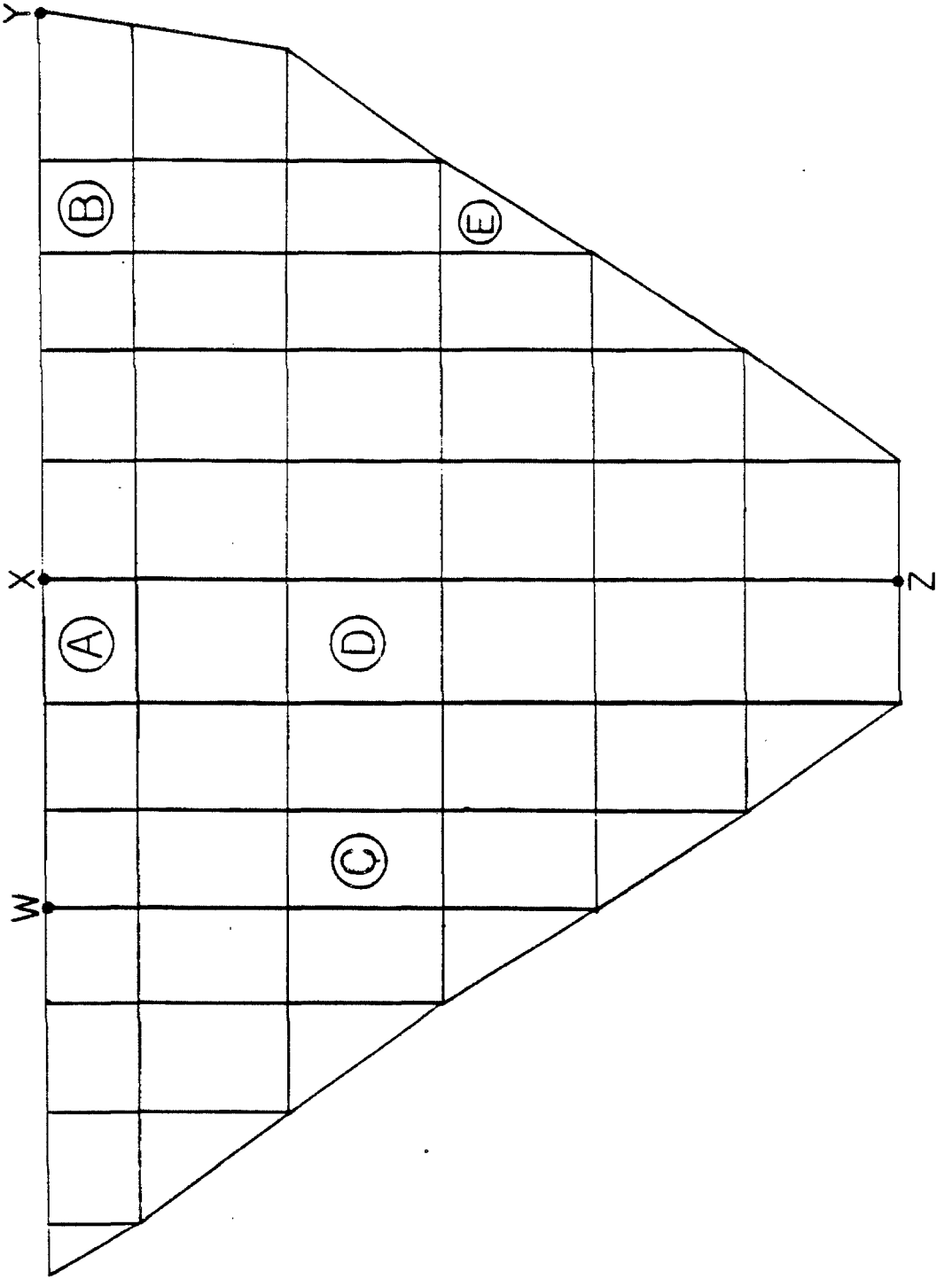

Figure 4.7 : Key for dam responses

Figure 4.8 : Frequency domain responses of Pacoima dam for excitations in the stream direction, no water. Excitation amplitudes from Table 2.1 times 1g.

Figure 4.8a : Radial acceleration at node W

Figure 4.8b : Radial acceleration at node X

Figure 4.8c : Stream acceleration at node Y

Figure 4.8d : Stream acceleration at node Z

Figure 4.8e : Upstream arch stress in element A

Figure 4.8f : Downstream arch stress in element B

Figure 4.8g : Downstream arch stress in element E

Figure 4.8h : Downstream cantilever stress in element C

Figure 4.8i : Upstream cantilever stress in element D

Figure 4.8j : Upstream cantilever stress in element E

Key to graphs :

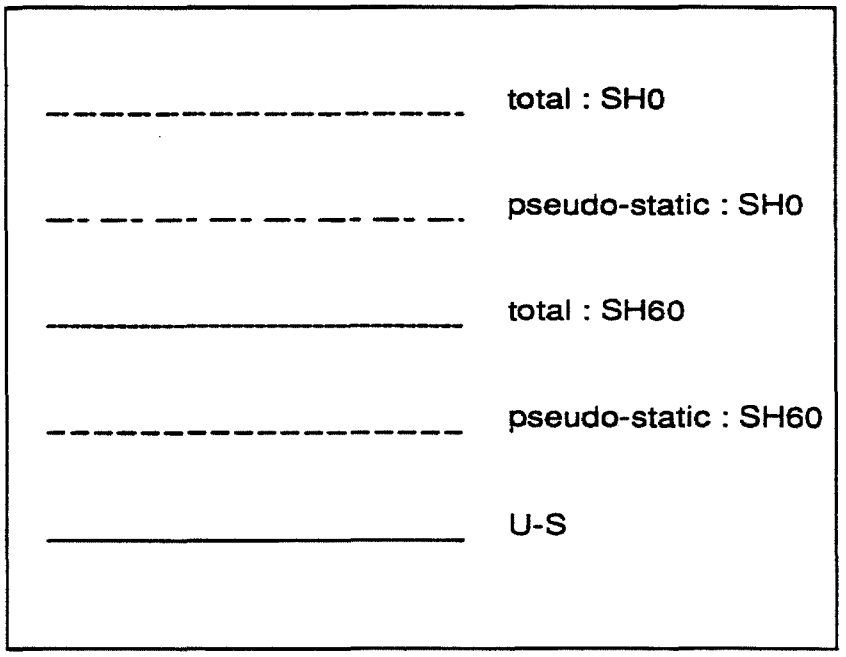

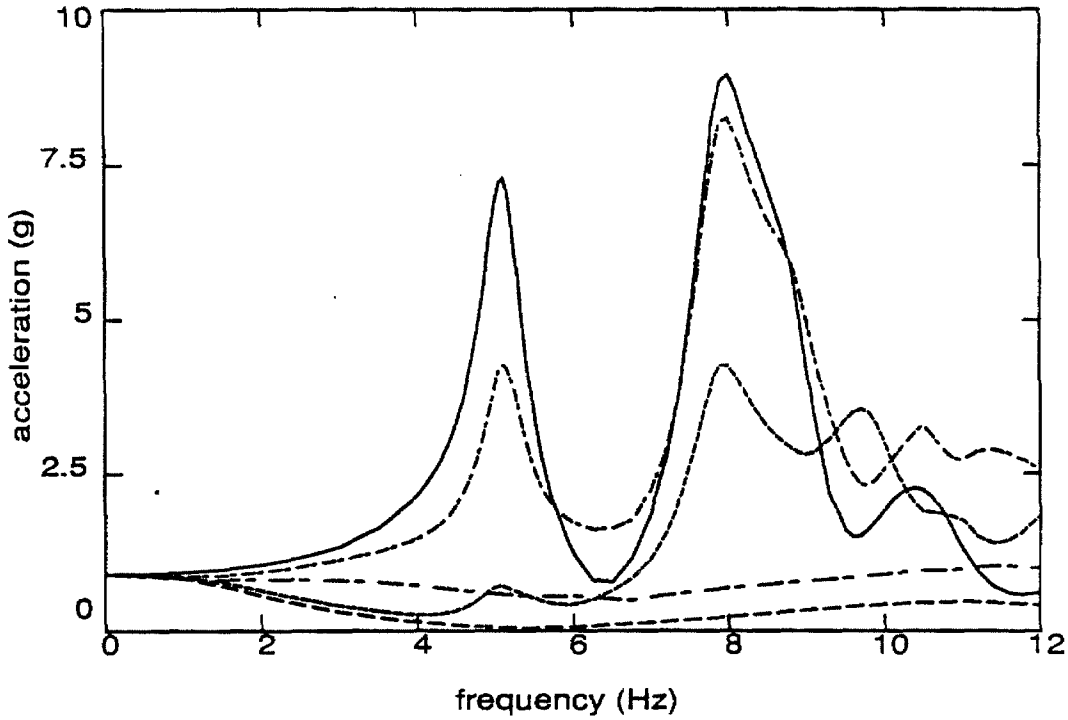

Figure 4.8a : Radial acceleration at node W

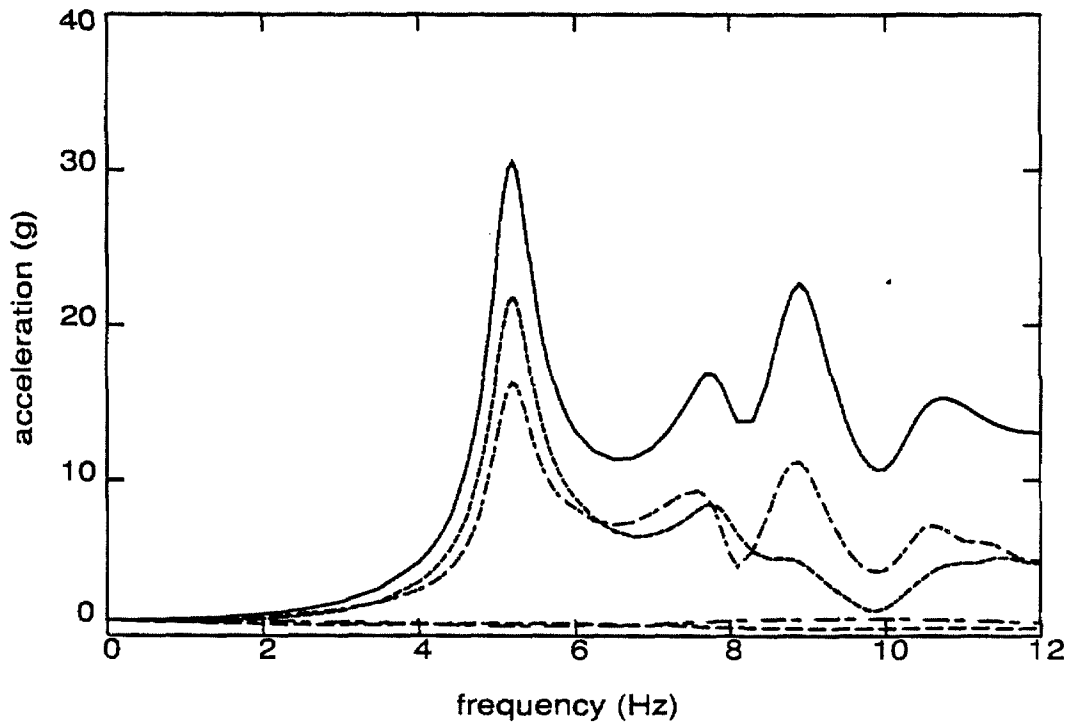

Figure 4.8b : Radial acceleration at node X

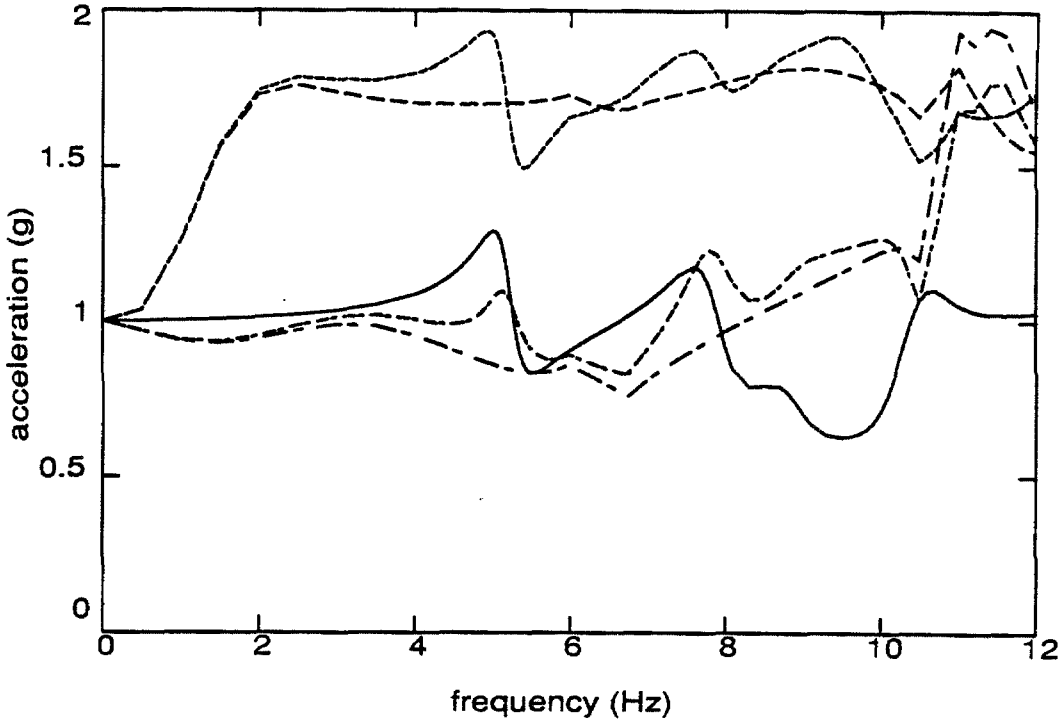

Figure 4.8c : Stream acceleration at node Y

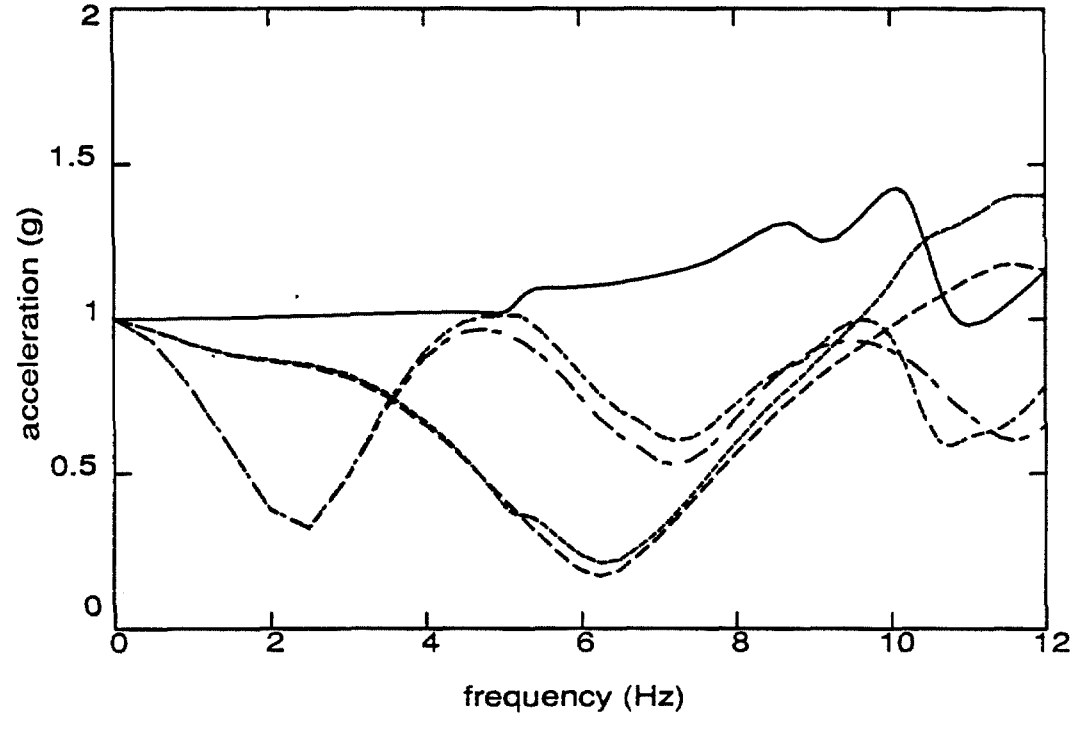

Figure 4.8d : Stream acceleration at node Z

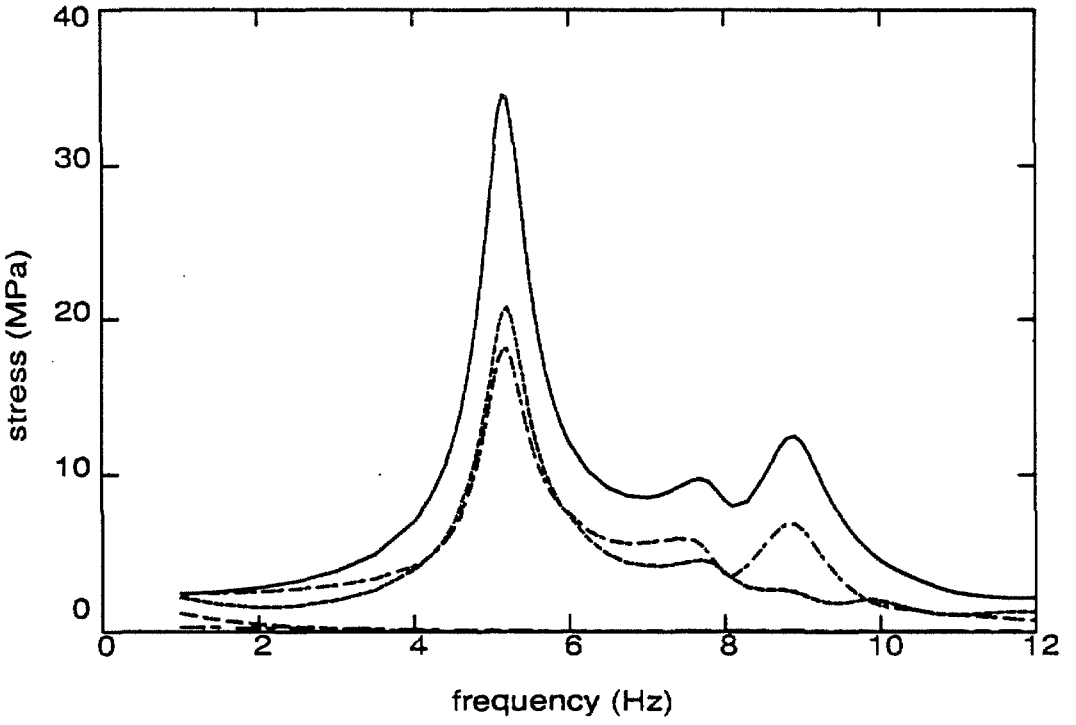

Figure 4.8e : Upstream arch stress in element A

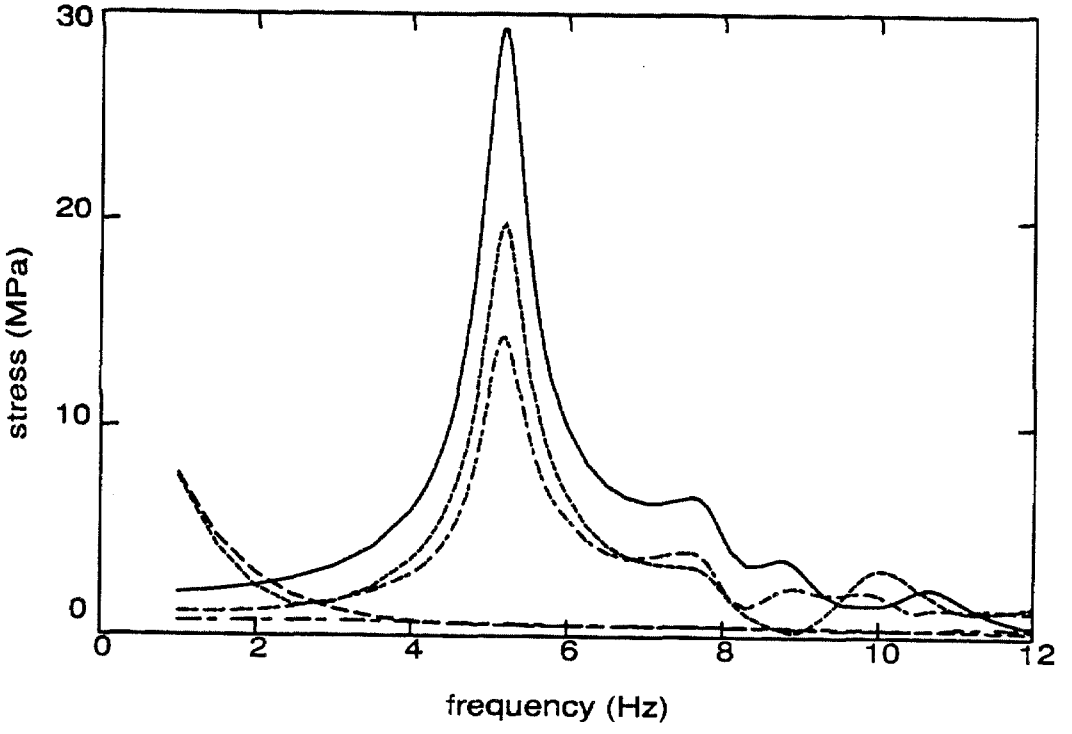

Figure 4.8f : Downstream arch stress in element B

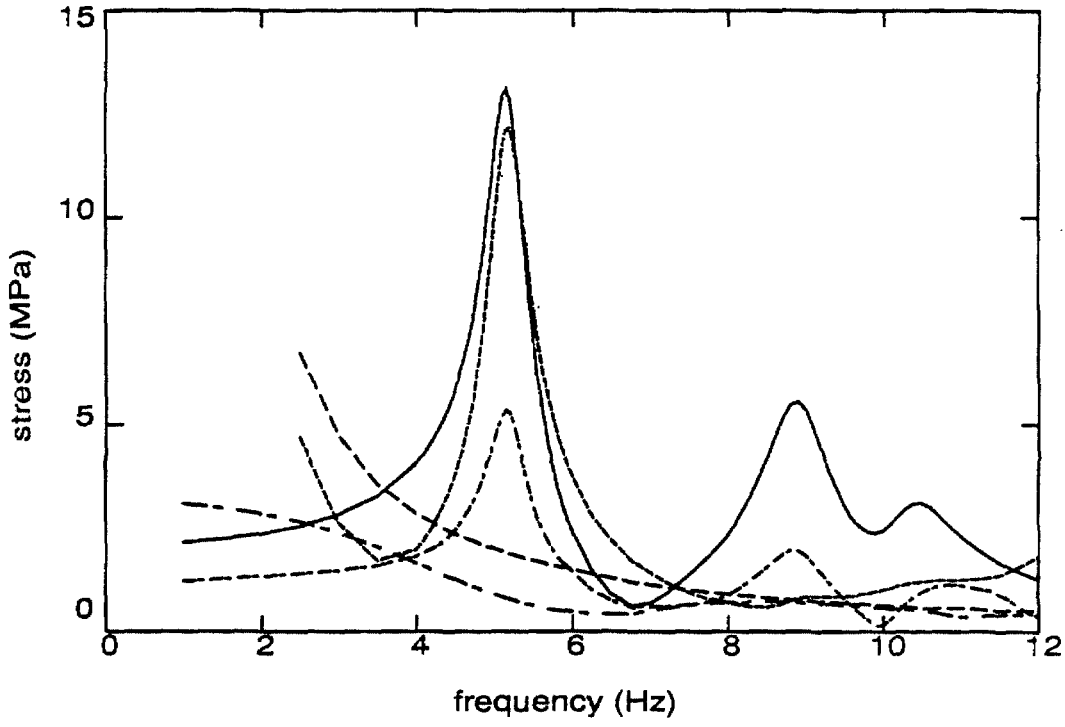

Figure 4.8g : Downstream arch stress in element E

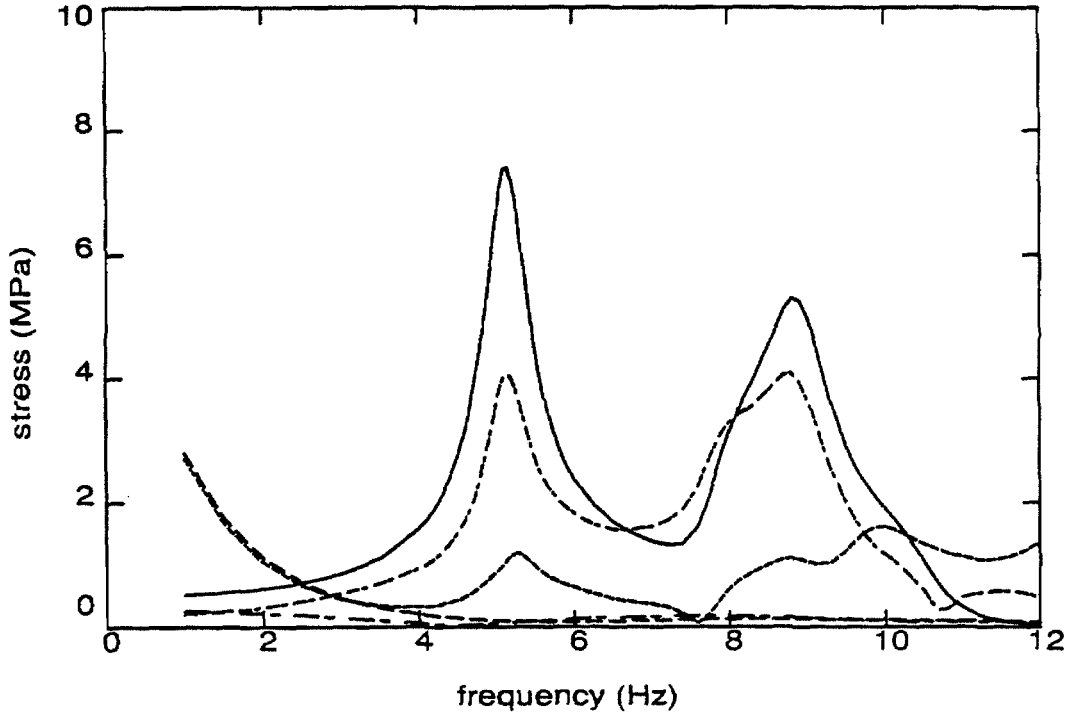

Figure 4.8h : Downstream cantilever stress in element C

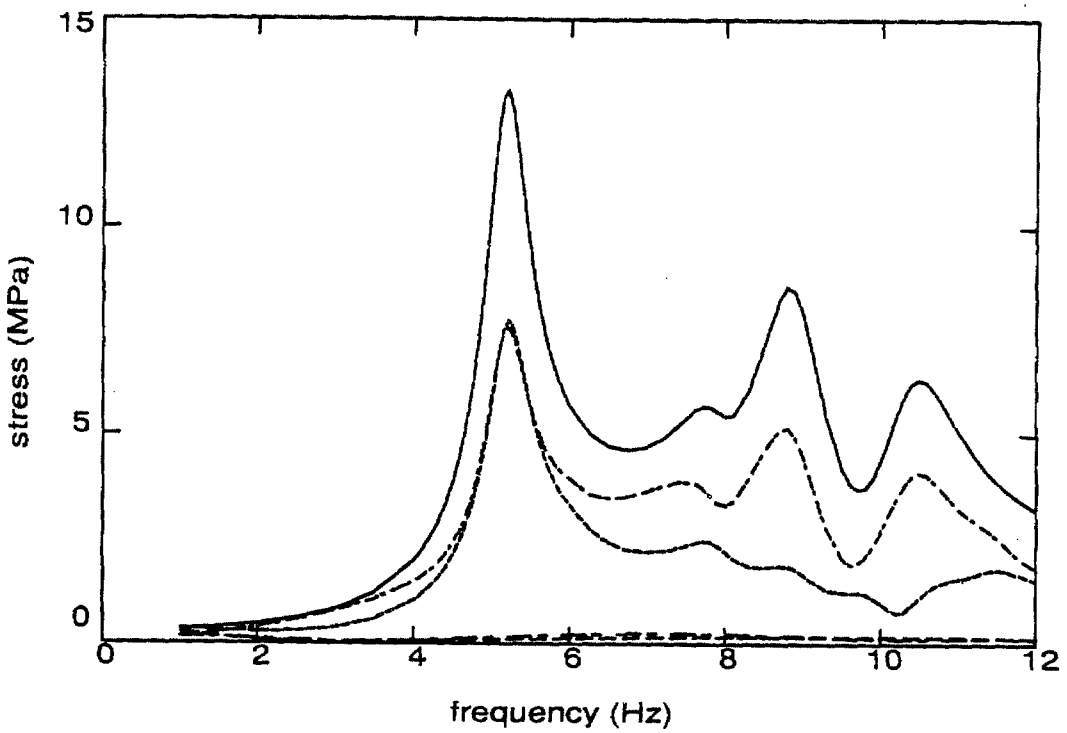

Figure 4.8i : Upstream cantilever stress in element D

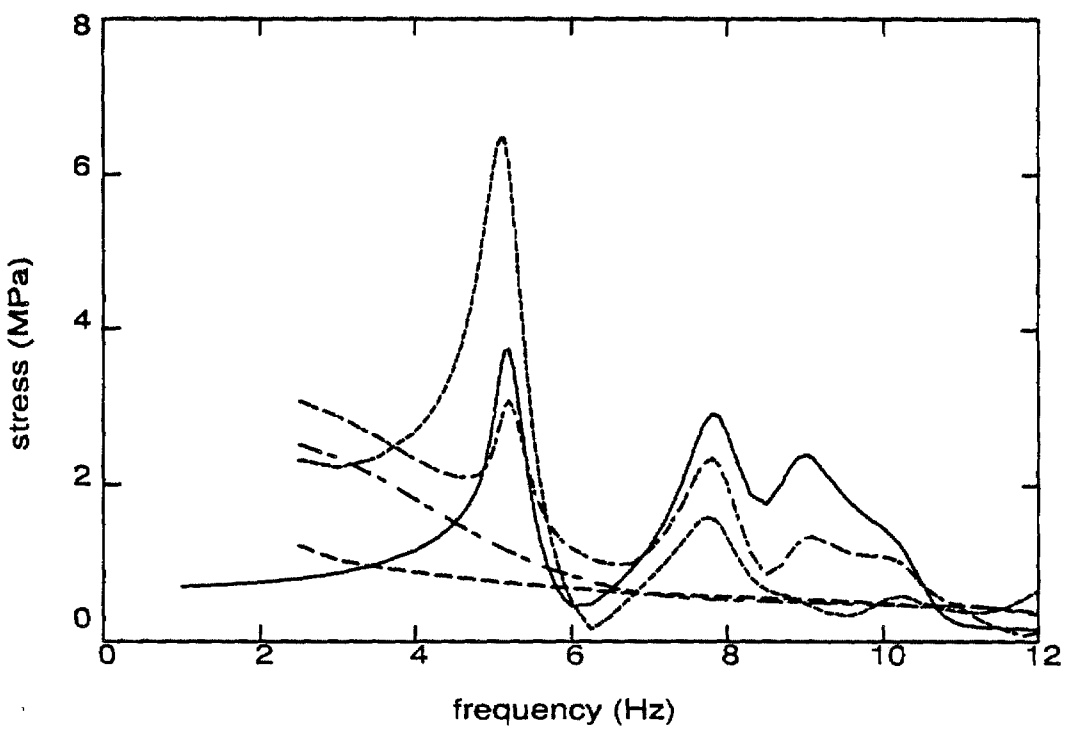

Figure 4.8j : Upstream cantilever stress in element E

Figure 4.9 : Frequency domain responses of Pacoima dam for excitations in the cross-stream and vertical directions, no water. Excitation amplitudes from Table 2.1 times 1g.

Figure 4.9a : Radial acceleration at node W

Figure 4.9b : Radial acceleration at node X

Figure 4.9c : Stream acceleration at node Y

Figure 4.9d : Stream acceleration at node Z

Figure 4.9e : Upstream arch stress in element A

Figure 4.9f : Downstream arch stress in element B

Figure 4.9g : Downstream arch stress in element E

Figure 4.9h : Downstream cantilever stress in element C

Figure 4.9i : Upstream cantilever stress in element D

Figure 4.9j : Upstream cantilever stress in element E

Key to graphs :

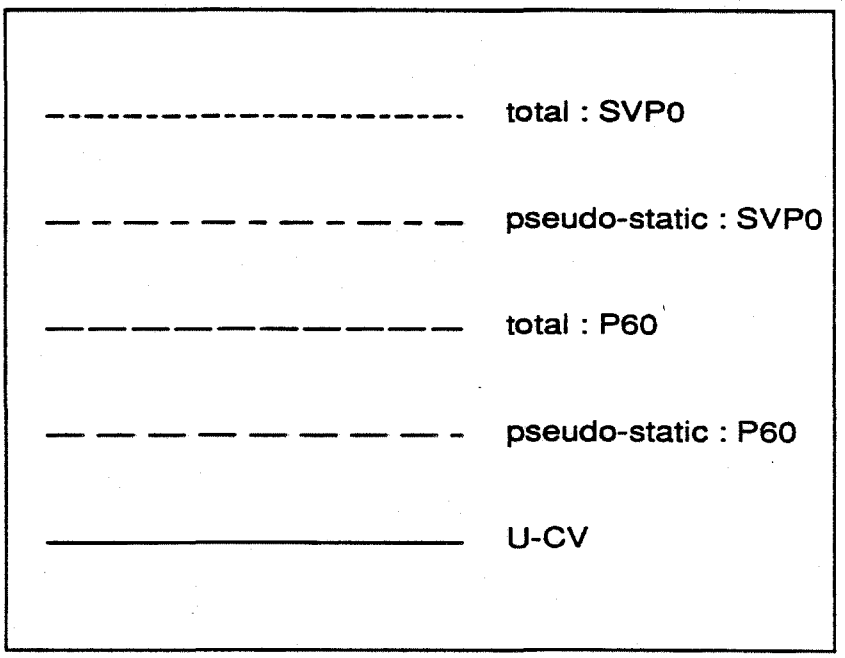

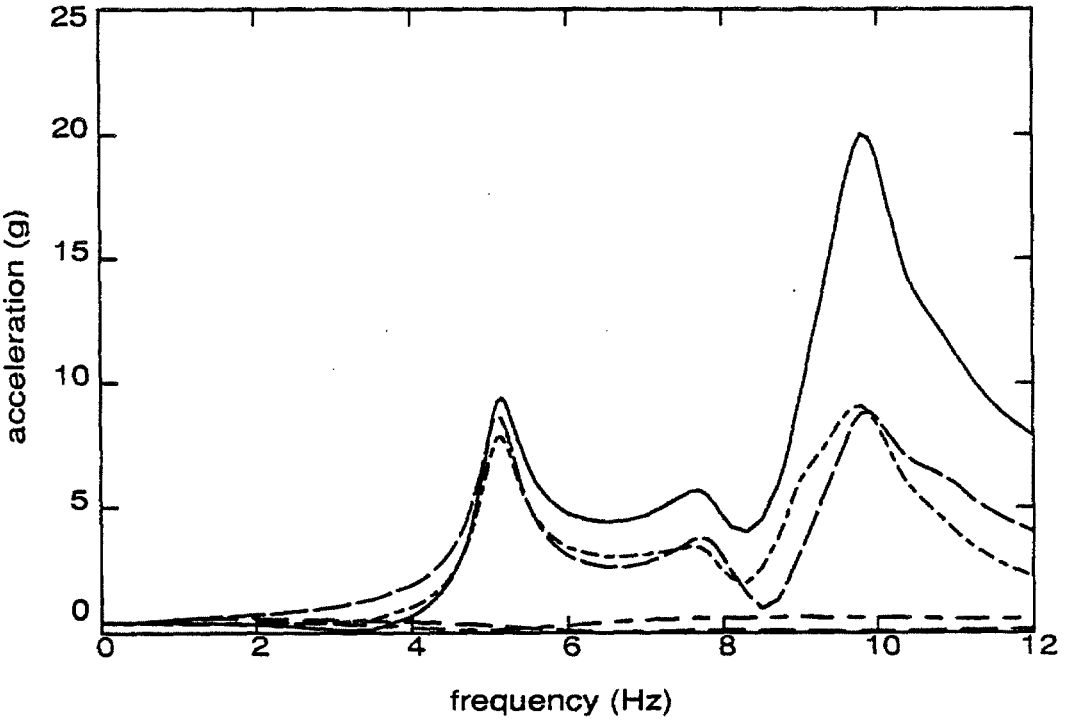

Figure 4.9a : Radial acceleration at node W

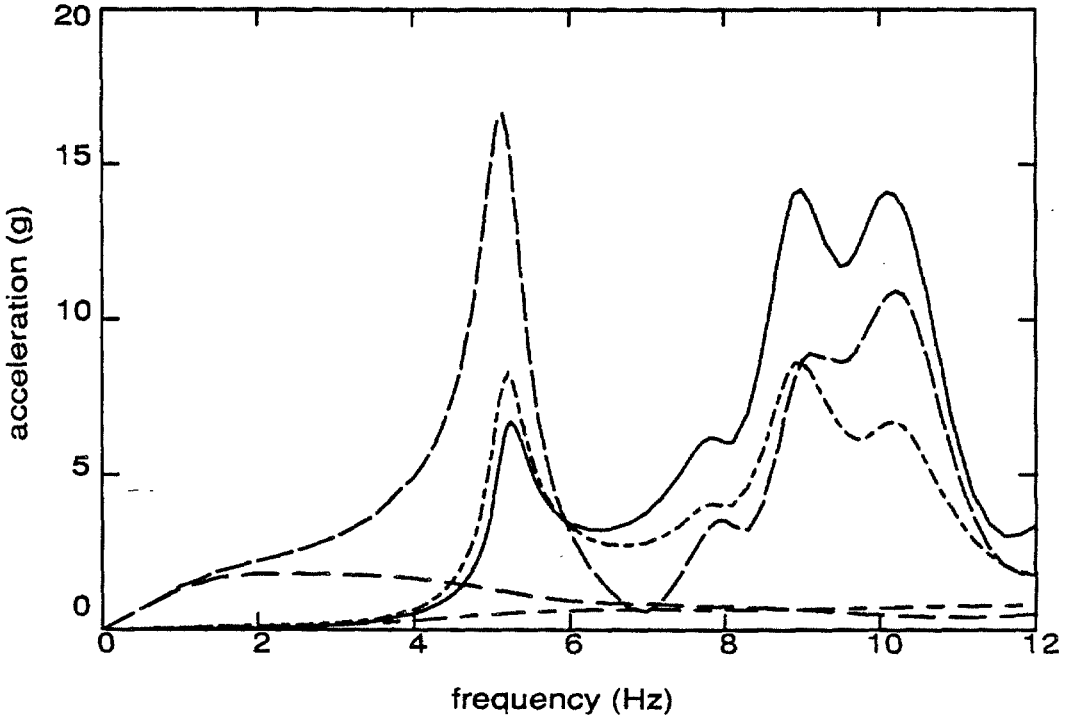

Figure 4.9b : Radial acceleration at node X

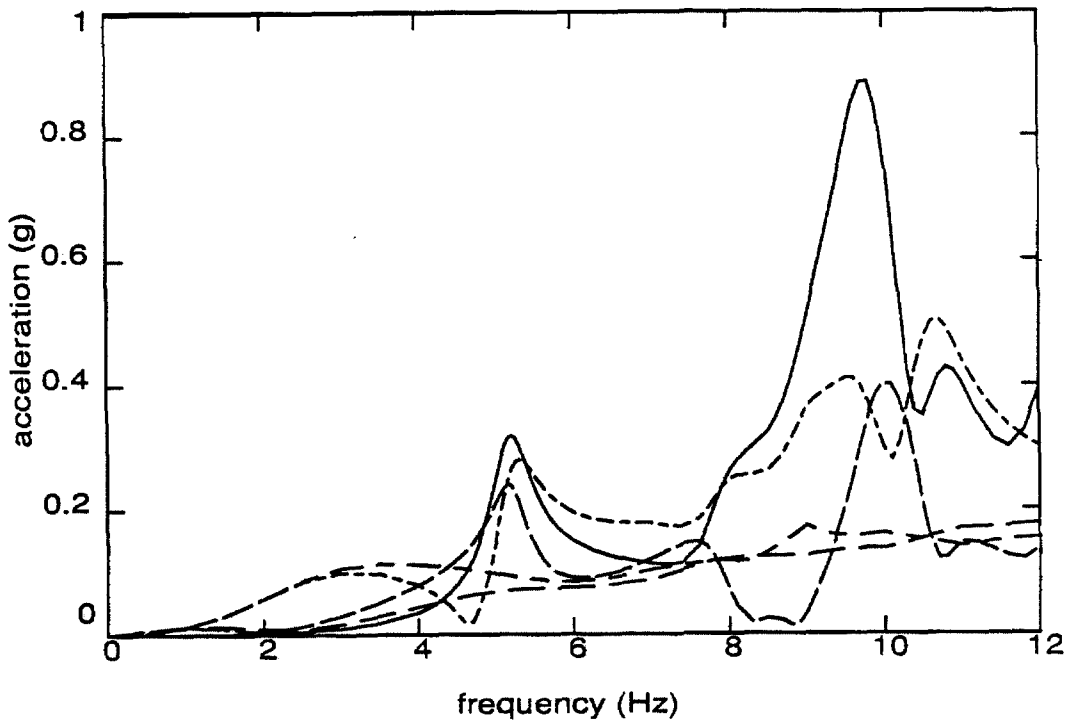

Figure 4.9c : Stream acceleration at node Y

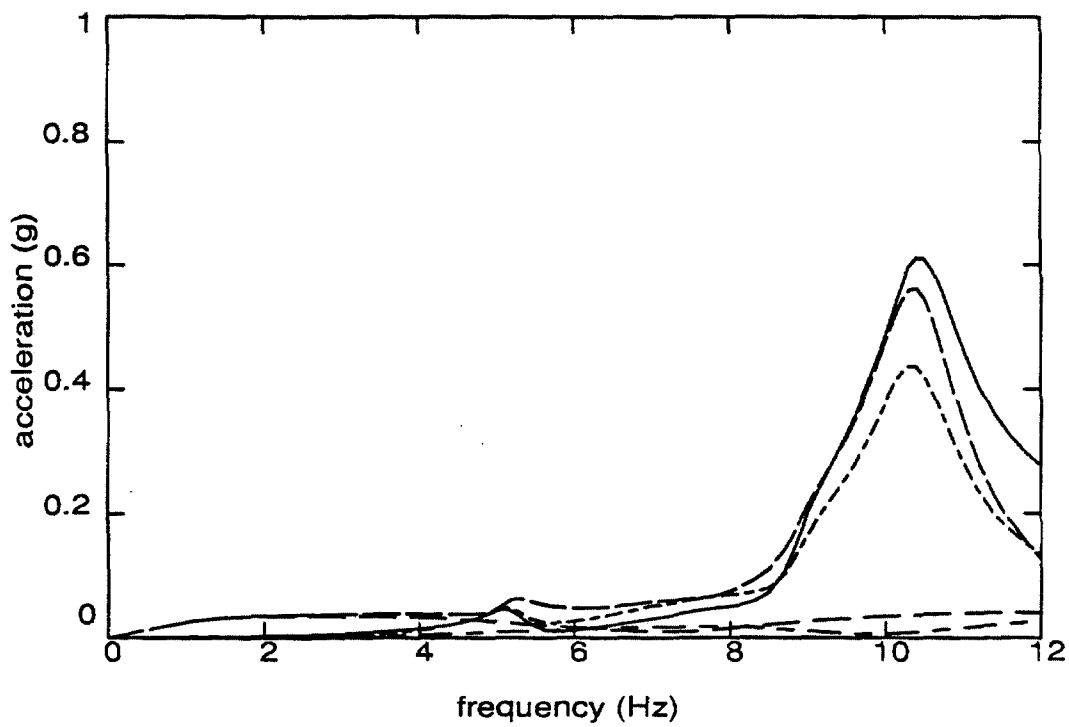

Figure 4.9d : Stream acceleration at node Z

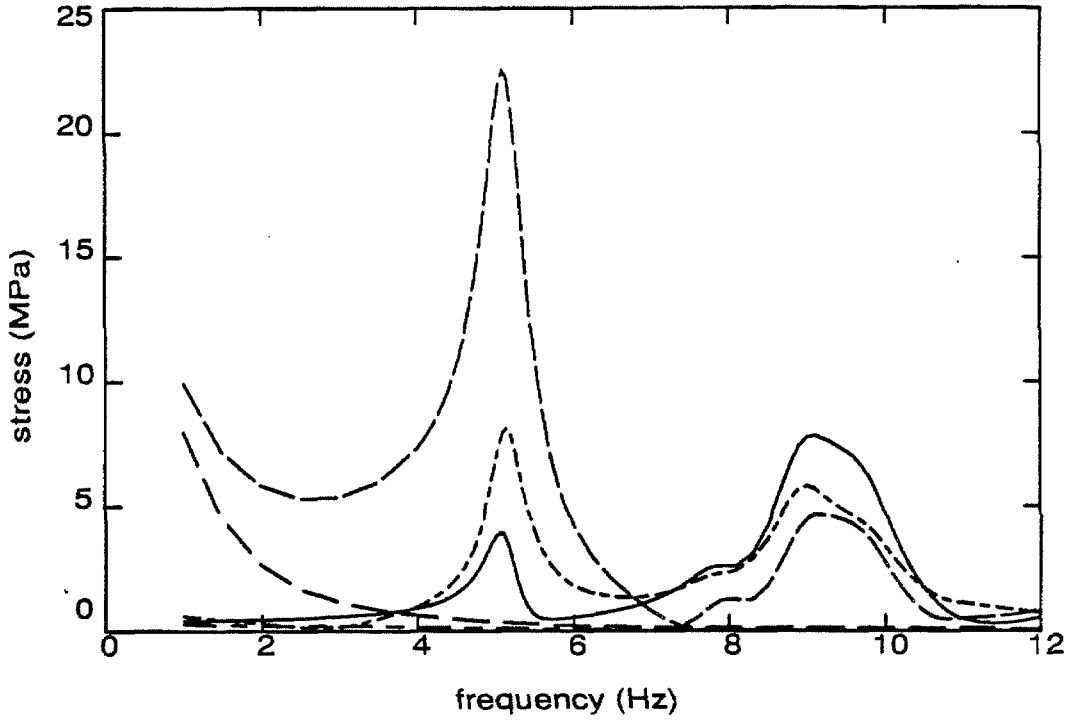

Figure 4.9e : Upstream arch stress in element A

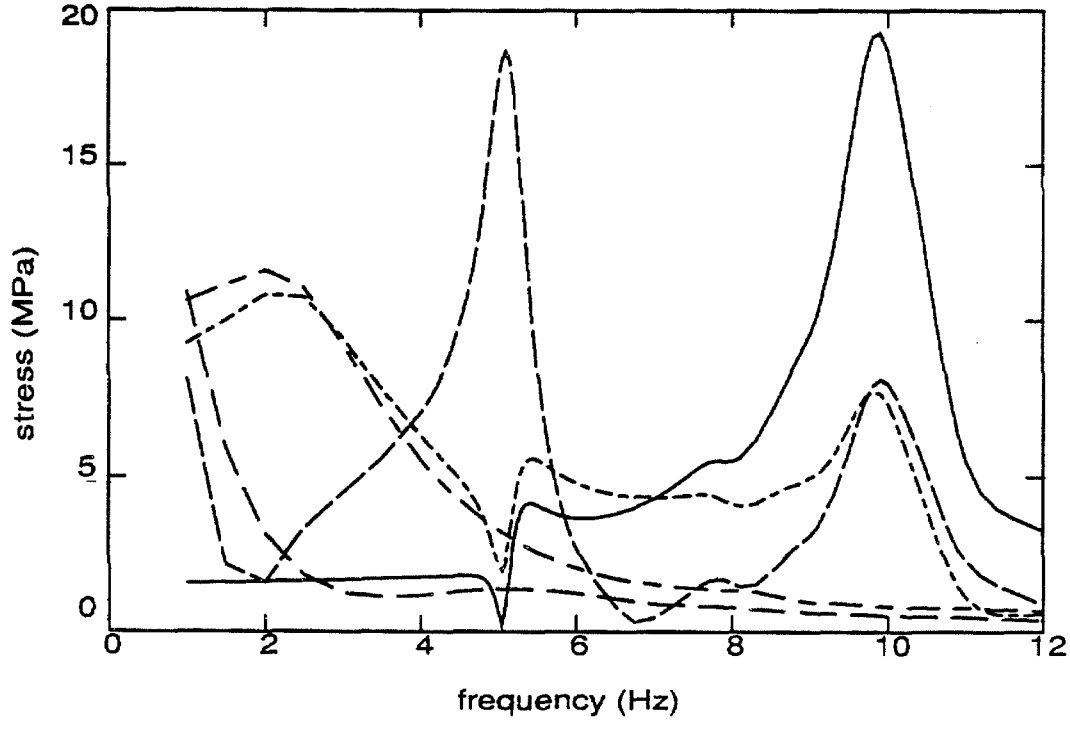

Figure 4.9f : Downstream arch stress in element B

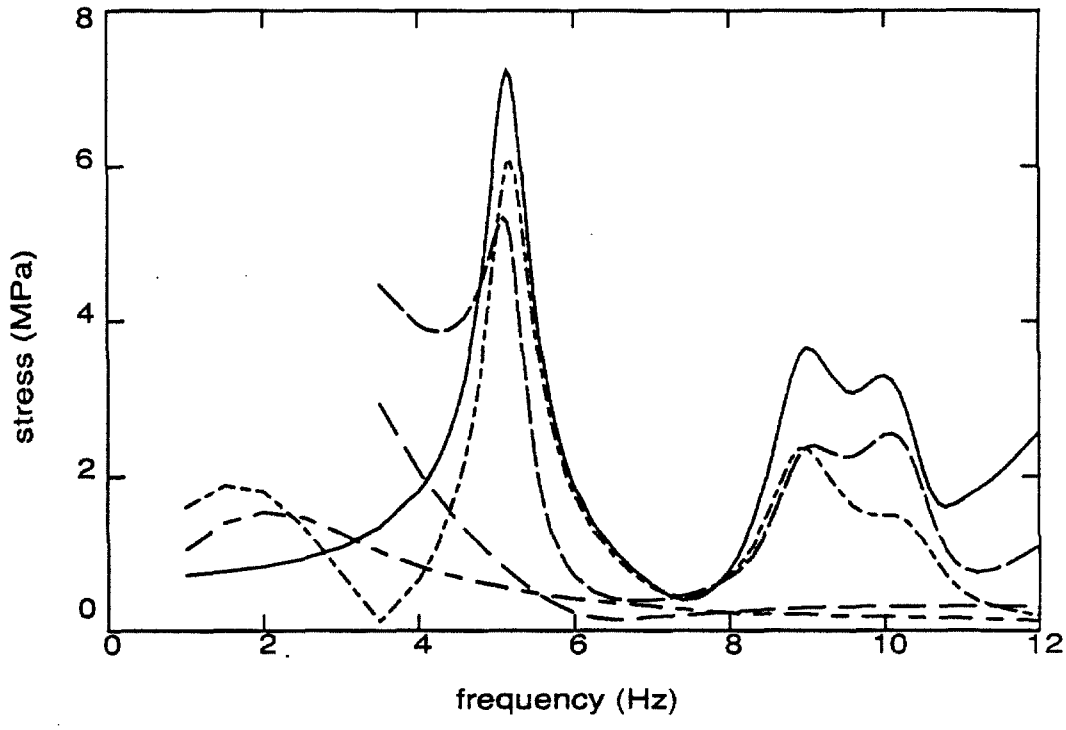

Figure 4.9g : Downstream arch stress in element E

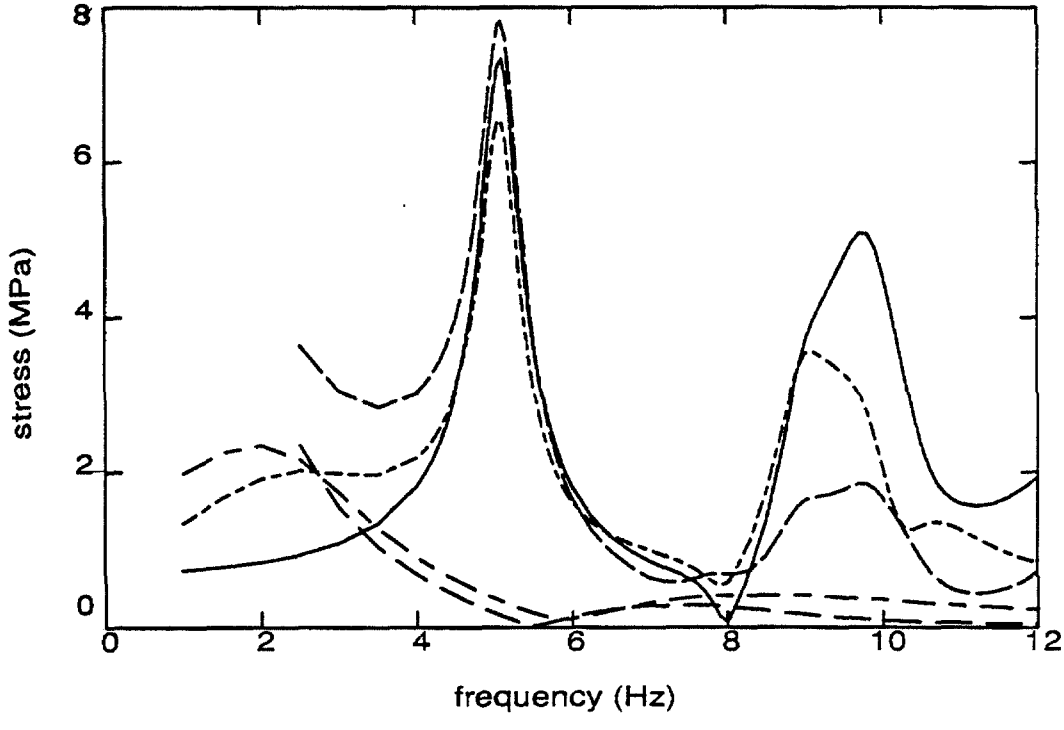

Figure 4.9h : Downstream cantilever stress in element C

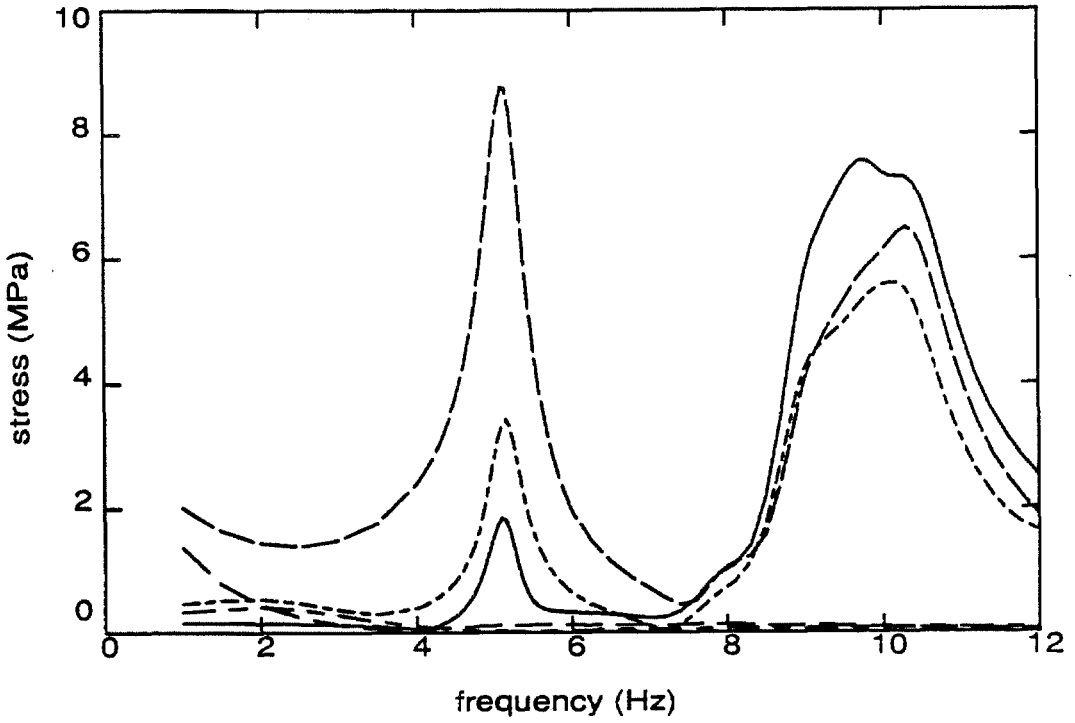

Figure 4.9i : Upstream cantilever stress in element D

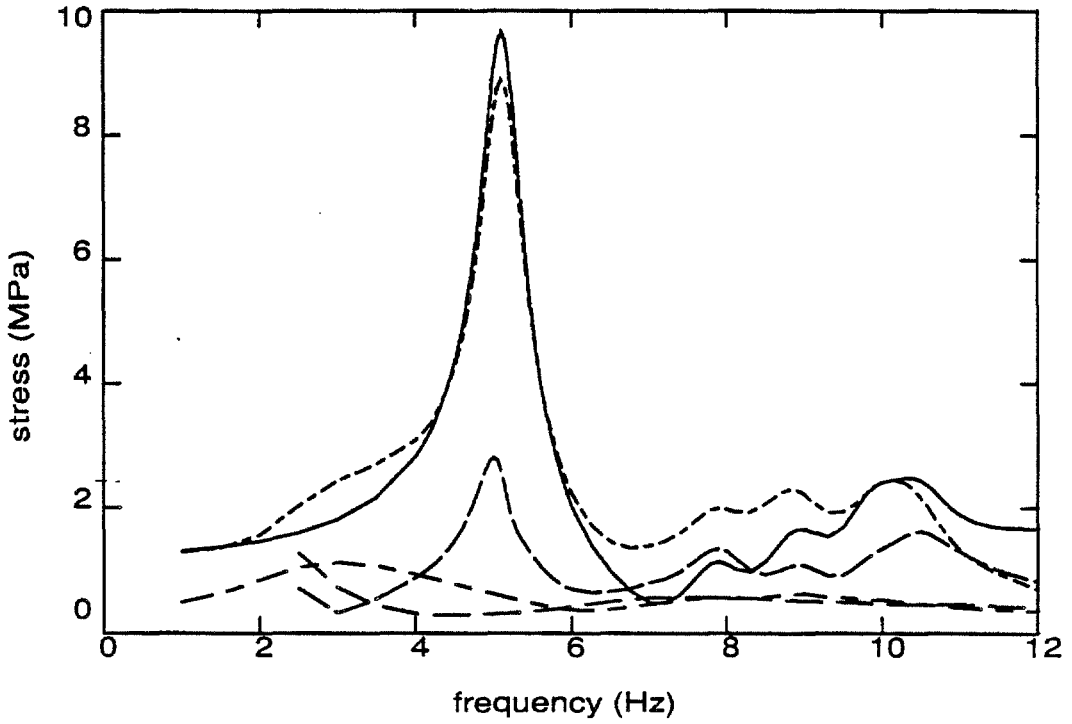

Figure 4.9j : Upstream cantilever stress in element E

Figure 4.10 : **Frequency domain responses of Pacoima dam for excitations in the stream direction, with water. Excitation amplitudes from Table 2.1 times 1g.**

Figure 4.10a : Radial acceleration at node W

Figure 4.10b : Radial acceleration at node X

Figure 4.10c : Stream acceleration at node Y

Figure 4.10d : Stream acceleration at node Z

Figure 4.10e : Upstream arch stress in element A

Figure 4.10f : Downstream arch stress in element B

Figure 4.10g : Downstream arch stress in element E

Figure 4.10h : Downstream cantilever stress in element C

Figure 4.10i : Upstream cantilever stress in element D

Figure 4.10j : Upstream cantilever stress in element E

Key to graphs :

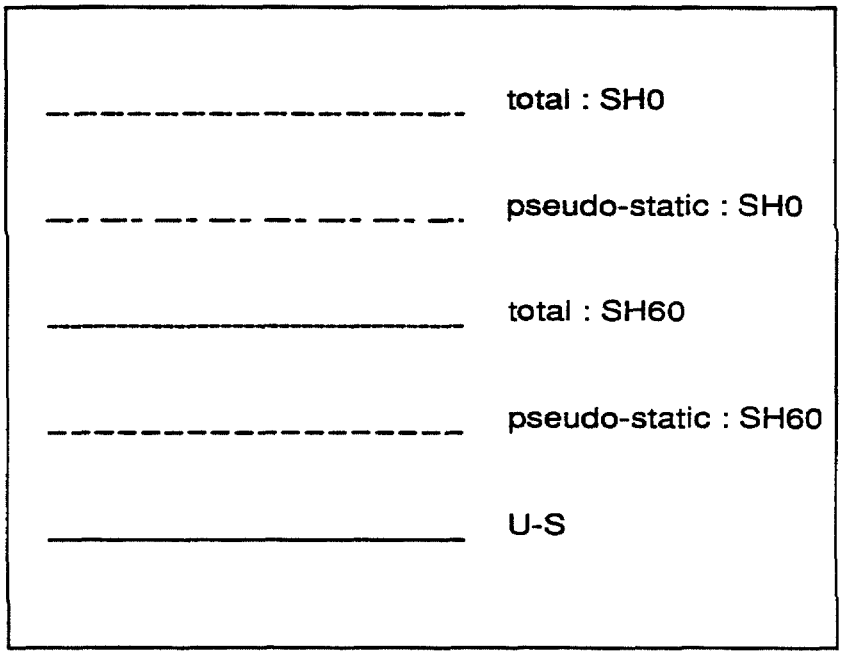

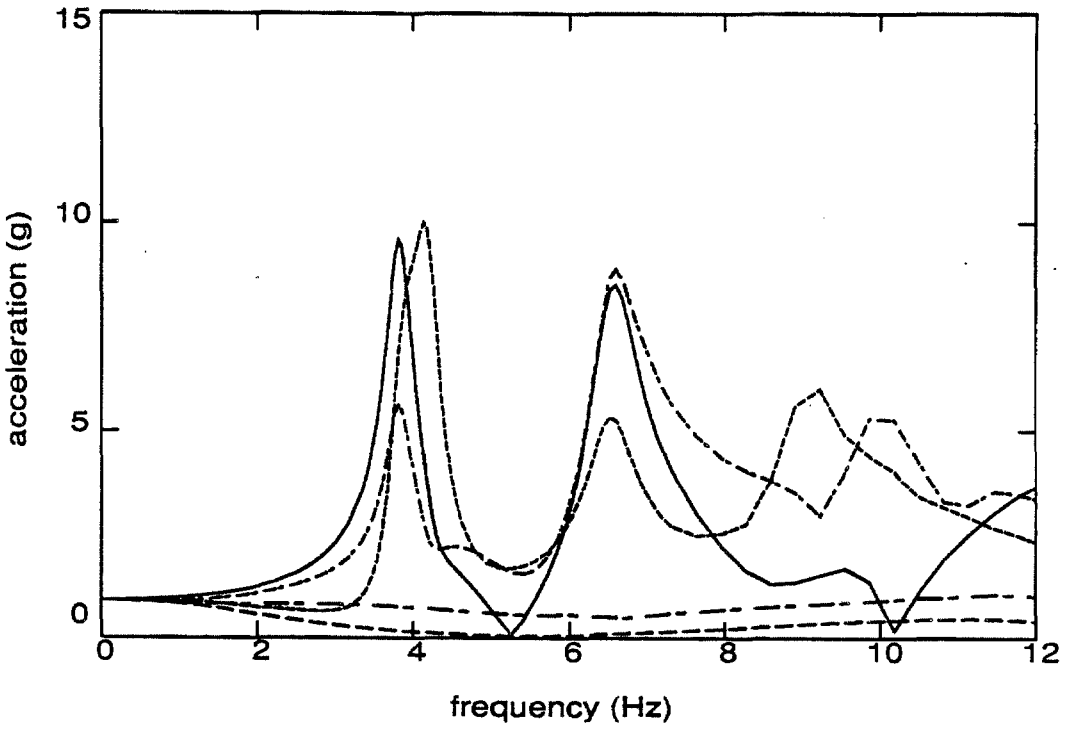

Figure 4.10a : Radial acceleration at node W

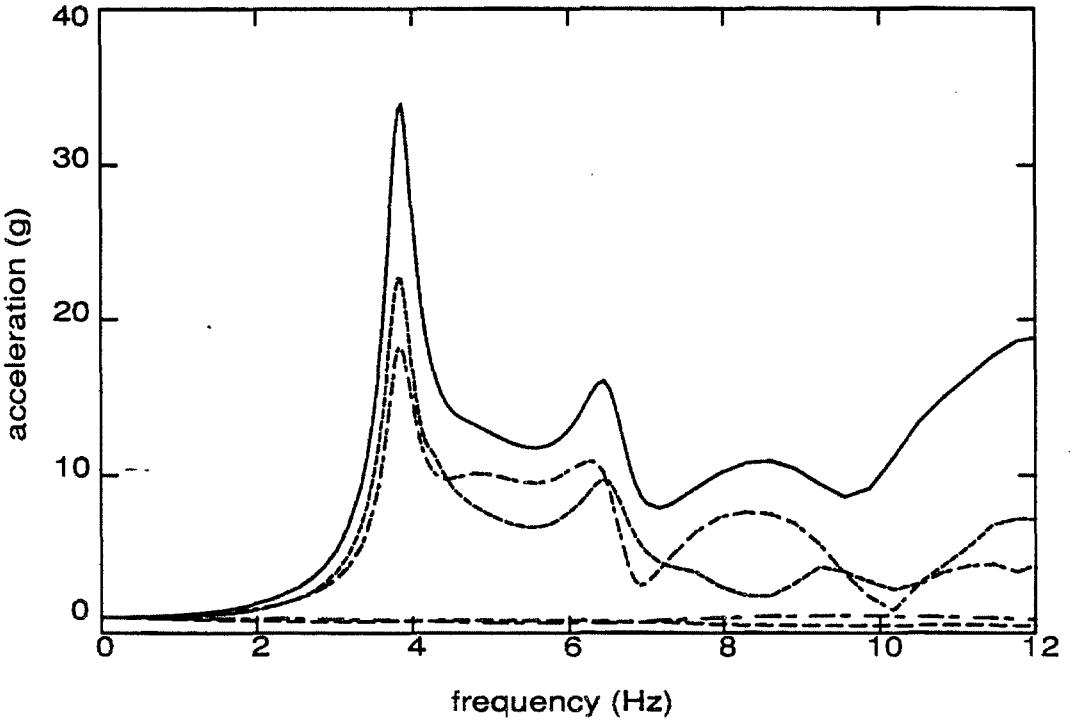

Figure 4.10b : Radial acceleration at node X

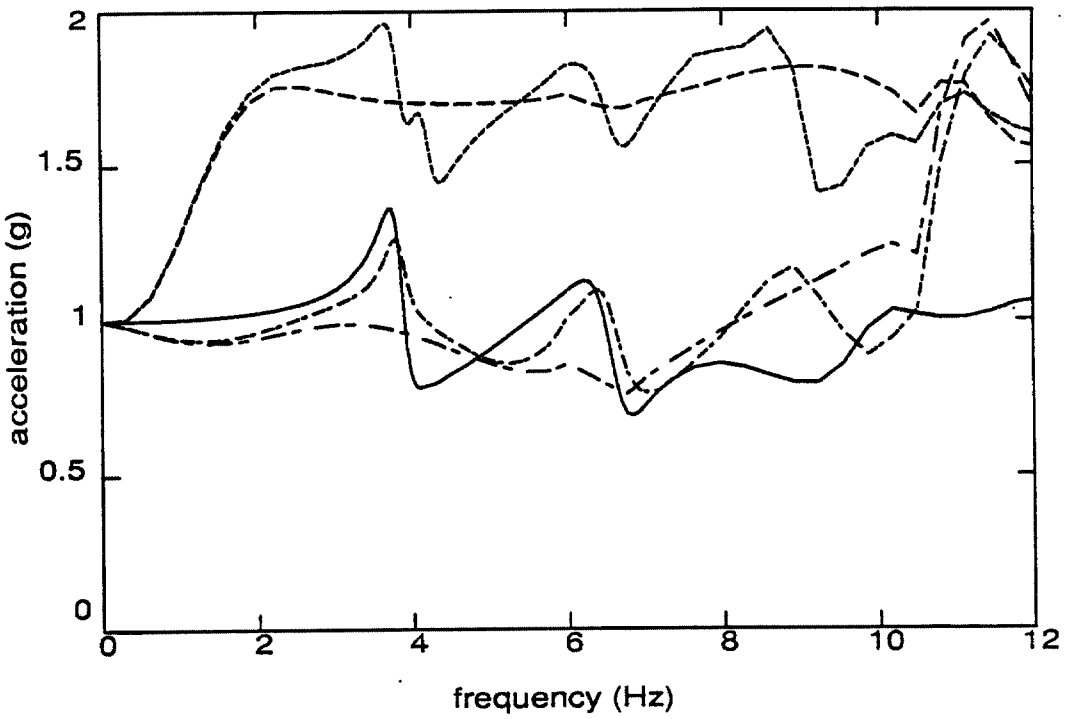

Figure 4.10c : Stream acceleration at node Y

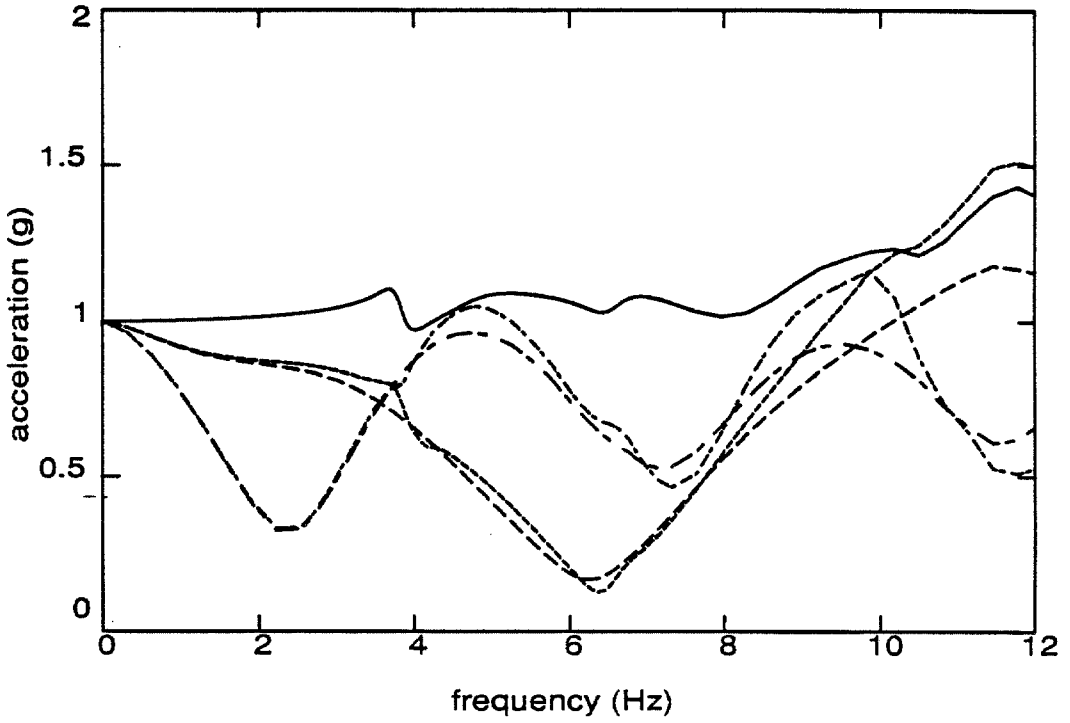

Figure 4.10d : Stream acceleration at node Z

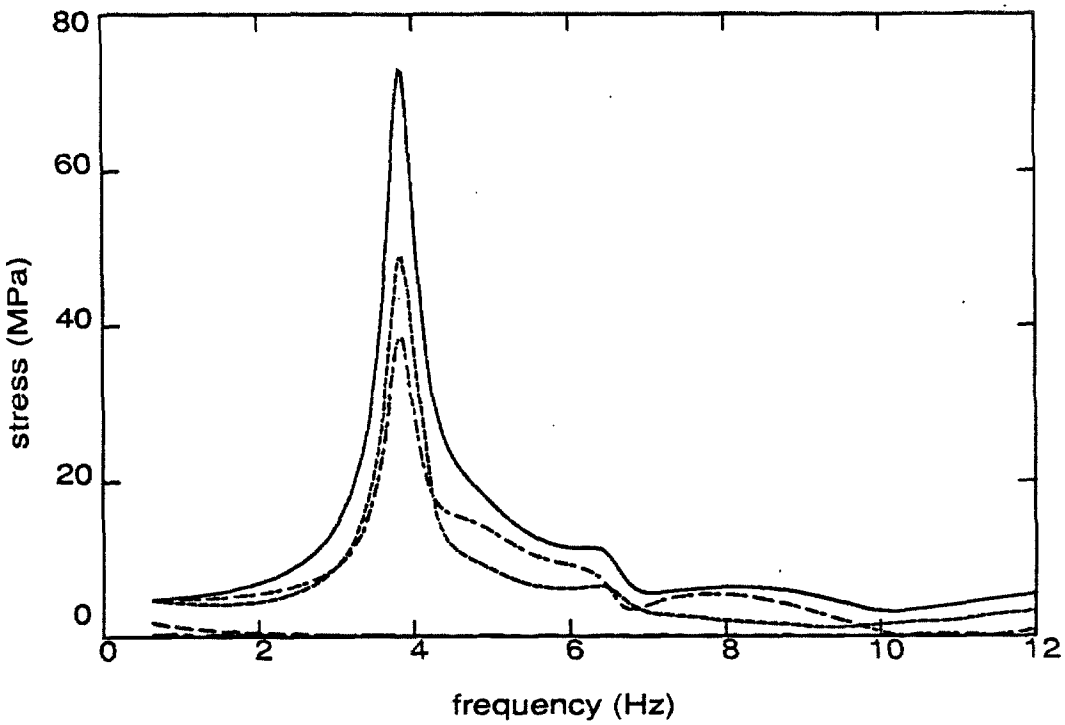

Figure 4.10e : Upstream arch stress in element A

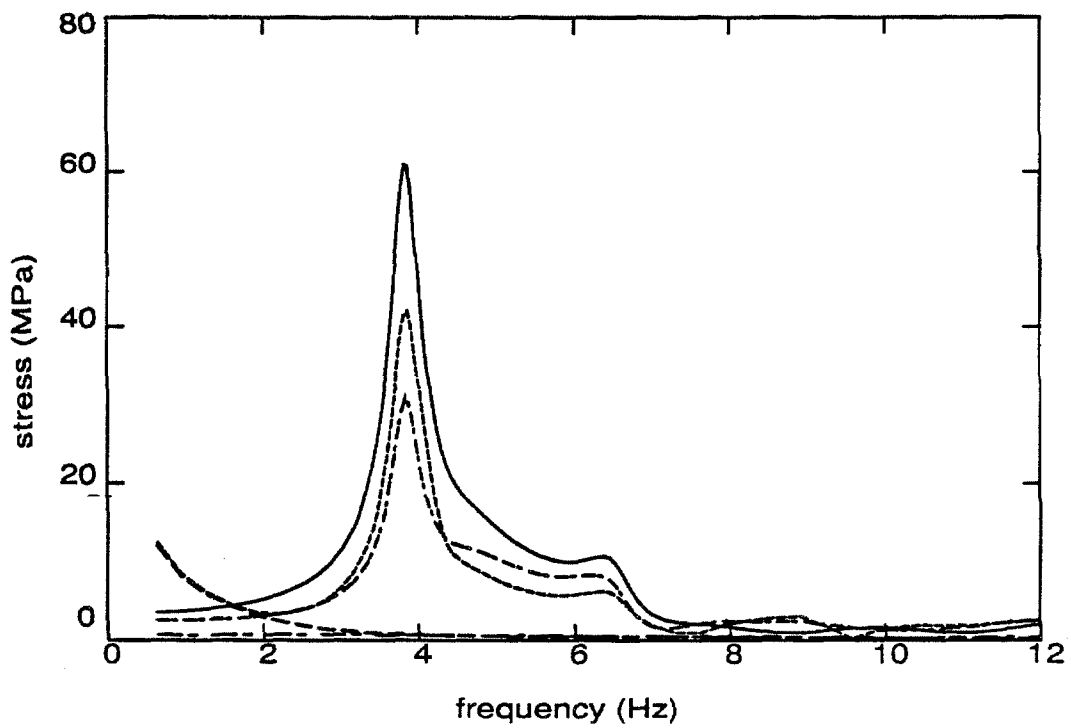

Figure 4.10f : Downstream arch stress in element B

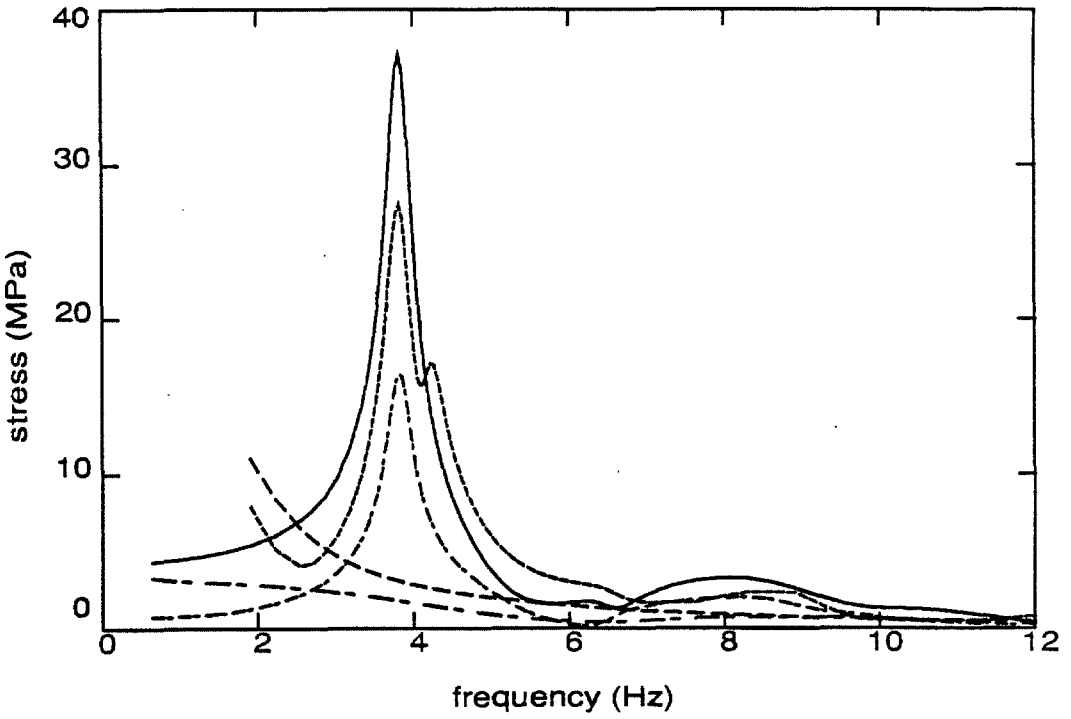

Figure 4.10g : Downstream arch stress in element E

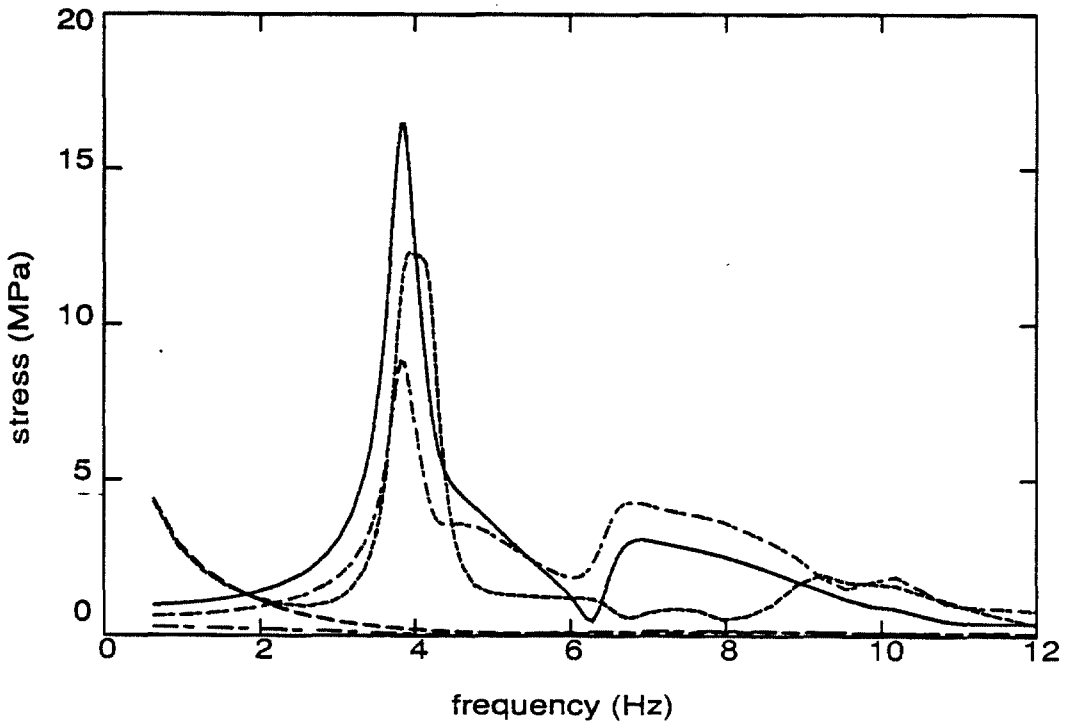

Figure 4.10h : Downstream cantilever stress in element C

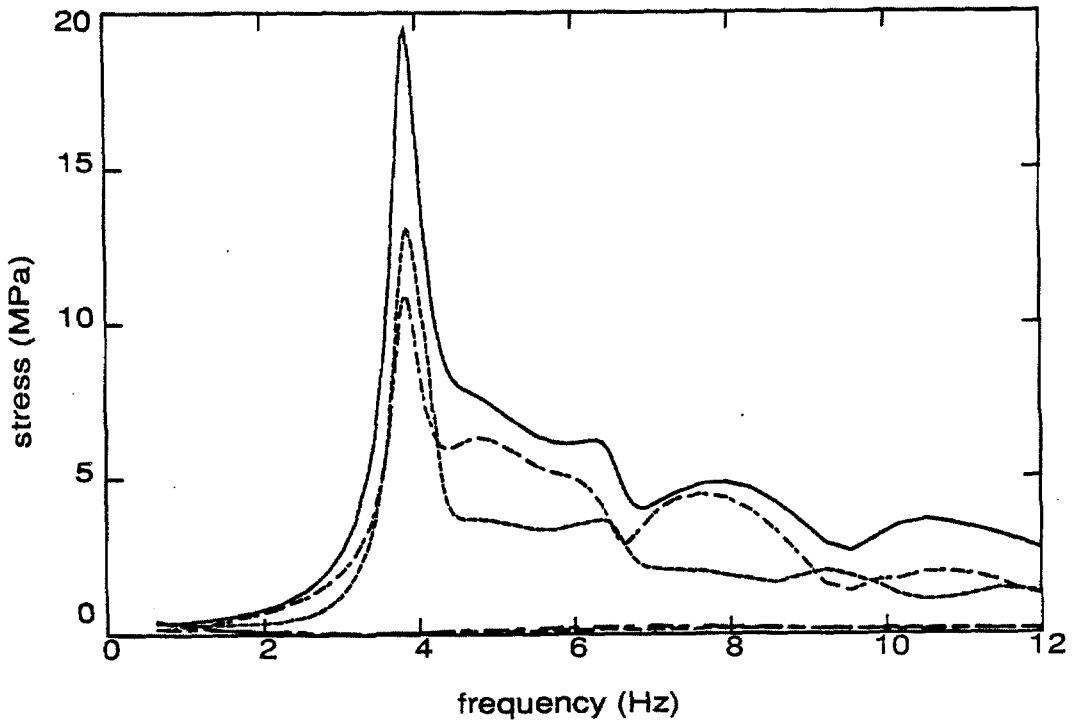

Figure 4.10i : Upstream cantilever stress in element D

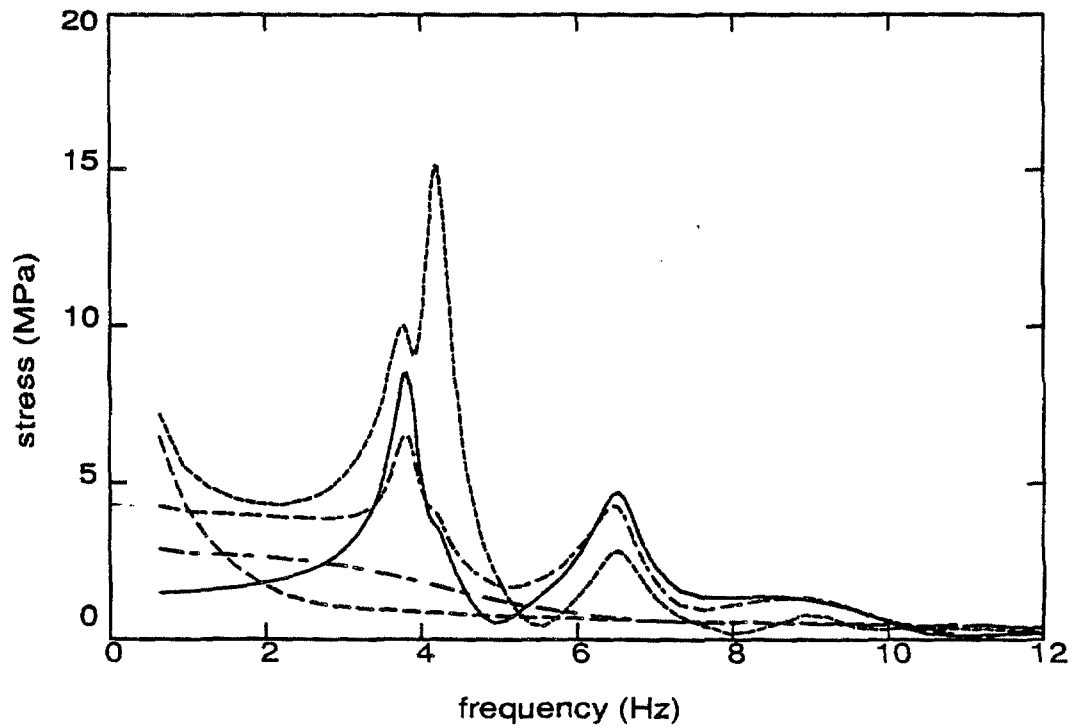

Figure 4.10j : Upstream cantilever stress in element E

Figure 4.11: Frequency domain responses of Pacoima dam for excitations in the cross-stream and vertical direction, with water. Excitation amplitudes from Table 2.1 times 1g.

Figure 4.11a: Radial acceleration at node W

Figure 4.11b: Radial acceleration at node X

Figure 4.11c: Stream acceleration at node Y

Figure 4.11d: Stream acceleration at node Z

Figure 4.11e: Upstream arch stress in element A

Figure 4.11f: Downstream arch stress in element B

Figure 4.11g: Downstream arch stress in element E

Figure 4.11h: Downstream cantilever stress in element C

Figure 4.11i: Upstream cantilever stress in element D

Figure 4.11j: Upstream cantilever stress in element E

Key to graphs :

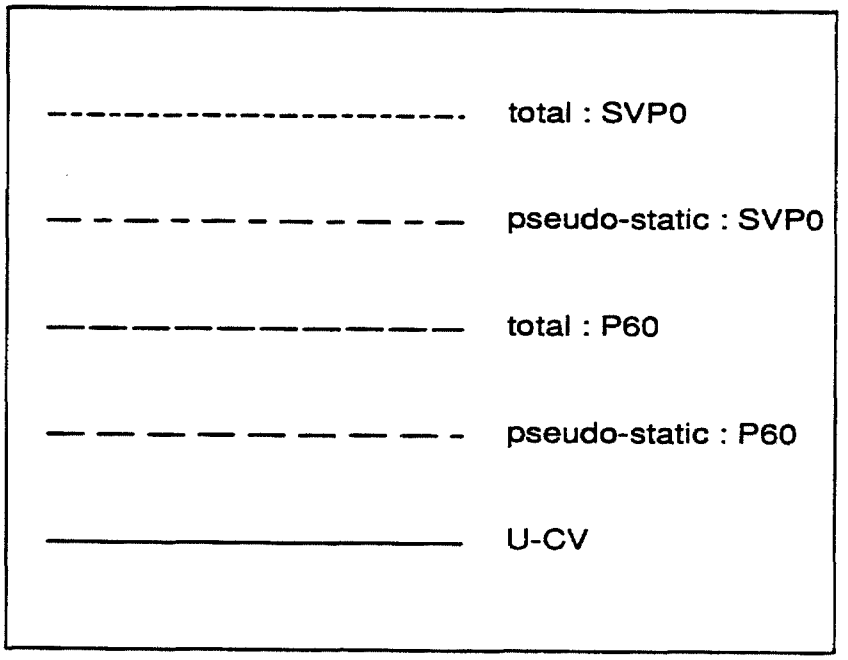

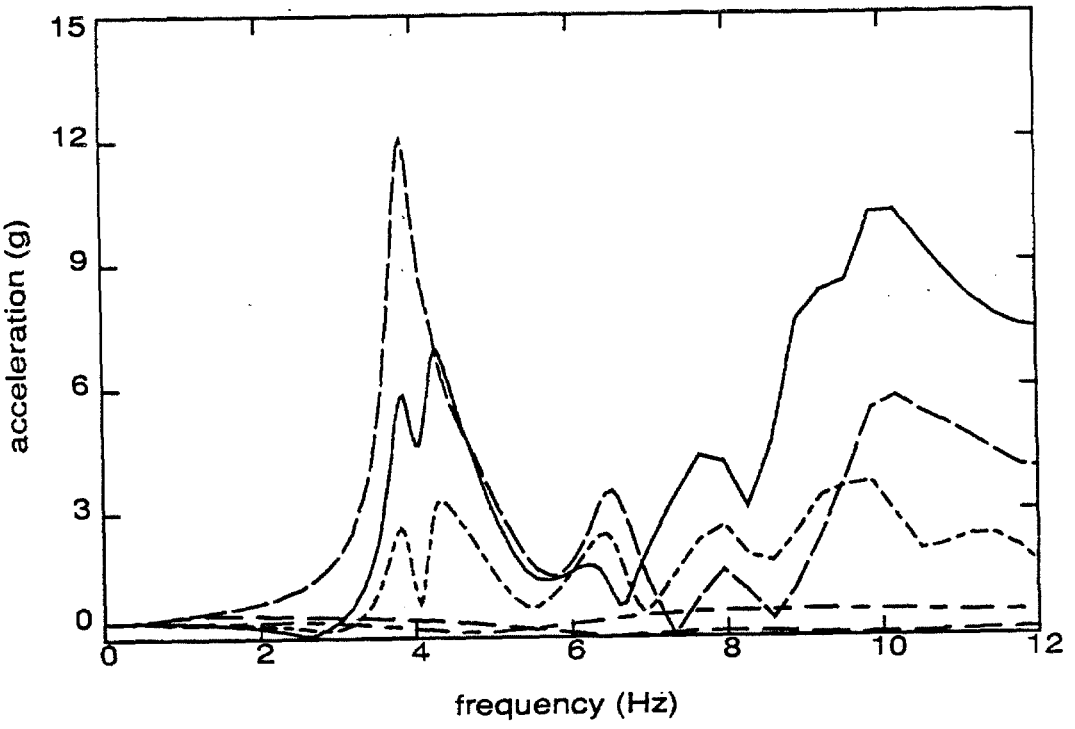

Figure 4.11a : Radial acceleration at node W

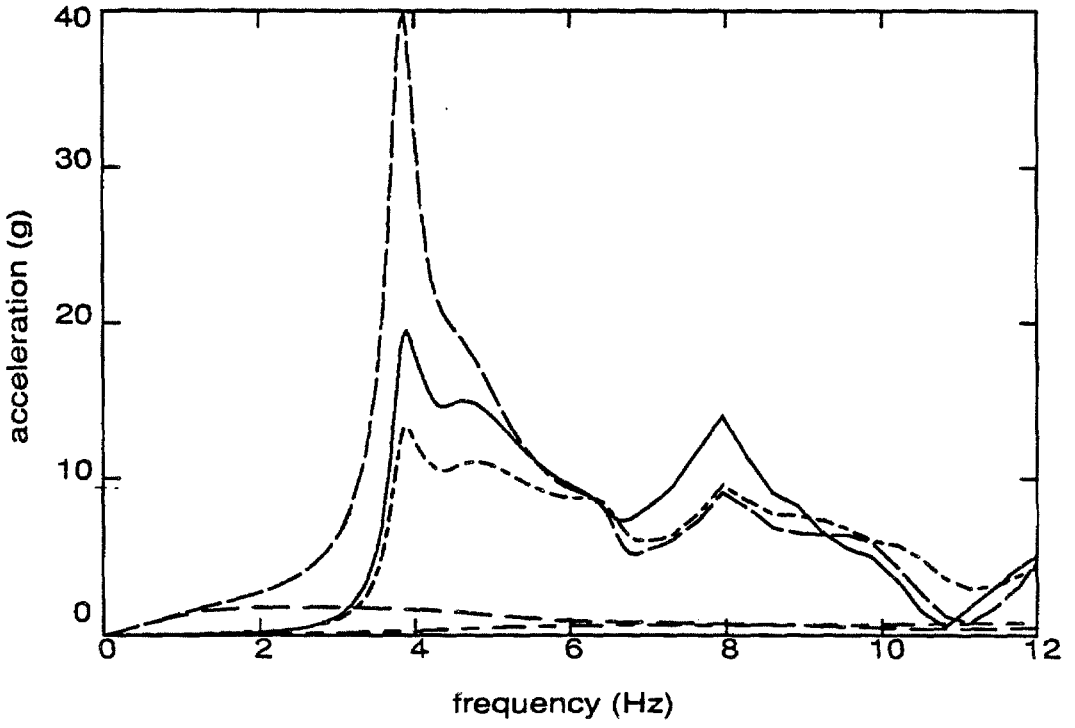

Figure 4.11b : Radial acceleration at node X

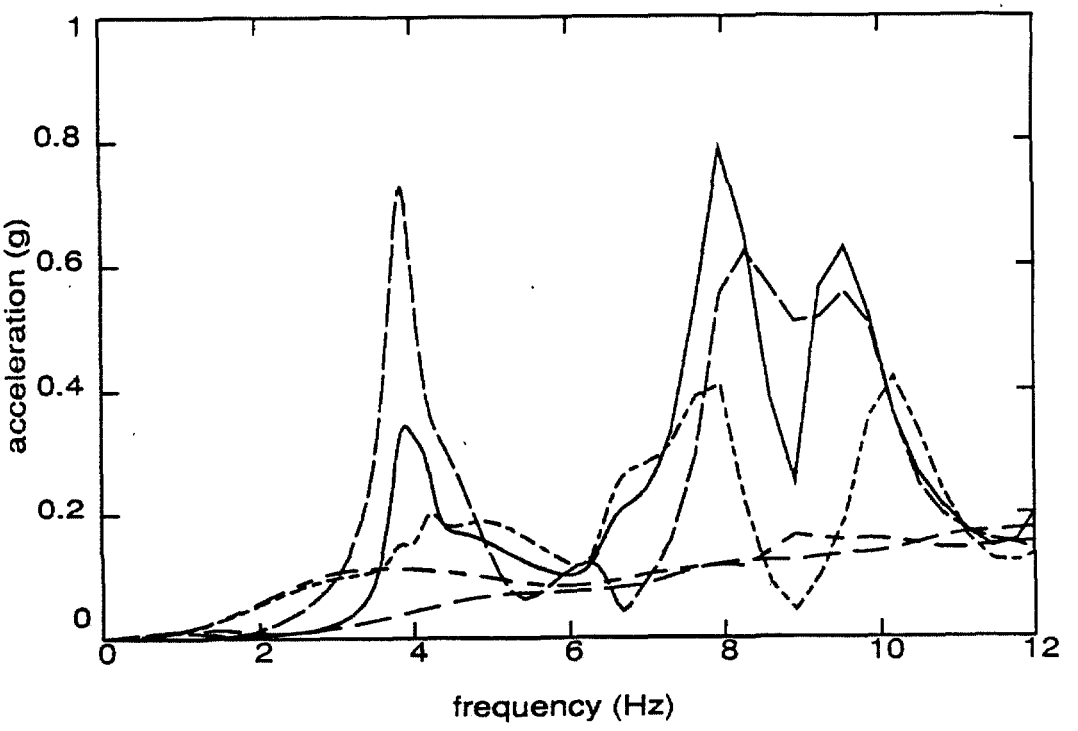

Figure 4.11c : Stream acceleration at node Y

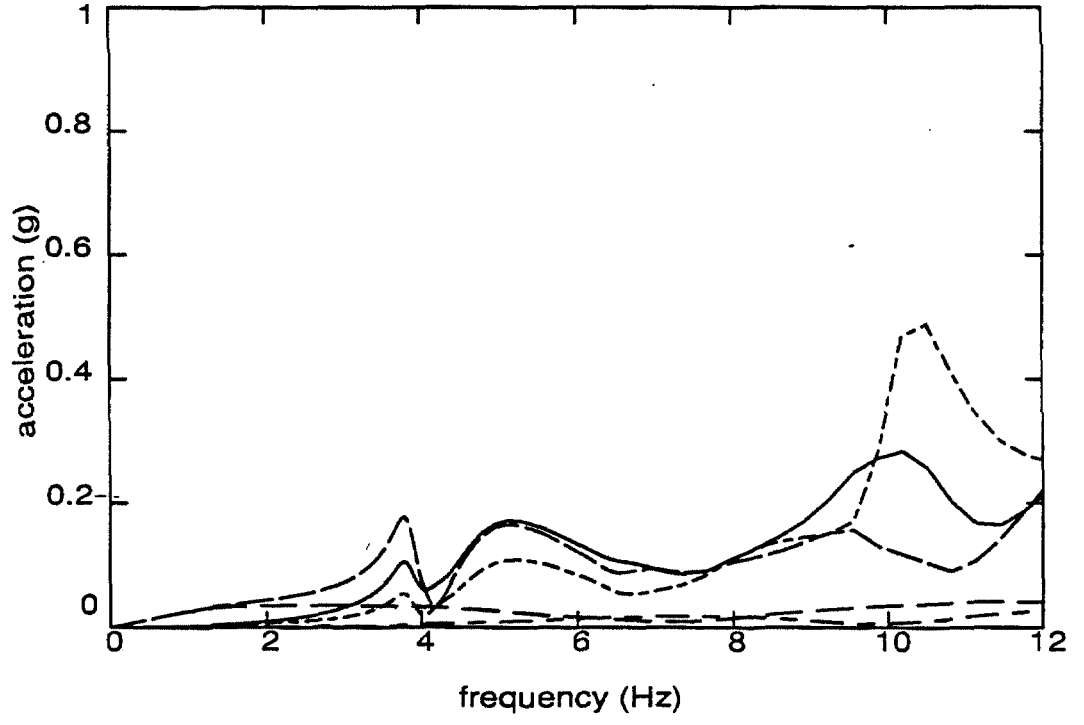

Figure 4.11d : Stream acceleration at node Z

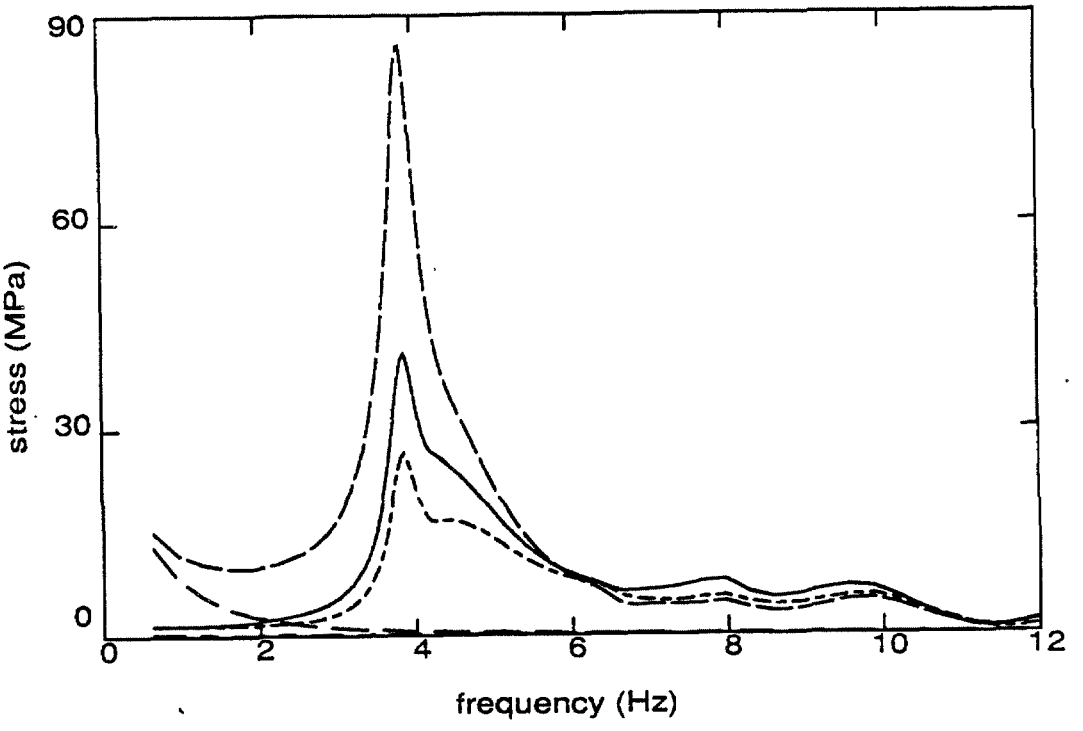

Figure 4.11e : Upstream arch stress in element A

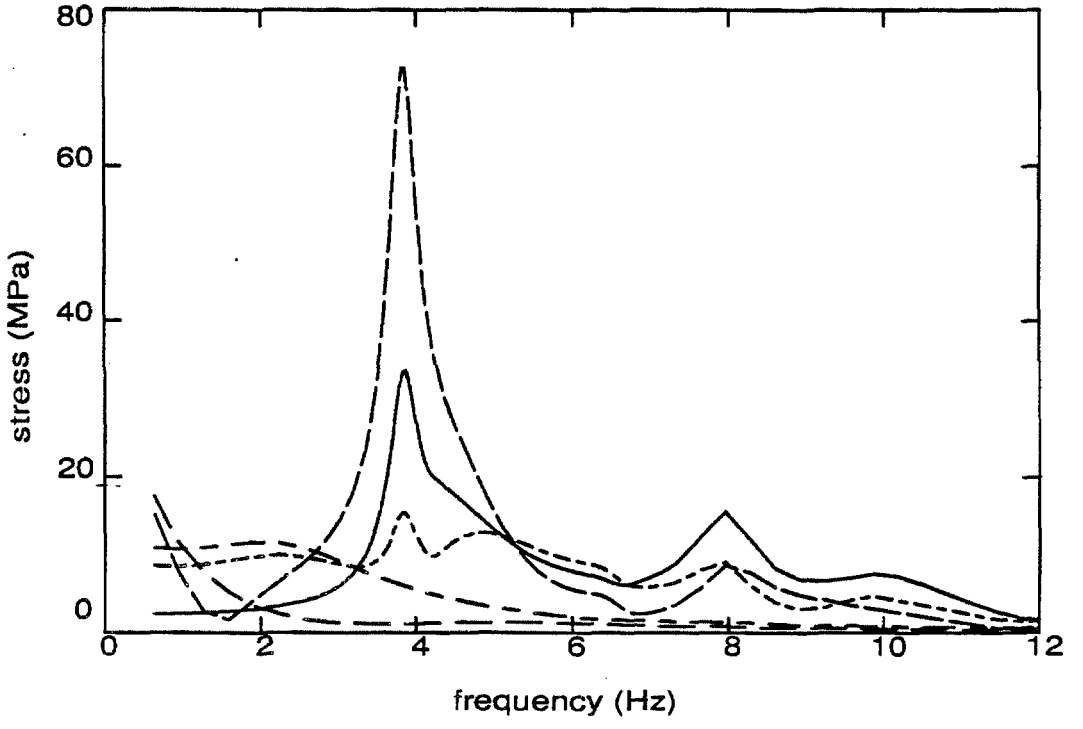

Figure 4.11f : Downstream arch stress in element B

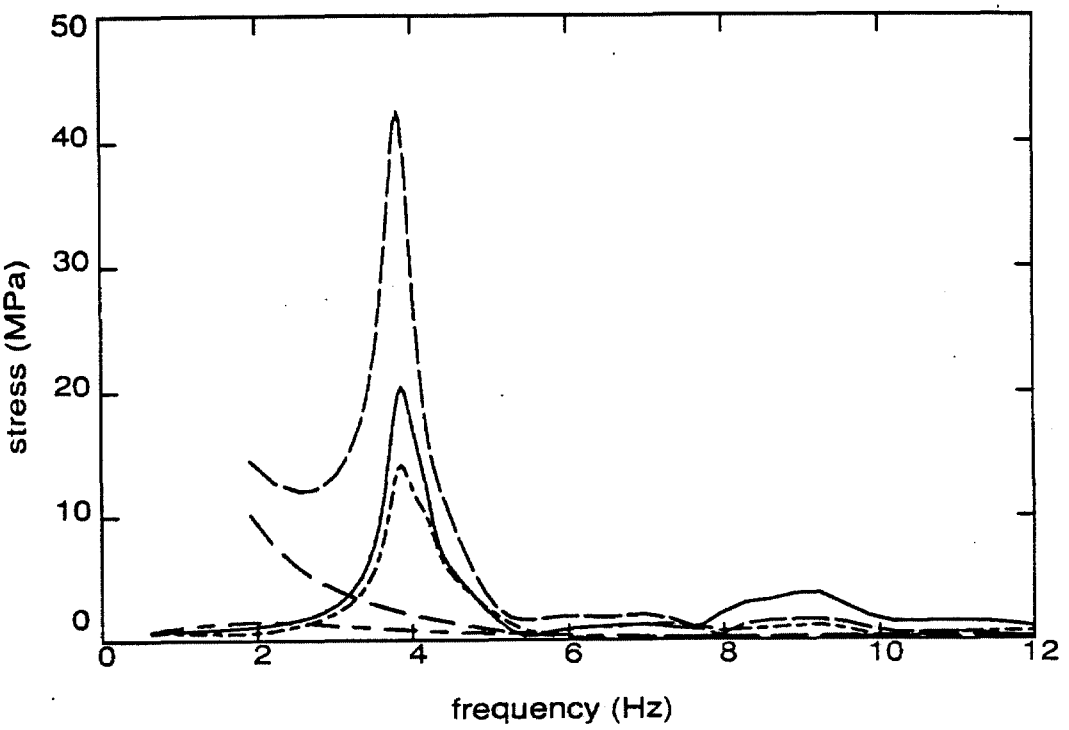

Figure 4.11g : Downstream arch stress in element E

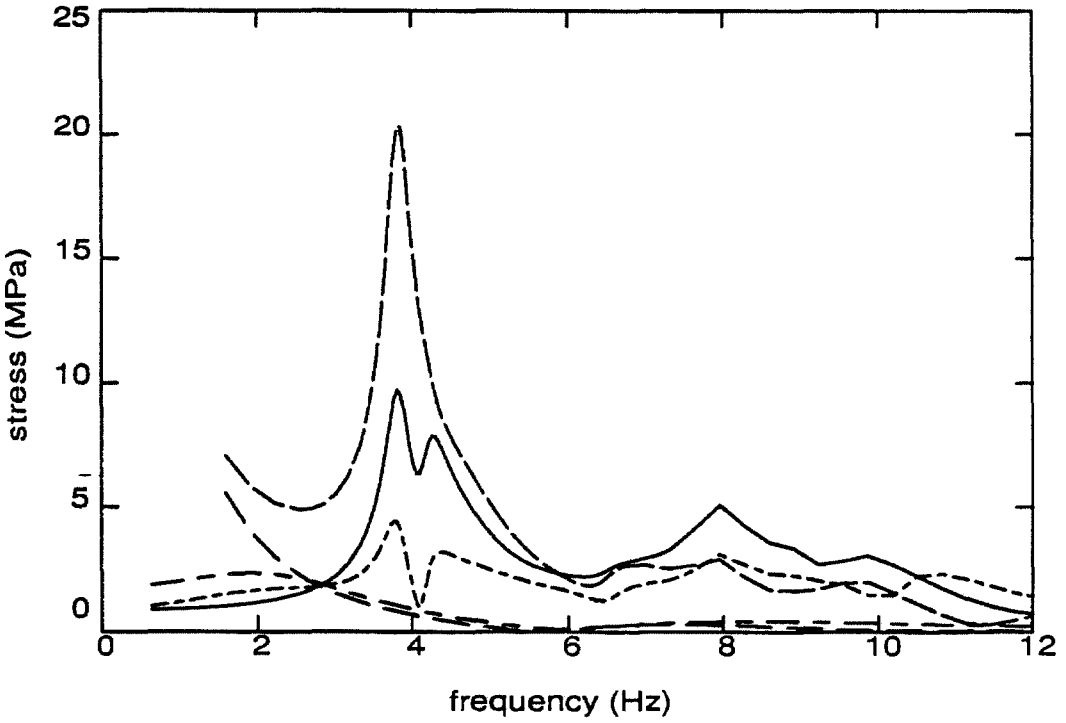

Figure 4.11h : Downstream cantilever stress in element C

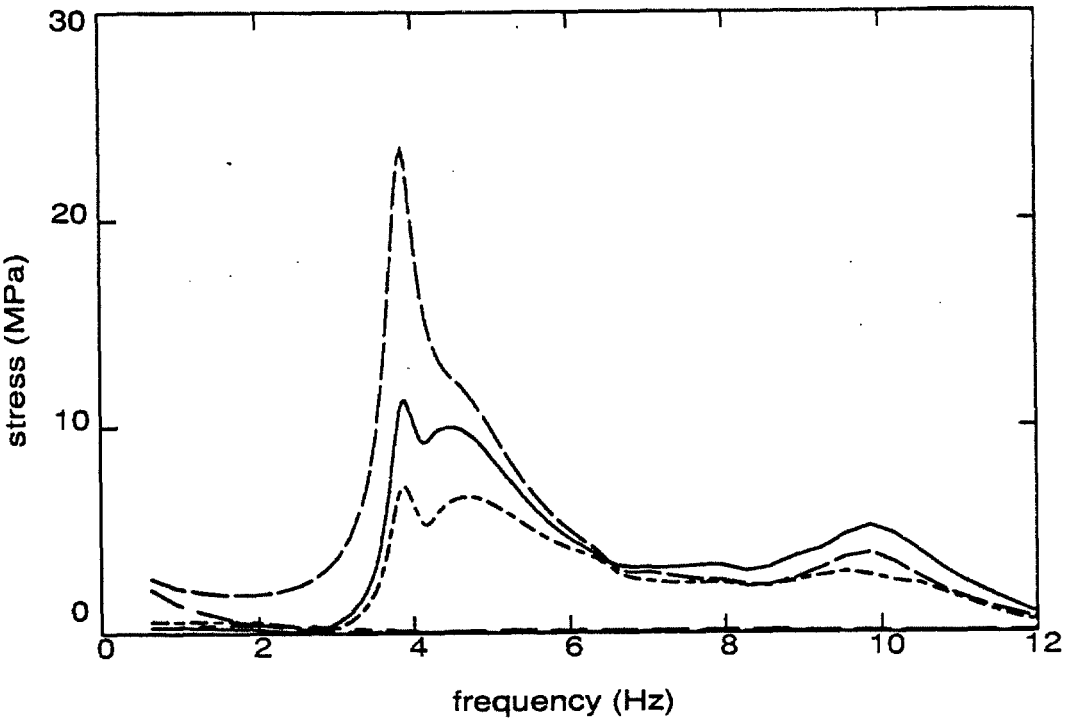

Figure 4.11i : Upstream cantilever stress in element D

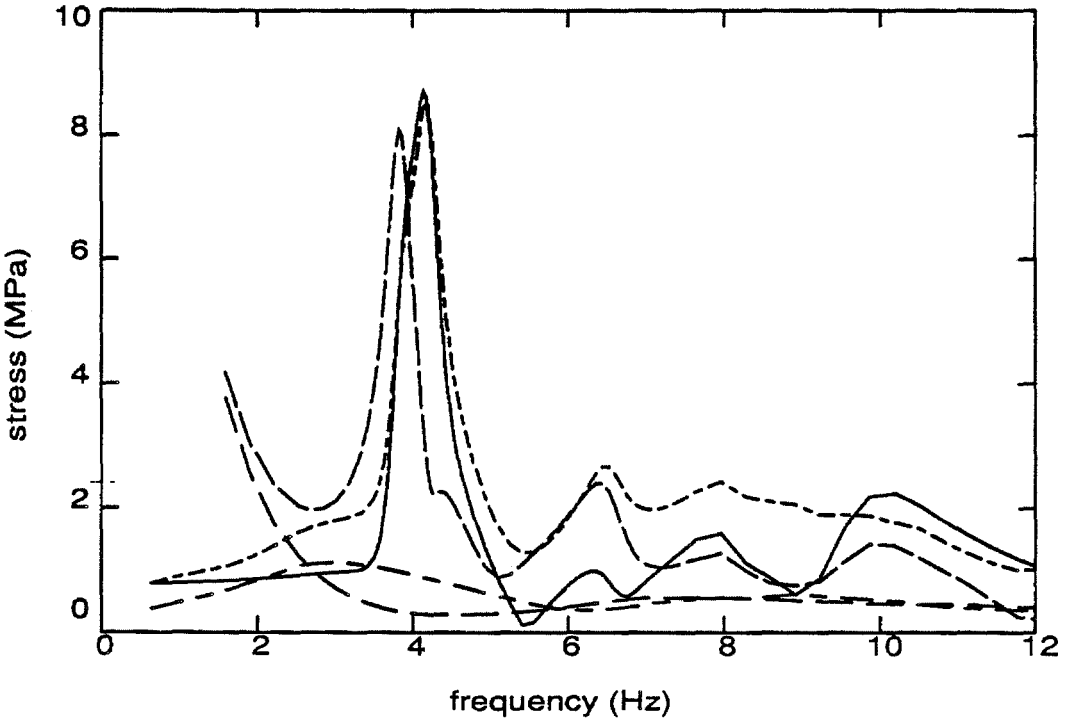

Figure 4.11j : Upstream cantilever stress in element E

Figure 4.12 : Contours of the standard deviations over time of the stresses in Pacoima dam without water for an M = 7.5 earthquake normalized with the arch stress at the center crest for excitation U-S with water (=100). Contours are given for : total arch stress, total cantilever stress, pseudo-static (p-s) arch stress and pseudo-static (p-s) cantilever stress.

Figure 4.12a : Excitation U-S

Figure 4.12b : Excitation SH0

Figure 4.12c : Excitation SH60

Figure 4.12d : Excitation U-CV

Figure 4.12e : Excitation SVP0

Figure 4.12f : Excitation P60

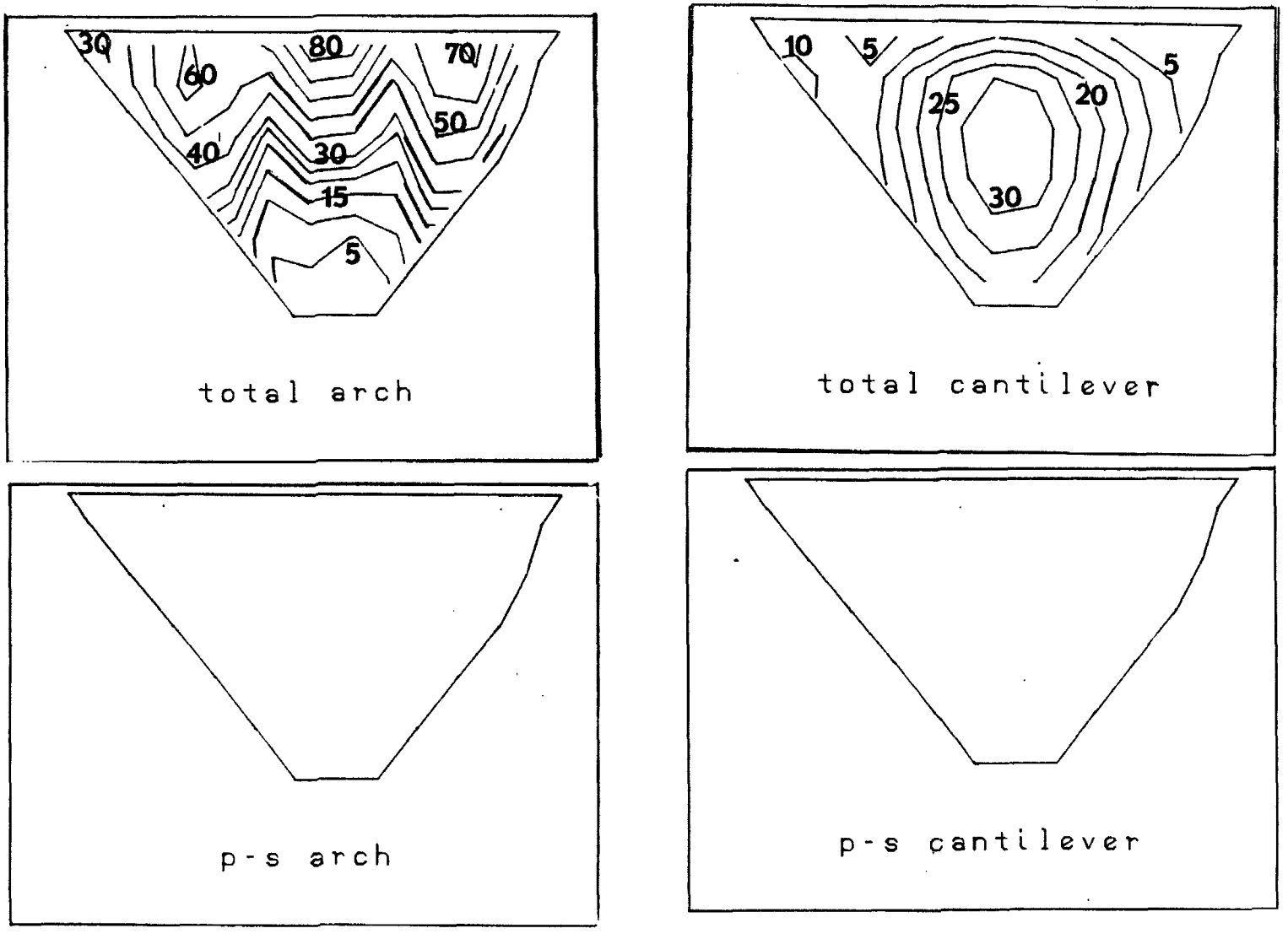

Figure 4.12a : Excitation U-S

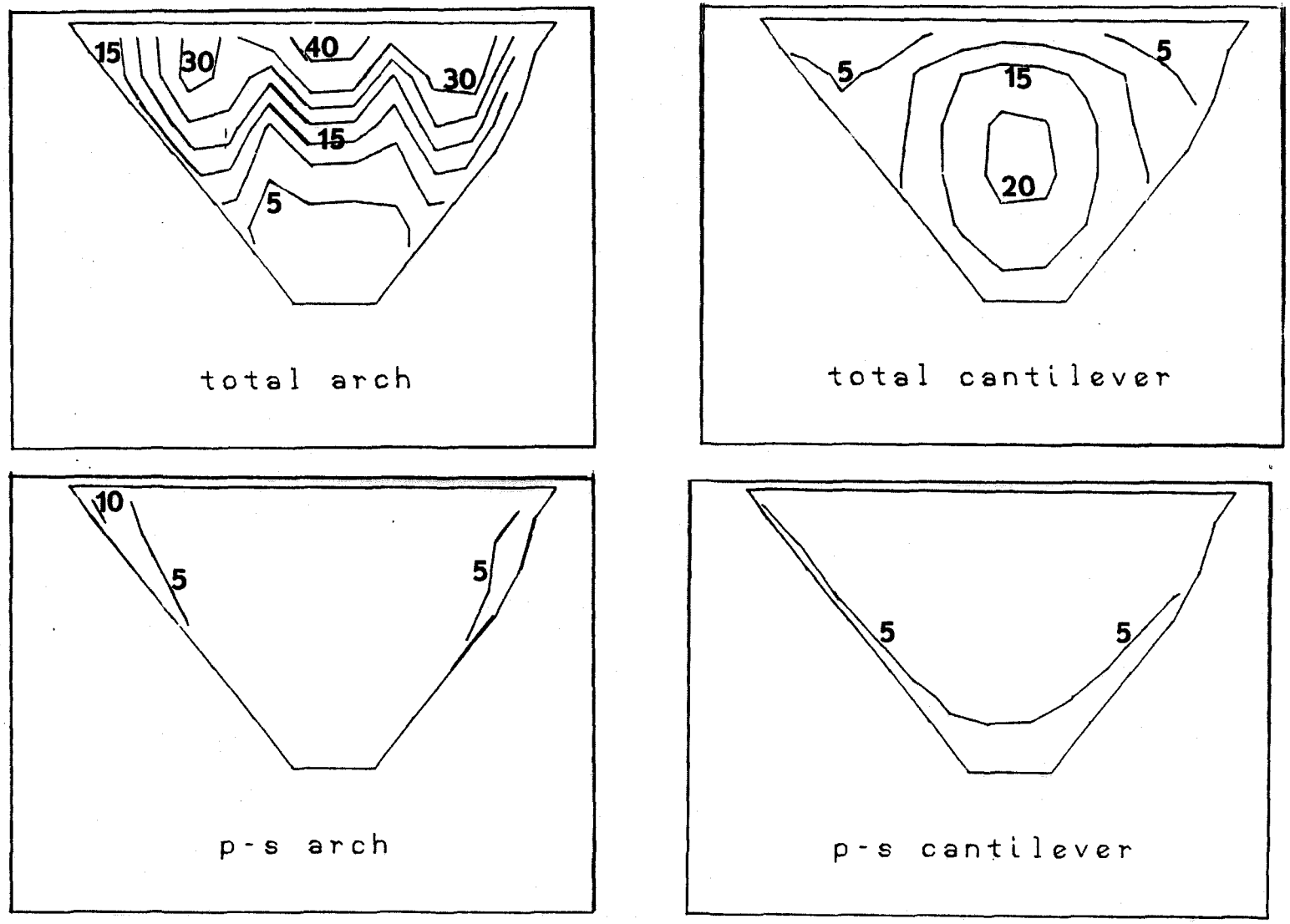

Figure 4.12b : Excitation SH0

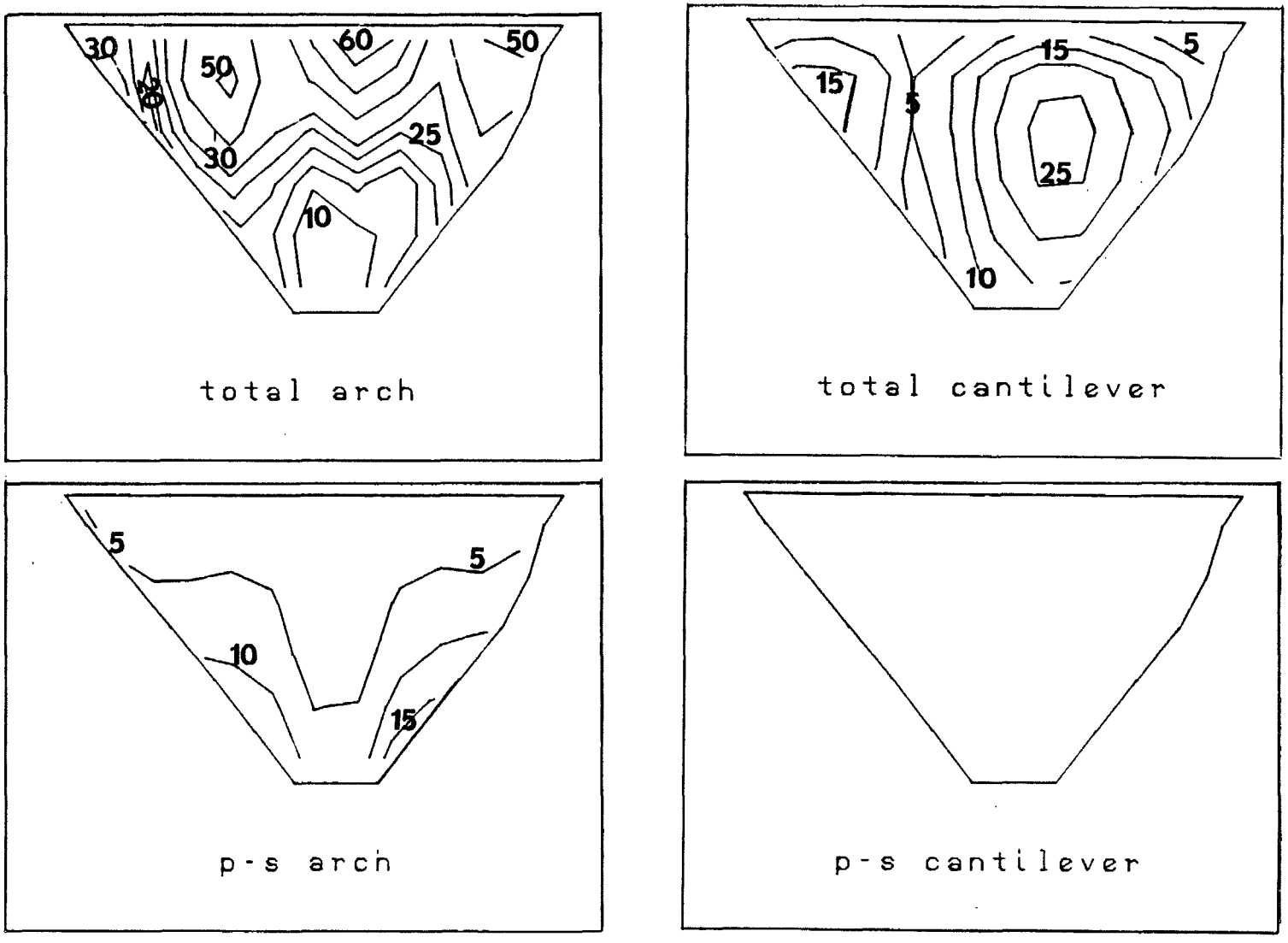

Figure 4.12c : Excitation SH60

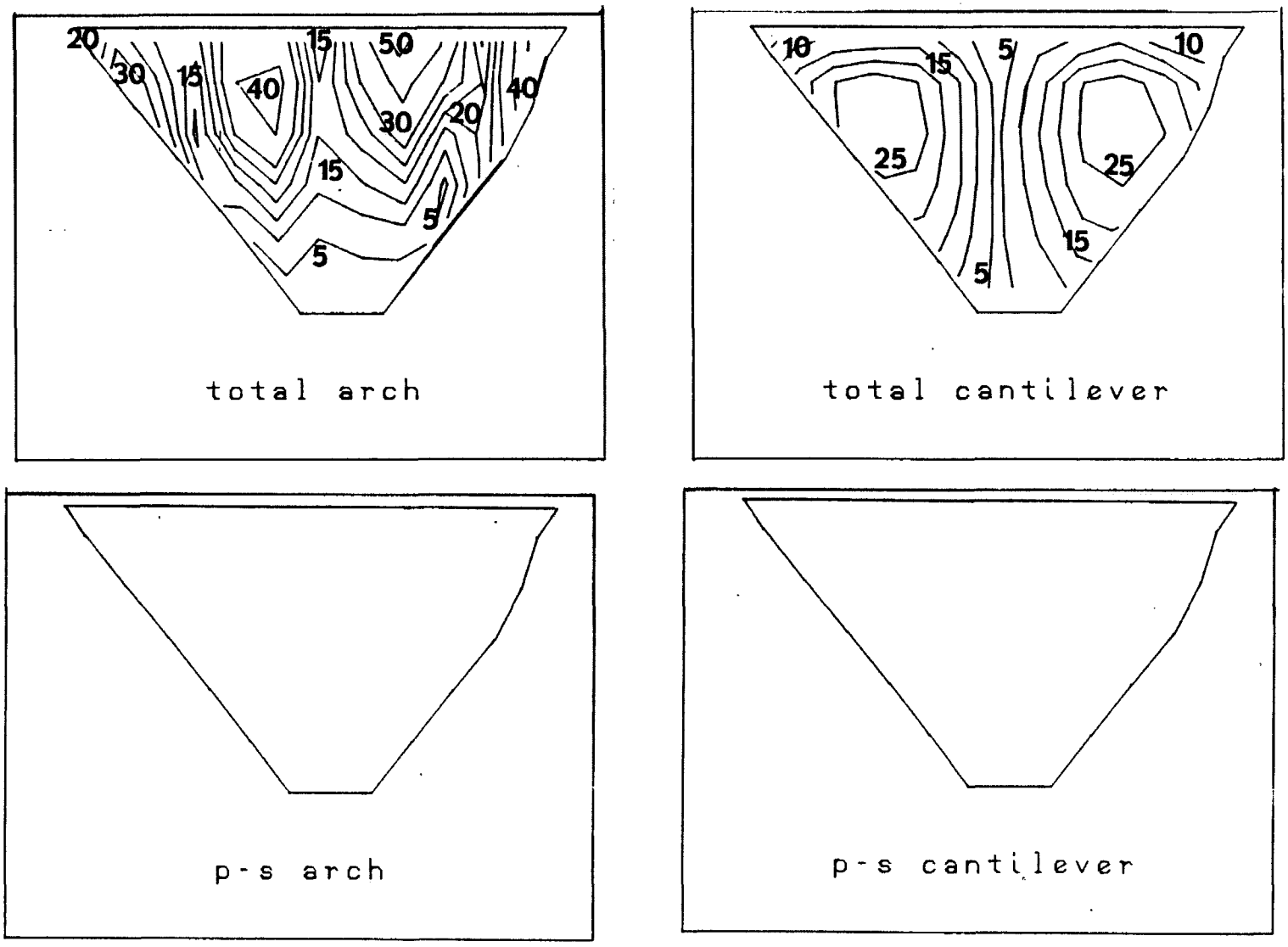

Figure 4.12d : Excitation U-CV

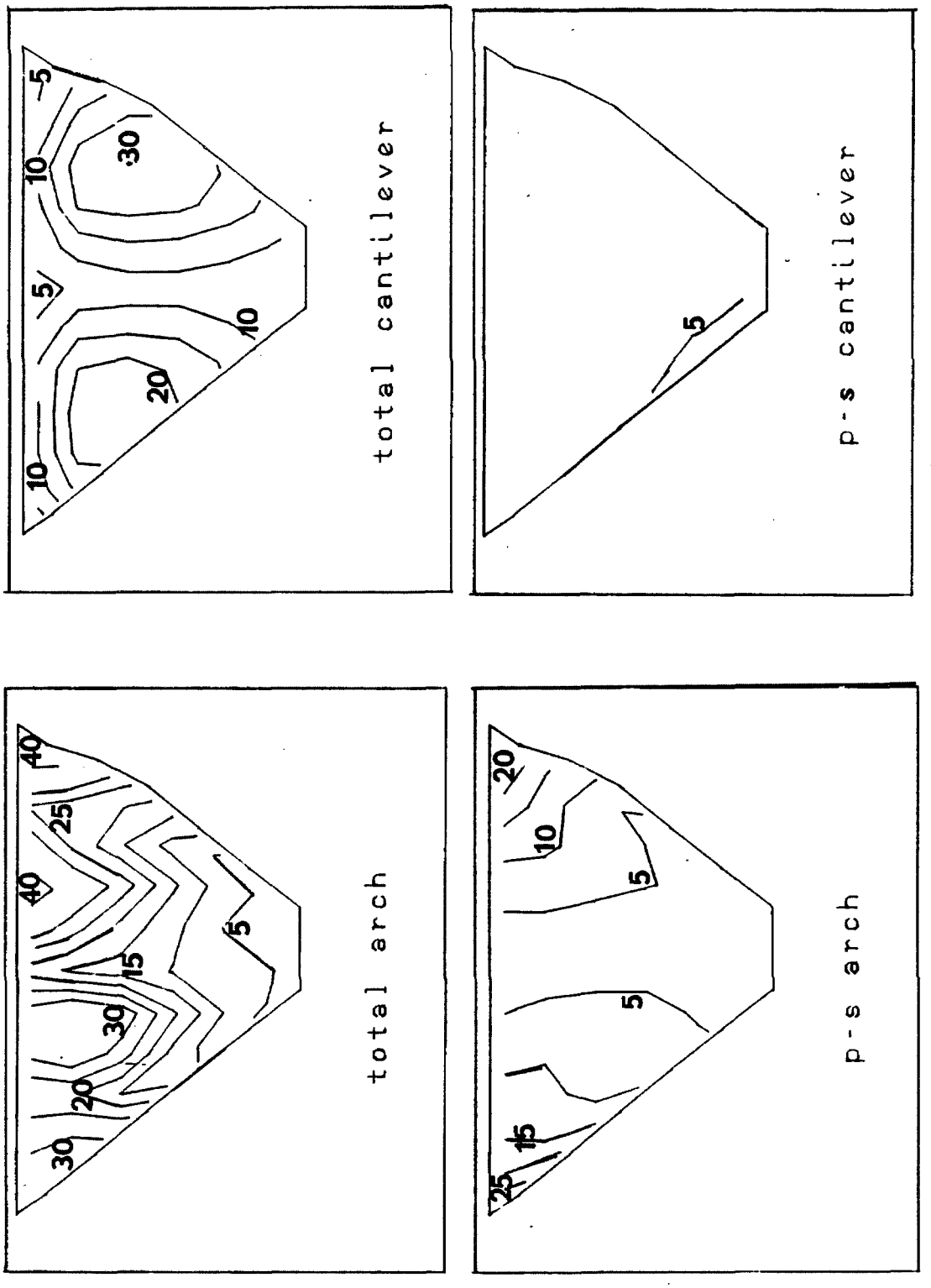

Figure 4.12e : Excitation SVP0

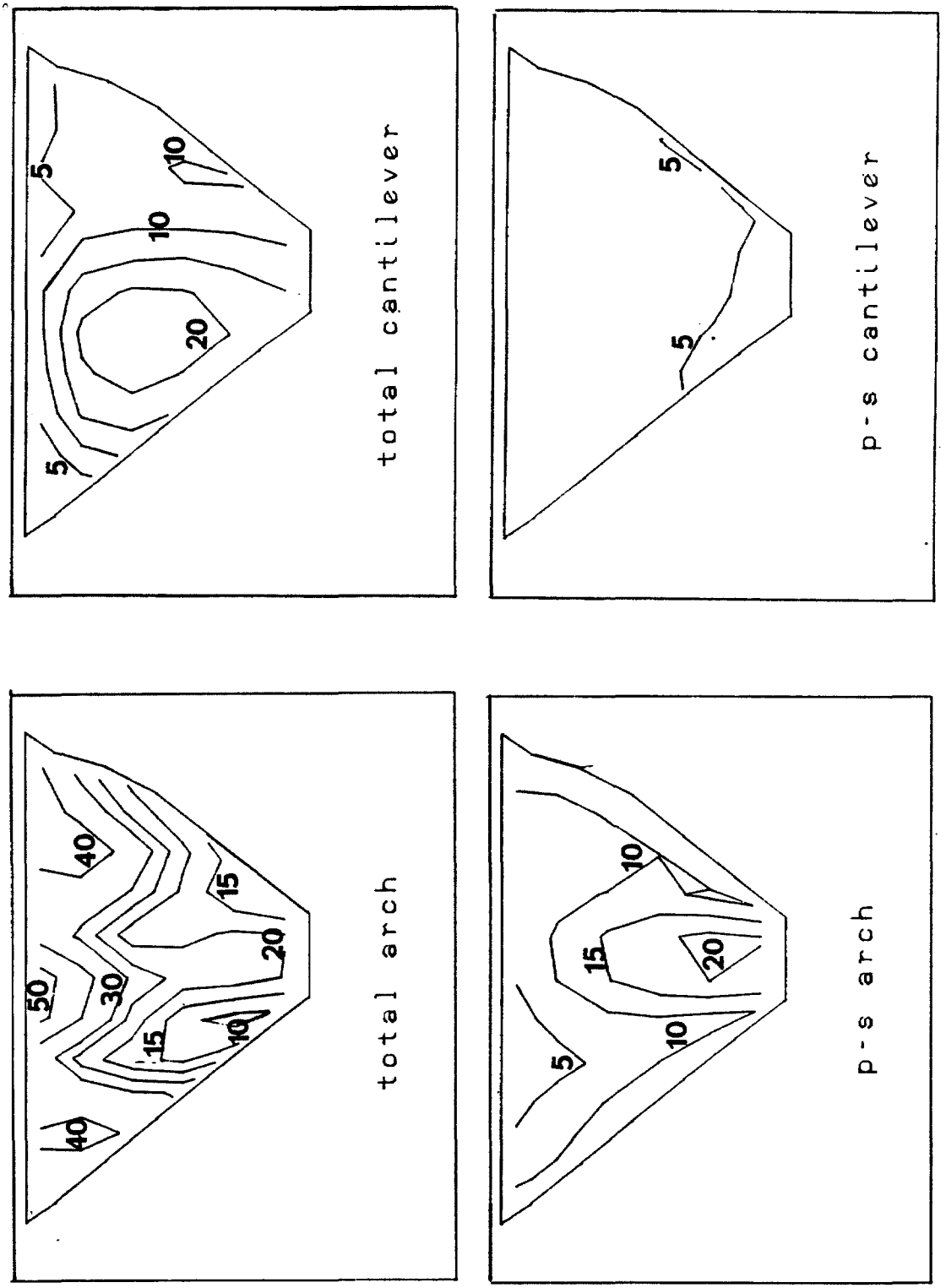

Figure 4.12f : Excitation P60

Figure 4.13 : Contours of the standard deviations over time of the stresses in Pacoima dam with water for an M = 7.5 earthquake normalized with the arch stress at the center crest for excitation U-S with water (=100). Contours are given for : total arch stress, total cantilever stress, pseudo-static (p-s) arch stress and pseudo-static (p-s) cantilever stress.

Figure 4.13a : Excitation U-S

Figure 4.13b : Excitation SH0

Figure 4.13c : Excitation SH60

Figure 4.13d : Excitation U-CV

Figure 4.13e : Excitation SVP0

Figure 4.13f : Excitation P60

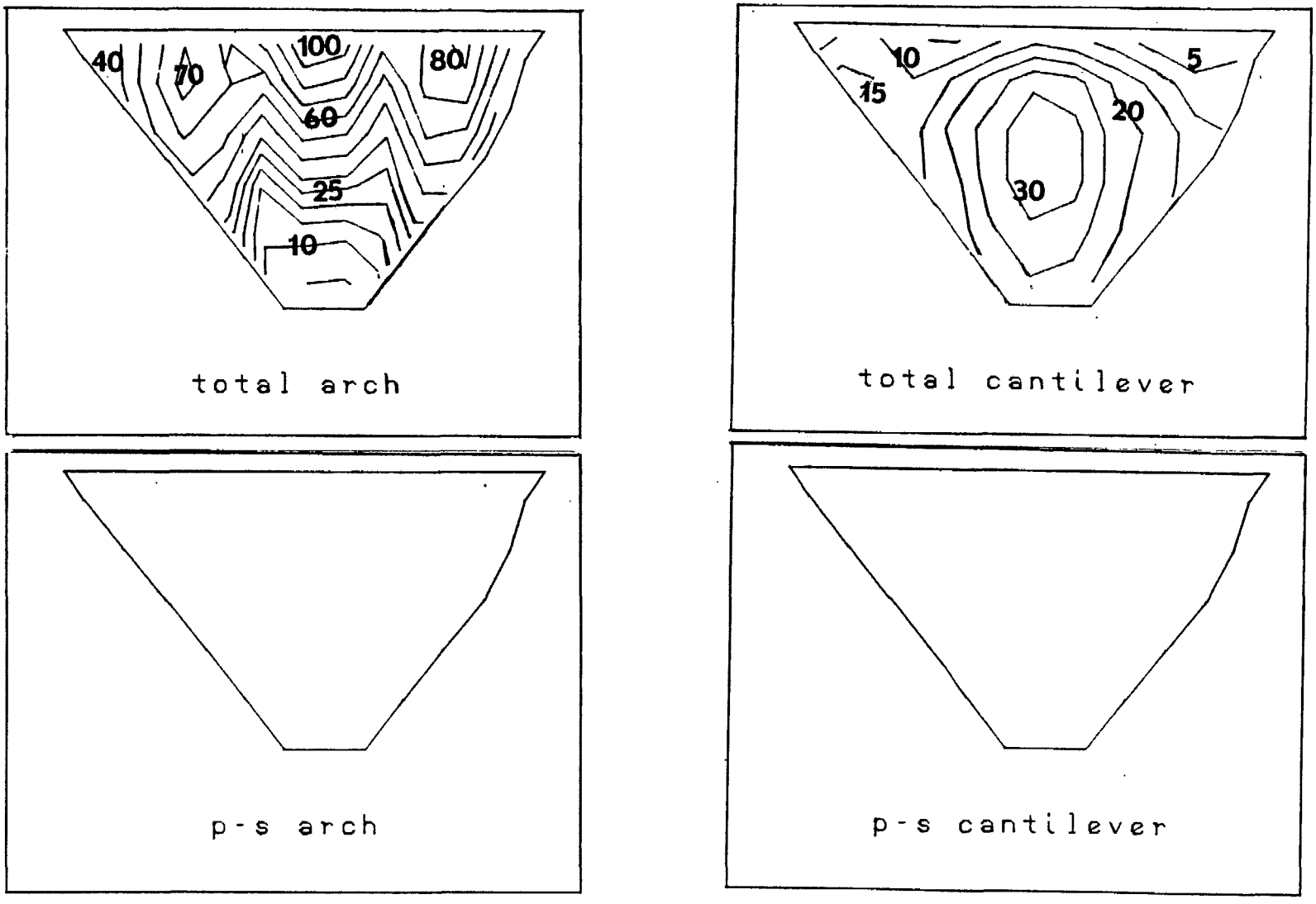

Figure 4.13a : Excitation U-S

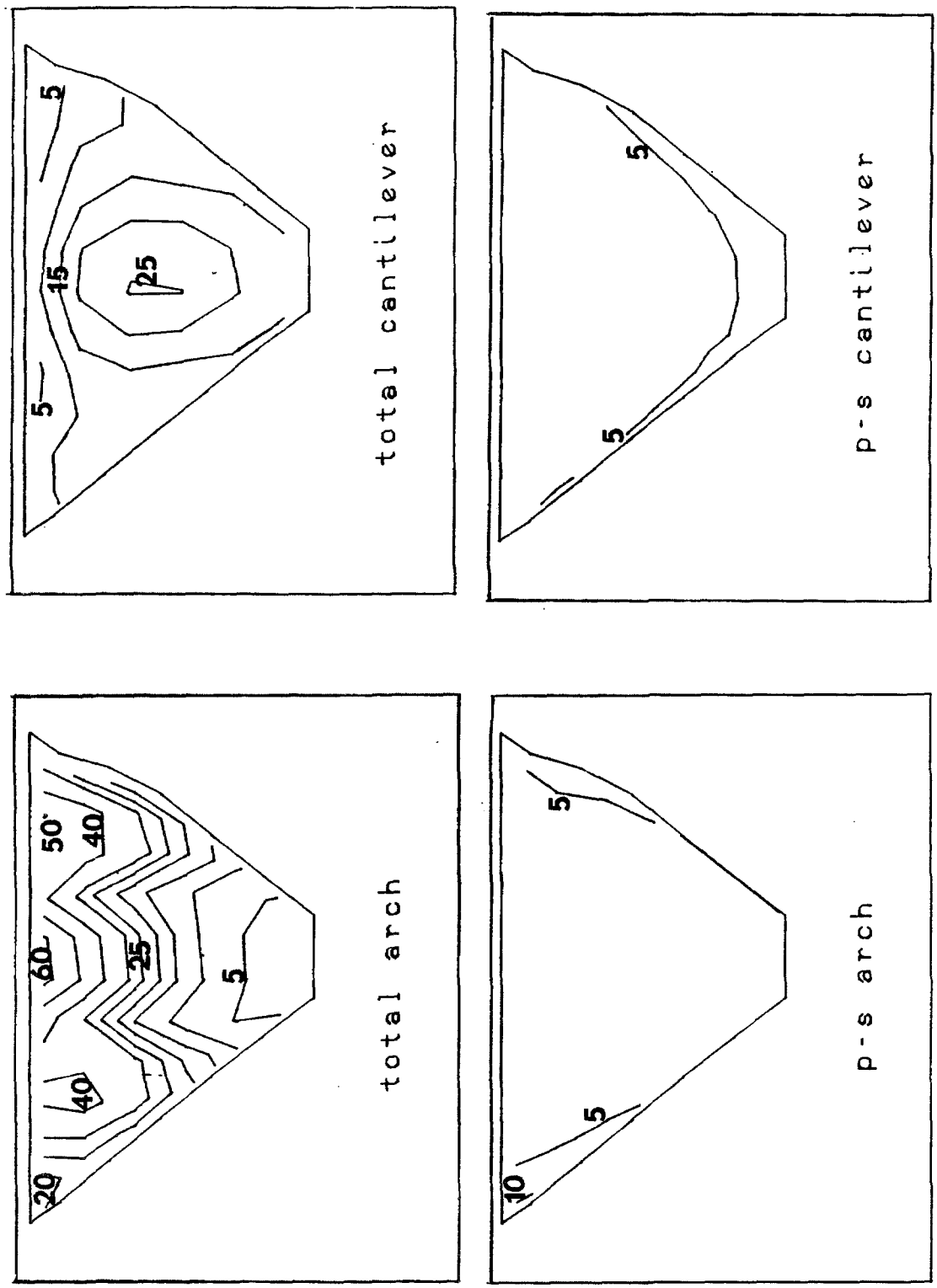

Figure 4.13b : Excitation SH0

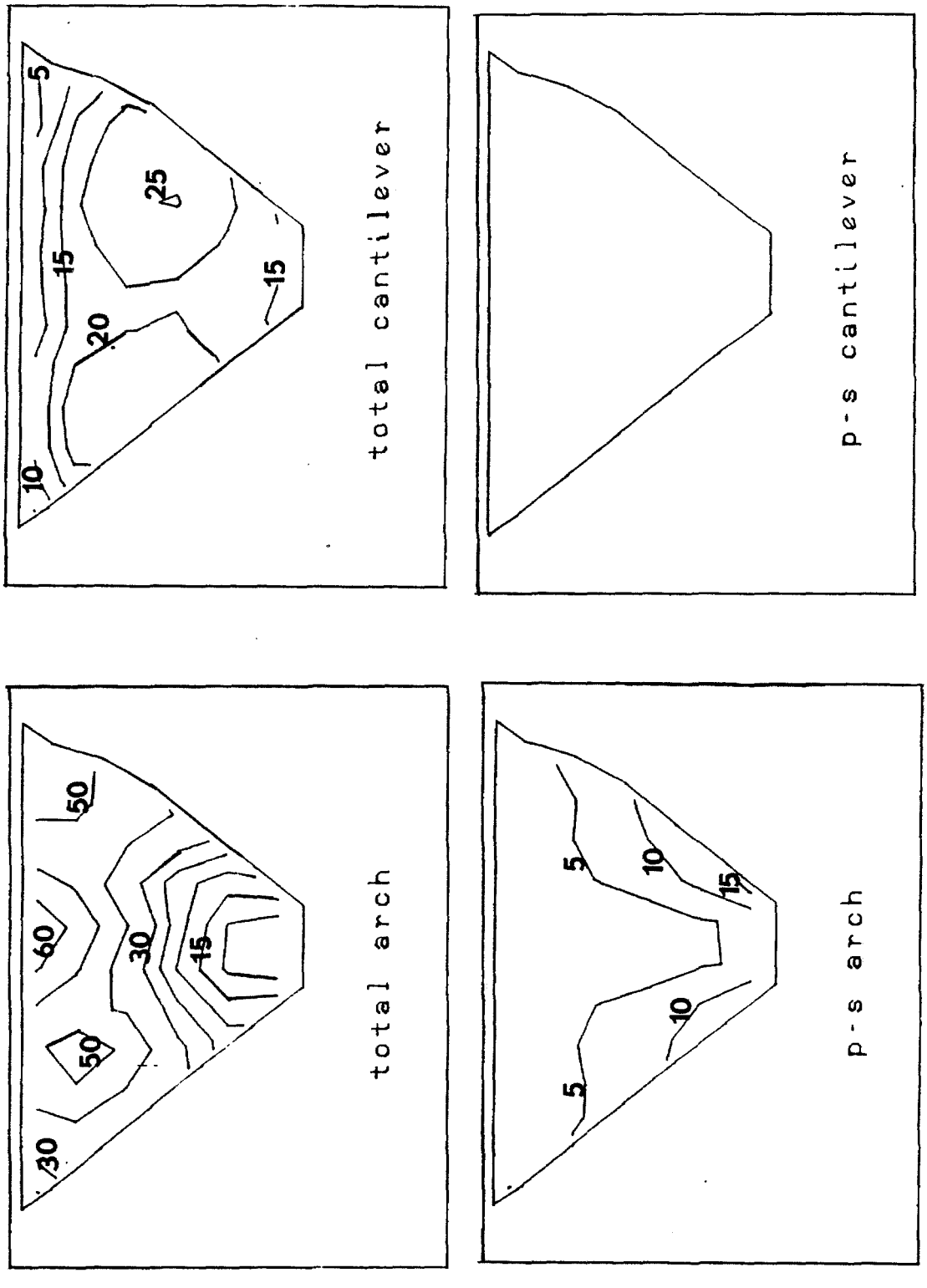

Figure 4.13c : Excitation SH60

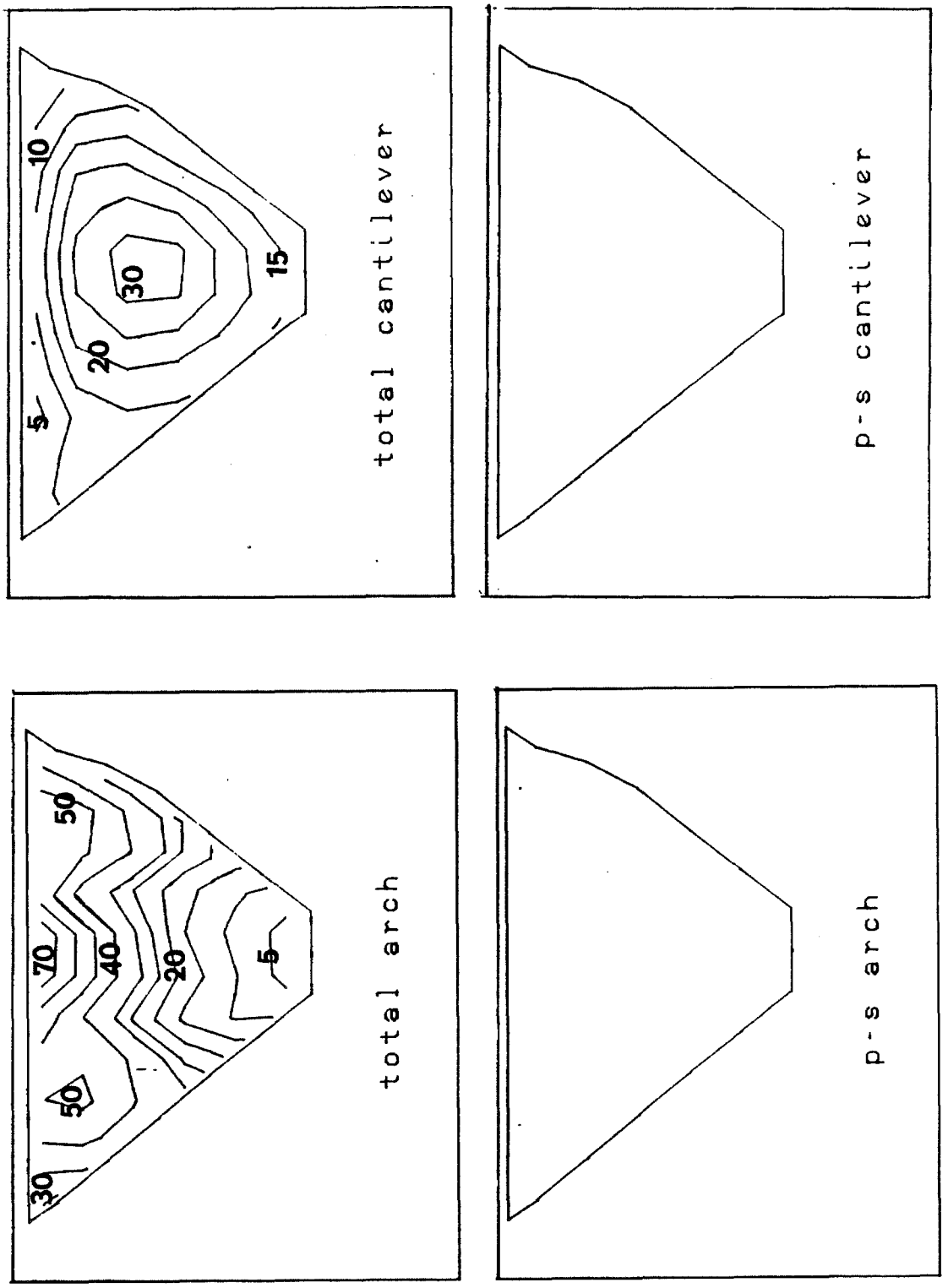

Figure 4.13d : Excitation U-CV

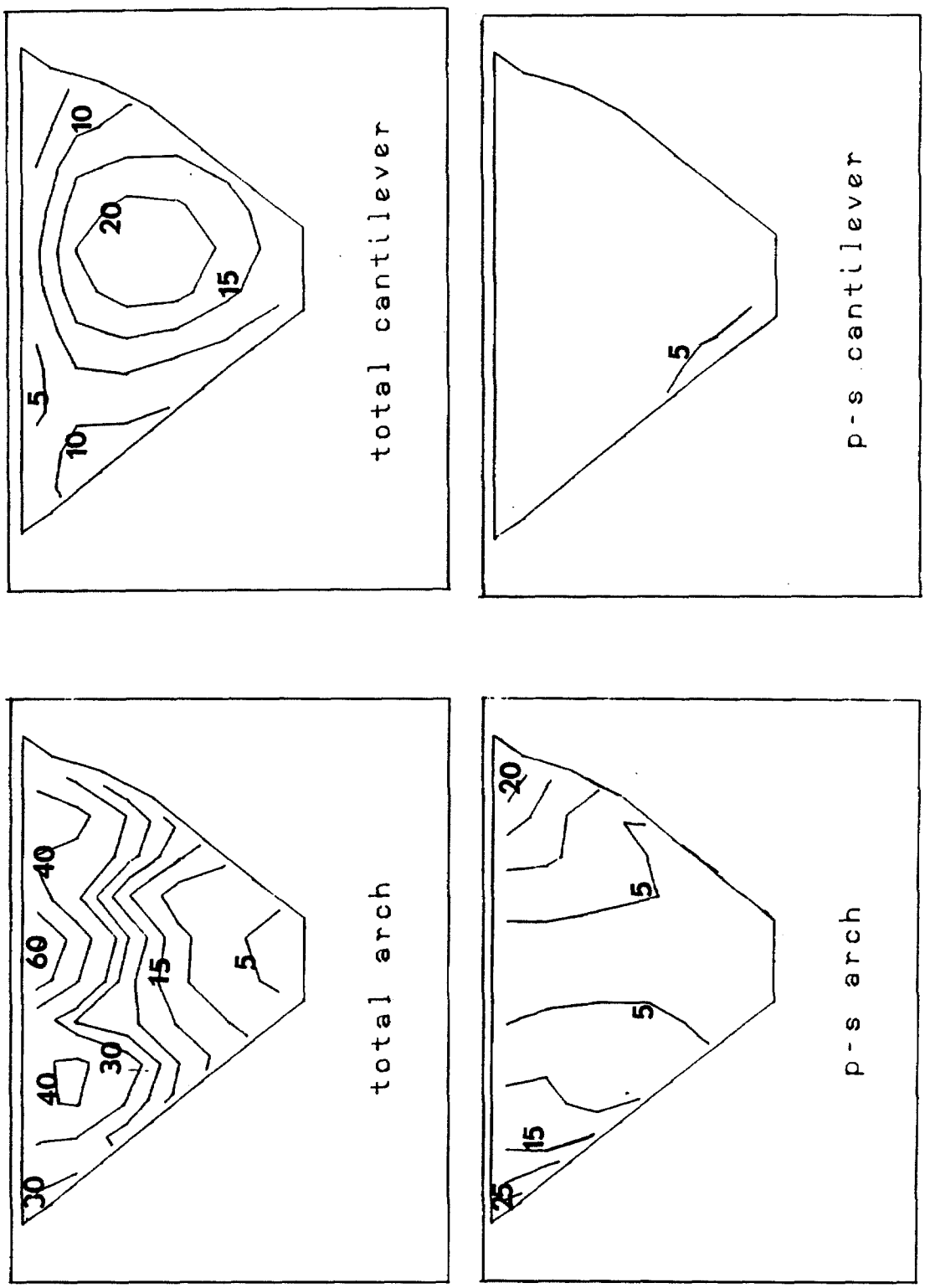

Figure 4.13e : Excitation SVP0

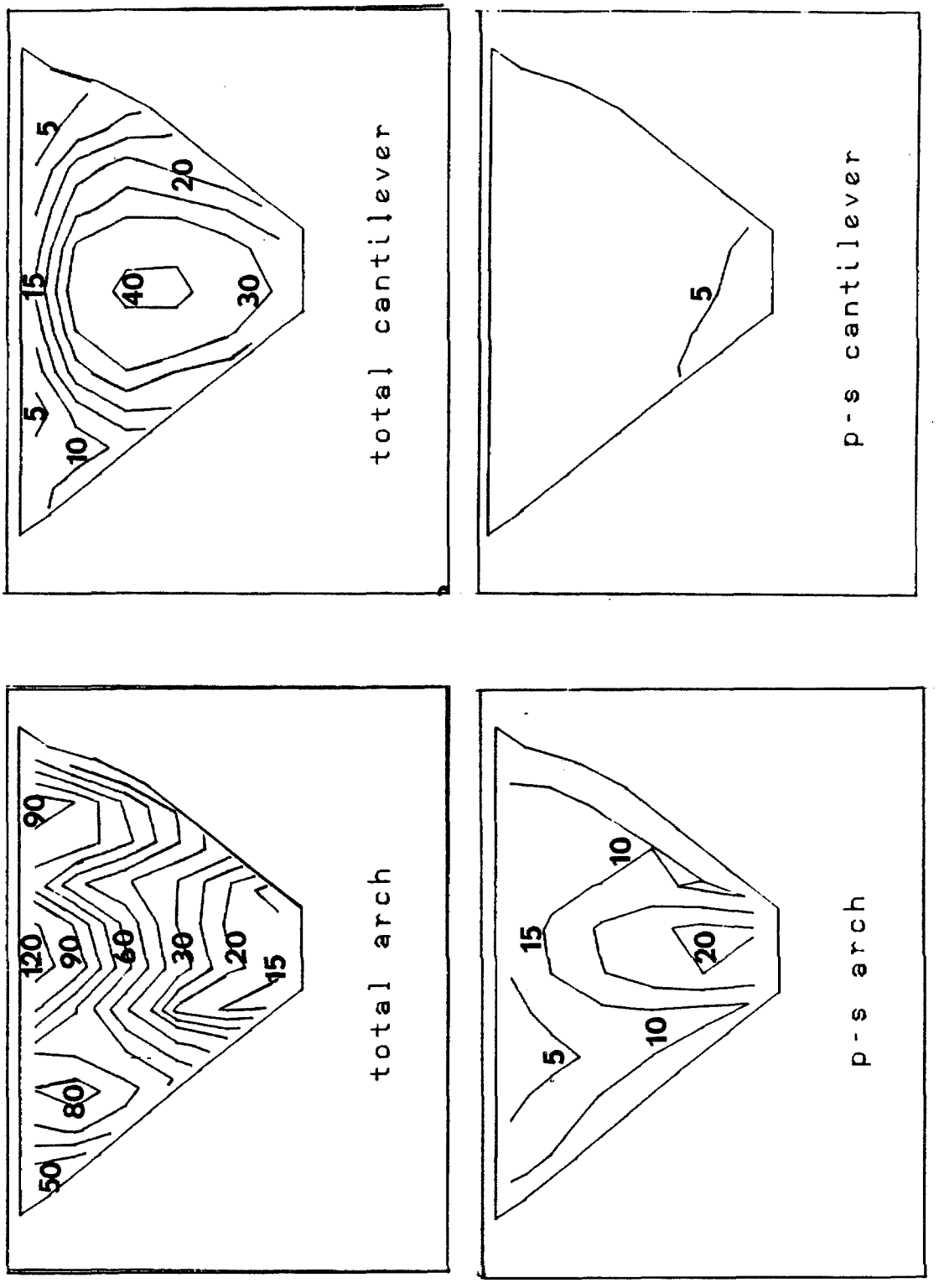

Figure 4.13f : Excitation P60

Chapter 5

Conclusions and Recommendations for Future Work

5.1 Conclusions

The boundary element method is suitable for providing the free-field solutions for incident SH, P and SV waves on a two-dimensional canyon of realistic cross section in an infinite, elastic half-space. While no claims of superiority over the method described in [41] are made, at least the present method has verified the previous one.

Response of a typical arch dam is sensitive to the input excitation mechanism. Results from the analysis of Pacoima dam suggest that incident waves produce the largest responses when arriving at angles closer to horizontal. The stress levels generated by incident SH waves (used as excitation in the stream direction) may be only 60 % to 80 % of those that are due to uniform stream motion. Effects of incident P and SV waves (used for excitation in the cross-stream and vertical directions) are more variable and have the potential for a significant increase, i.e., the P wave arriving at near horizontal incidence, as compared to the uniform excitation.

In current design and analysis practice for large arch dams in seismic zones, the free-field motions of the canyon are taken to be uniform. The results of this thesis show that this design practice may be conservative when the excitation is in

the stream direction. When the earthquake excitation is perpendicular to the stream direction, the current design methods may either overestimate or underestimate the actual stresses within the dam.

5.2 Future Work

The current study treats the earthquake as plane body waves normally incident to the axis of a canyon which is assumed uniform in cross-section and contained in an infinite, elastic, isotropic, homogeneous half-space. Although this idealization is rather severe, a more general problem (other than the addition of incident Rayleigh waves, which is straightforward) is much more complicated. Probably, the most useful, next step would be to conduct a frequency domain comparison of the motions generated by the present model with those recorded during actual earthquakes.

Any user of the present model in practice faces the decision of what combination of waves at what angles of incidence to use. At the start of this study, it was anticipated that nonuniform seismic input would always reduce the dam response compared to that under uniform excitation, and that significant benefit could still be gained by using a worst-case specification of incident waves and angles. Such, however, is not the case, so some intelligent choice must be made. Perhaps, the results of the comparison to actual earthquake motions mentioned above will provide some guidelines.

One parameter associated with the present model that deserves further study is the amount of the canyon above the level of the dam crest to include in the boundary element discretization. For the Pacoima canyon employed in Chapter 4, the extent of the actual canyon above the dam was much greater than that included in the model. It is anticipated that results would be sensitive to this parameter, and further

investigation should be carried out.

Free-field motions generated by the current technique can also be employed in seismic analysis of long-span bridges over deep canyons. An investigation of Pine Valley bridge near San Diego, California, is planned for the near future.

References

[1] *CSIMP Strong Motion Records from the Whittier, California Earthquake of 1 October 1987*, California Division of Mines and Geology, Office of Strong Motions Studies, Report OSMS 87-05, 1987.

[2] M. Abramowitz and I. A. Stegun. *Handbook of Mathematical Functions.* Dover Publications, Inc., New York, 1964.

[3] J. D. Achenbach. *Wave Propagation in Elastic Solids.* North Holland Publishing Company, Amsterdam, 1973.

[4] P. K. Banerjee and R. Butterfield. *Boundary Element Methods in Engineering Science.* McGraw-Hill Book Company (UK), 1981.

[5] F. Calciati et al. Experience gained during in situ artificial and natural dynamic excitation of large concrete dams in Italy: analytical interpretation of results. In *Proceedings of the 13th International Congress on Large Dams*, Question 51, New Delhi, 1979.

[6] A. Castoldi. *Contributions of the Surveillance to the Evaluation of the Seismic Efficiency of Dams. Example of Ambiesta Dam.* Report No. 112, ISMES, Bergamo, 1978.

[7] A. Castoldi. New criteria for the seismic monotoring of dams: a dynamic active surveillance system. In *Proceedings of China-U.S. Workshop on Earthquake*

Behavior of Arch Dams, Beijing, 1987.

[8] S. C. Chang et al. *A Study on Seismic Response of Te-Chi Arch Dam.* Center for Earthquake Engineering Research 2, National Tiawan University, August 1987.

[9] H. Chen and S. Hou. Effect of seismic travelling wave on the response of arch dam. In *Proceedings of China-U.S. Workshop on Earthquake Behavior of Arch Dams*, Beijing, 1987.

[10] R. W. Clough et al. *ADAP-A Computer Program for Static and Dynamic Analysis of Arch Dams.* Earthquake Engineering Research Center Report No. EERC 73-14, University of California, Berkeley, California, June 1973.

[11] R. W. Clough et al. *Dynamic Interaction Effects in Arch Dams.* Earthquake Engineering Research Center Report No. UCB/EERC-85/11, University of California, Berkeley, California, October 1985.

[12] G. Dasgupta and A. K. Chopra. *Dynamic Stiffness Matrices for Homogeneous Viscoelastic Halfplanes.* Earthquake Engineering Research Center Report No. UCB/EERC-77/26, University of California, Berkeley, California, October 1977.

[13] M. J. Dowling. *Nonlinear Seismic Analysis of Arch Dams.* Earthquake Engineering Research Laboratory Report EERL 87-03, California Institute of Technology, Pasadena, California, 1987.

[14] A. A. Dumanoglu and R. T. Severn. Dynamic response of dams and other structures to differential ground motions. *Proceeding of the Institution of Civil Engineers*, September 1984.

[15] Z. H. Duron. *Experimental and Finite Element Studies of a Large Arch Dam.* Earthquake Engineering Research Laboratory Report EERL 87-02, California Institute of Technology, Pasadena, California, September 1987.

[16] A. C. Eringen and E. S. Suhubi. *Elastodynamics.* Volume 2, Academic Press, New York, 1975.

[17] W. M. Ewing et al. *Elastic Waves in Layered Media.* McGraw-Hill Book Company, New York, 1957.

[18] F. J. Sanchez-Sesma, M. A. Bravo and I. Herrera. Surface motion of topographical irregularities for incident P, SV and Rayleigh waves. *Bulletin of the Seismological Society of America*, 75(1):263–269, February 1985.

[19] K.-L. Fok and A. K. Chopra. Earthquake analysis of arch dams including dam-water interaction, reservoir boundary absorption and foundation flexibility. *Earthquake Engineering and Structural Dynamics*, March-April 1986.

[20] J. F. Hall. The dynamic and earthquake behavior of concrete dams: review of experimental behavior and observational evidence. *Soil Dynamics and Earthquake Engineering*, 7(2):58–121, April 1988.

[21] J. F. Hall. Study of the earthquake response of Pine Flat dam. *Earthquake Engineering and Structural Dynamics*, March-April 1986.

[22] J. F. Hall and A. K. Chopra. Dynamic analysis of arch dams including hydrodynamic effects. *Journal of Engineering Mechanics*, 109(1):149–167, February 1983.

[23] J. F. Hall and A. K. Chopra. *Dynamic Response of Embankment Concrete-Gravity and Arch Dams Including Hydrodynamic Interaction.* Earthquake Engineering Research Center Report No. UCB/EERC-80/39, University of California, Berkeley, California, October 1980.

[24] W. V. Mickey et al. Amplification studies of the Pacoima dam from aftershocks of the San Fernando earthquake. In *Proceedings of the 5th World Conference on Earthquake Engineering*, Rome, 1974.

[25] M. Nose. Observation and measurement of dynamic behavior of the Kurobe dam. In *Proceedings of the 10th International Congress on Large Dams*, Communication, Montreal, 1970.

[26] S. Okamoto. *Introduction to Earthquake Engineering.* University of Tokyo Press, Tokyo, 2nd edition, 1984.

[27] S. Okamoto et al. *Dynamic Behavior of an Arch Dam During Earthquakes.* Technical Report 2, Report of the Institute of Industrial Science, University of Tokyo, December 1964.

[28] S. Okamoto et al. Observations of dams during earthquakes. In *Proceedings of the 8th International Congress on Large Dams*, Question 29, Edinburgh, 1964.

[29] E. G. Prater and M. Weiland. Hydrodynamic pressures on dams. In D. N. Naylor et al., editors, *Criteria and Assumptions for Numerical Analysis of Dams*, Swansea, September 1975.

[30] R. F. Vogt, J. P. Wolf and H. Bachmann. Wave scattering by a canyon of arbitrary shape in a layered half-space. *Earthquake Engineering and Structural Dynamics*, 16(6):803–812, August 1988.

[31] R. W. Clough, K.-T. Chang et al. *Dynamic Response Behavior of Quan Shui Dam.* Earthquake Engineering Research Center Report No. UCB/EERC 84/20, University of California, Berkeley, California, November 1984.

[32] R. W. Clough, K.-T. Chang, et al. *Dynamic Response Behavior of Xiang Hong Dian Dam.* Earthquake Engineering Research Center Report No. UCB/EERC 84/02, University of California, Berkeley, California, April 1984.

[33] R. W. Clough, Y. Ghanaat and X.-F. Qiu. *Dynamic Reservoir Interaction with Monticello Dam.* Earthquake Engineering Research Center Report No. UCB/EERC-87/21, University of California, Berkeley, California, December 1987.

[34] F. J. Sanchez-Sesma and E. Rosenbluth. Ground motion at canyons of arbitrary shape under incident SH waves. *Earthquake Engineering and Structural Dynamics*, 7(5):441–450, September-October 1979.

[35] T. Fujii, K. Egawa and I. Katayama. Dynamic behavior of Nagawado arch dam in the event of 1984 Naganoken Seibu earthquake. *Earthquake Spectra*, 3(2), Earthquake Engineering Research Institute, May 1987.

[36] S. P. Timoshenko and J. N. Goodier. *Theory of Elasticity.* McGraw-Hill Book Company, New York, 3rd edition, 1934.

[37] M. D. Trifunac. Preliminary empirical model for scaling Fourier amplitude spectra of strong ground acceleration in terms of earthquake magnitude, source-to-station distance, and recording site conditions. *Bulletin of the Seismological Society of America*, 66(4):1343–1373, August 1976.

[38] M. D. Trifunac. Scattering of plane SH waves by a semi-cylindrical canyon. *Earthquake Engineering and Structural Dynamics*, 1(3):276–281, January-March 1973.

[39] A. Flores Victoria et al. Hydrodynamic pressures generated by vertical earthquake component. In *Proceedings of the 4th World Conference on Earthquake Engineering*, Santiago, 1969.

[40] M. Weiland. Earthquake resistance of a gravity dam-reservoir-foundation system. In *Proceedings of the 6th European Conference on Earthquake Engineering*, Dubrovnik, Yugoslavia, 1978.

[41] H. L. Wong. *Diffraction of P, SV, and Rayleigh Waves by Surface Topographies.* Report CE 79-05, University of Southern California, Los Angeles, California, January 1979.

[42] H. L. Wong. Effect of surface topography on the diffraction of P, SV and Rayleigh waves. *Bulletin of the Seismological Society of America*, 72(4):1167–1183, August 1982.

[43] H. L. Wong and P. C. Jennings. Effect of canyon topography on strong ground motion. *Bulletin of the Seismological Society of America*, 65(5):1239–1257, October 1975.

[44] H. L. Wong and M. D. Trifunac. Scattering of plane SH waves by a semi-elliptical canyon. *Earthquake Engineering and Structural Dynamics*, 3(2):157–169, October-December 1974.

[45] G. Zhang et al. A new seismic wave input procedure for arch dam foundations.

In *Proceedings of China-U.S. Workshop on Earthquake Behavior of Arch Dams*, Beijing, 1987.

[46] X. Zhang and J. Mai. Vibration-response of arch dams with time-lag between abutments. In *International Symposium on Earthquakes and Dams*, Volume 1, ICOLD, Beijing, 1987.

Appendix A

Notation for Appendices

A, A_n = amplitude of wave

C_1 = $-1/(4\pi(1-\nu))$

C_2 = $(1-2\,\nu)$

C_p = P wave speed = $\sqrt{(\lambda+2\mu)/\rho}$

C_s = shear wave speed = $\sqrt{\mu/\rho}$

$H_0^{(1)}(\eta)$ = first Hankel function of order 0 $= J_0(\eta) + i\,Y_0(\eta)$

i = $\sqrt{-1}$

$J_0(\eta)$ = Bessel function of the first kind of order 0

$J_1(\eta)$ = Bessel function of the first kind of order 1

K_p = P wave number = ω/C_p

K_s = shear wave number = ω/C_s

n = type of wave

r_s = radial distance from application of line source

= $\sqrt{(x-x_s)^2+(y-y_s)^2)}$

t = time

T_x, T_y, T_z = traction components

u_x, u_y, u_z = displacement components

x, y, z = coordinates of response point

x_s, y_s, z_s = coordinates of source point

$Y_0(\eta)$ = Bessel function of the second kind of order 0

$Y_1(\eta)$ = Bessel function of the second kind of order 1

α = $\sqrt{(\beta^2 - 1)}$

negative root if $\beta < 1$ and positive root if $\beta \geq 1$

β = spatial Fourier transform parameter

= (shear wave length / transform wavelength)

β_r = β with the transform wavelength equal to the Rayleigh wavelength

χ = $\kappa^{-1} = (C_s/C_p)$

Δ = small increment of β

η = $K_s r_s$

γ = $\sqrt{(\beta^2 - \chi^2)}$

negative root if $\beta < \chi$ and positive root if $\beta \geq \chi$

Γ = boundary (surface)

κ = material constant = (C_p/C_s)

λ = Lamé constant

μ = Shear modulus

ν = Poisson ratio

ω = frequency (radians per second)

Ω^c = domain of half-space with canyon present

Ω^h = domain of half-space without canyon

ρ = density

ϕ = angular component from point x_s, y_s

ϕ_i = orientation angle of element i

σ_{kl} = stress components, $kl = xx, xy, yy, zx, zy$

θ, θ_n = propagation angle of wave

Appendix B

Incident Wave Solutions in a Half-Space

Solutions for incident waves in an elastic half-space [3]. All time variations are harmonic at $\exp(-i\omega t)$.

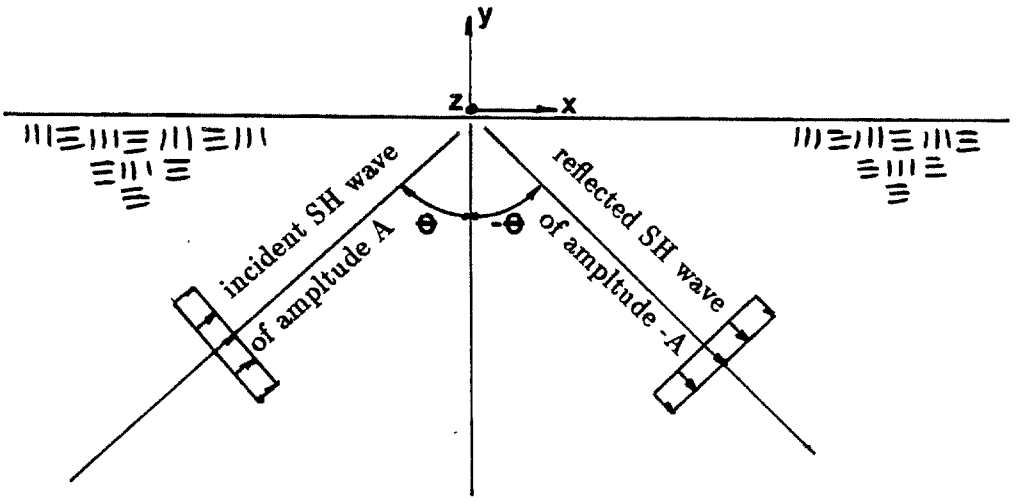

B.1 Displacements and stresses for the SH wave

$$u_z^{\mathrm{I}} = 2\,A\,\cos\left(K_s\,y\,\cos\theta\right)\,\exp\left(i\,K_s\,x\,\sin\theta\right) \tag{B.1}$$

$$\sigma_{zx}^{\mathrm{I}} = 2\,A\,i\,\mu\,K_s\,\sin\theta\,\cos\left(K_s\,y\,\cos\theta\right)\,\exp\left(i\,K_s\,x\,\sin\theta\right) \tag{B.2}$$

$$\sigma_{zy}^{\mathrm{I}} = -2\,A\,\mu\,K_s\,\cos\theta\,\sin\left(K_s\,y\,\cos\theta\right)\,\exp\left(i\,K_s\,x\,\sin\theta\right) \tag{B.3}$$

B.2 Displacements and stresses for P and SV waves

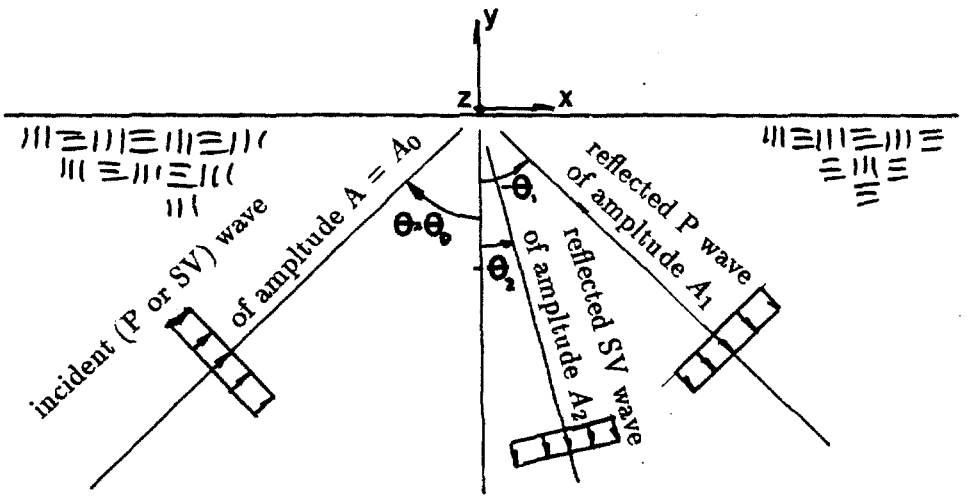

$$u_i^{\mathrm{I}} = \sum_{n=0}^{2} u_i^{(n)} \qquad i = x, y \tag{B.4}$$

$$\sigma_{ij}^{\mathrm{I}} = \sum_{n=0}^{2} \sigma_{ij}^{(n)} \qquad ij = xx, xy, yy \tag{B.5}$$

where

$$u_x^{(n)} = A_n\, d_x^{(n)} \exp(i\eta_n) \tag{B.6}$$

$$u_y^{(n)} = A_n\, d_y^{(n)} \exp(i\eta_n) \tag{B.7}$$

$$\sigma_{xx}^{(n)} = iK_nA_n \left[(\lambda + 2\mu) d_x^{(n)} q_x^{(n)} + \lambda d_y^{(n)} q_y^{(n)}\right] \exp(i\eta_n) \tag{B.8}$$

$$\sigma_{xy}^{(n)} = iK_nA_n\mu \left[d_y^{(n)} q_x^{(n)} + d_x^{(n)} q_y^{(n)}\right] \exp(i\eta_n) \tag{B.9}$$

$$\sigma_{yy}^{(n)} = iK_nA_n \left[(\lambda + 2\mu) d_y^{(n)} q_y^{(n)} + \lambda d_x^{(n)} q_x^{(n)}\right] \exp(i\eta_n) \tag{B.10}$$

and

$$\eta_n = K_n \left(x q_x^{(n)} + y q_y^{(n)}\right) \tag{B.11}$$

$n = 0$ for the incident wave (P or SV)

$n = 1$ for the reflected P wave

$n = 2$ for the reflected SV wave

$q_x^{(n)}$, $q_y^{(n)}$ = x and y components of the unit vector in the direction of propagation of the wave n

$d_x^{(n)}$, $d_y^{(n)}$ = x and y components of the unit vector along the direction of particle motion for the wave n

and, for the incident P wave,

$$\frac{A_1}{A_0} = \frac{\sin(2\theta_0)\,\sin(2\theta_2) - \kappa^2\cos^2(2\theta_2)}{\sin(2\theta_0)\,\sin(2\theta_2) + \kappa^2\cos^2(2\theta_2)} \tag{B.12}$$

$$\frac{A_2}{A_0} = \frac{2\kappa\sin(2\theta_0)\,\cos(2\theta_2)}{\sin(2\theta_0)\,\sin(2\theta_2) + \kappa^2\cos^2(2\theta_2)} \tag{B.13}$$

$$\theta_1 = -\theta_0 \tag{B.14}$$

$$-\sin\theta_2 = \kappa^{-1}\sin\theta_0 \tag{B.15}$$

and, for the incident SV wave,

$$\frac{A_1}{A_0} = \frac{-\kappa\sin(4\theta_0)}{\sin(2\theta_0)\,\sin(2\theta_1) + \kappa^2\cos^2(2\theta_0)} \tag{B.16}$$

$$\frac{A_2}{A_0} = \frac{\sin(2\theta_0)\,\sin(2\theta_1) - \kappa^2\cos^2(2\theta_0)}{\sin(2\theta_0)\,\sin(2\theta_1) + \kappa^2\cos^2(2\theta_0)} \tag{B.17}$$

$$\theta_2 = -\theta_0 \tag{B.18}$$

$$-\sin\theta_1 = \kappa\sin\theta_0 \tag{B.19}$$

$$\theta_0 \leq \theta_{cr} = \sin^{-1}(\kappa^{-1}) \tag{B.20}$$

where θ_{cr} = the critical angle for the incident SV wave beyond which the reflected waves attenuate and become complex.

Appendix C

Solutions for Displacements and Stresses due to Line Load and Image in the Full-space

Reference [16].

Note : S.T.$(+y_s)$ means similar term but with $+y_s$ replacing $-y_s$ (including the expressions for r_s and η).

C.1 Antiplane shear : $\delta_z(x-x_s, y-y_s)$ and $\delta_z(x-x_s, y+y_s)$

$$u_z = \frac{i}{4\mu} H_0^{(1)}(\eta) + \text{S.T.}(+y_s) \tag{C.1}$$

$$\sigma_{zx} = -\frac{iK_s}{4}\frac{x-x_s}{r_s} H_1^{(1)}(\eta) + \text{S.T.}(+y_s) \tag{C.2}$$

$$\sigma_{zy} = -\frac{iK_s}{4}\frac{y-y_s}{r_s} H_1^{(1)}(\eta) + \text{S.T.}(+y_s) \tag{C.3}$$

C.2 Plane strain : $\delta_x(x-x_s, y-y_s)$ and $\delta_{-x}(x-x_s, y+y_s)$

$$\begin{aligned} u_x^A = & \left(\frac{i}{4\rho C_p^2}\right)\left\{\left(\frac{x-x_s}{r_s}\right)^2 H_0^{(1)}(\eta) + \kappa^2\left(\frac{y-y_s}{r_s}\right)^2 H_0^{(1)}(\kappa\eta) + \right. \\ & \left.\frac{1}{\eta}\left(1-2\left(\frac{x-x_s}{r_s}\right)^2\right)\left(H_1^{(1)}(\eta) - \kappa H_1^{(1)}(\kappa\eta)\right)\right\} - \text{S.T.}(+y_s) \end{aligned} \tag{C.4}$$

$$u_y^A = \left(\frac{i}{4\rho C_p^2}\right)\left(\frac{(x-x_s)(y-y_s)}{r_s^2}\right)$$

$$\left\{H_0^{(1)}(\eta)-\kappa^2 H_0^{(1)}(\kappa\eta)-\frac{2}{\eta}\left(H_1^{(1)}(\eta)-\kappa H_1^{(1)}(\kappa\eta)\right)\right\}-\text{ S.T.}(+y_s) \quad \text{(C.5)}$$

$$\begin{aligned}\sigma_{xx}^A &= \left(\frac{i\omega(x-x_s)}{4C_p^3\rho r_s}\right)\Big[-\lambda H_1^{(1)}(\eta)+ \\ &\quad 2\mu\left\{\left(\frac{3(y-y_s)^2-(x-x_s)^2}{r_s^2}\right)\frac{1}{\eta}\left(H_0^{(1)}(\eta)-\kappa^2 H_0^{(1)}(\kappa\eta)\right)\right. \\ &\quad -2\left(\frac{3(y-y_s)^2-(x-x_s)^2}{r_s^2}\right)\frac{1}{\eta^2}\left(H_1^{(1)}(\eta)-\kappa H_1^{(1)}(\kappa\eta)\right) \\ &\quad \left.-\left(\frac{x-x_s}{r_s}\right)^2 H_1^{(1)}(\eta)-\left(\frac{y-y_s}{r_s}\right)^2\kappa^3 H_1^{(1)}(\kappa\eta)\right\}\Big]-\text{S.T.}(+y_s) \quad \text{(C.6)}\end{aligned}$$

$$\begin{aligned}\sigma_{xy}^A &= \left(\frac{i\omega(y-y_s)}{4C_p^3\rho r_s}\right)\mu\left\{-2\left(\frac{3(x-x_s)^2-(y-y_s)^2}{r_s^2}\right)\frac{1}{\eta}\left(H_0^{(1)}(\eta)-\kappa^2 H_0^{(1)}(\kappa\eta)\right)\right. \\ &\quad +4\left(\frac{3(x-x_s)^2-(y-y_s)^2}{r_s^2}\right)\frac{1}{\eta^2}\left(H_1^{(1)}(\eta)-\kappa H_1^{(1)}(\kappa\eta)\right) \\ &\quad \left.+\left(\frac{(x-x_s)^2-(y-y_s)^2}{r_s^2}\right)\kappa^3 H_1^{(1)}(\kappa\eta)-2\left(\frac{x-x_s}{r_s}\right)^2 H_1^{(1)}(\eta)\right\} \\ &\quad -\text{S.T.}(+y_s) \quad \text{(C.7)}\end{aligned}$$

$$\begin{aligned}\sigma_{yy}^A &= \left(\frac{i\omega(x-x_s)}{4C_p^3\rho r_s}\right)\Big[-\lambda H_1^{(1)}(\eta)+ \\ &\quad 2\mu\left\{-\left(\frac{3(y-y_s)^2-(x-x_s)^2}{r_s^2}\right)\frac{1}{\eta}\left(H_0^{(1)}(\eta)-\kappa^2 H_0^{(1)}(\kappa\eta)\right)\right. \\ &\quad +2\left(\frac{3(y-y_s)^2-(x-x_s)^2}{r_s^2}\right)\frac{1}{\eta^2}\left(H_1^{(1)}(\eta)-\kappa H_1^{(1)}(\kappa\eta)\right) \\ &\quad \left.-\left(\frac{y-y_s}{r_s}\right)^2\left(H_1^{(1)}(\eta)-\kappa^3 H_1^{(1)}(\kappa\eta)\right)\right\}\Big]-\text{S.T.}(+y_s) \quad \text{(C.8)}\end{aligned}$$

C.3 Plane strain : $\delta_y(x-x_s, y-y_s)$ and $\delta_{-y}(x-x_s, y+y_s)$

$$\begin{aligned}u_x^A &= \left(\frac{i}{4\rho C_p^2}\right)\left(\frac{(x-x_s)(y-y_s)}{r_s^2}\right) \\ &\quad \left\{H_0^{(1)}(\eta)-\kappa^2 H_0^{(1)}(\kappa\eta)-\frac{2}{\eta}\left(H_1^{(1)}(\eta)-\kappa H_1^{(1)}(\kappa\eta)\right)\right\}-\text{S.T.}(+y_s) \quad \text{(C.9)}\end{aligned}$$

$$u_y^A = \left(\frac{i}{4\rho C_p^2}\right)\left\{\left(\frac{y-y_s}{r_s}\right)^2 H_0^{(1)}(\eta) + \kappa^2\left(\frac{x-x_s}{r_s}\right)^2 H_0^{(1)}(\kappa\eta) + \frac{1}{\eta}\left(1-2\left(\frac{y-y_s}{r_s}\right)^2\right)\left(H_1^{(1)}(\eta) - \kappa H_1^{(1)}(\kappa\eta)\right)\right\} - \text{S.T.}(+y_s) \quad \text{(C.10)}$$

$$\sigma_{xx}^A = \left(\frac{i\omega(y-y_s)}{4C_p^3\rho r_s}\right)\Big[-\lambda H_1^{(1)}(\eta) + 2\mu\left\{-\left(\frac{3(x-x_s)^2-(y-y_s)^2}{r_s^2}\right)\frac{1}{\eta}\left(H_0^{(1)}(\eta) - \kappa^2 H_0^{(1)}(\kappa\eta)\right) + 2\left(\frac{3(x-x_s)^2-(y-y_s)^2}{r_s^2}\right)\frac{1}{\eta^2}\left(H_1^{(1)}(\eta) - \kappa H_1^{(1)}(\kappa\eta)\right) - \left(\frac{x-x_s}{r_s}\right)^2\left(H_1^{(1)}(\eta) - \kappa^3 H_1^{(1)}(\kappa\eta)\right)\right\}\Big] - \text{S.T.}(+y_s) \quad \text{(C.11)}$$

$$\sigma_{xy}^A = \left(\frac{i\omega(x-x_s)}{4C_p^3\rho r_s}\right)\mu\left\{-2\left(\frac{3(y-y_s)^2-(x-x_s)^2}{r_s^2}\right)\frac{1}{\eta}\left(H_0^{(1)}(\eta) - \kappa^2 H_0^{(1)}(\kappa\eta)\right) + 4\left(\frac{3(y-y_s)^2-(x-x_s)^2}{r_s^2}\right)\frac{1}{\eta^2}\left(H_1^{(1)}(\eta) - \kappa H_1^{(1)}(\kappa\eta)\right) + \left(\frac{(y-y_s)^2-(x-x_s)^2}{r_s^2}\right)\kappa^3 H_1^{(1)}(\kappa\eta) - 2\left(\frac{y-y_s}{r_s}\right)^2 H_1^{(1)}(\eta)\right\} - \text{S.T.}(+y_s) \quad \text{(C.12)}$$

$$\sigma_{yy}^A = \left(\frac{i\omega(y-y_s)}{4C_p^3\rho r_s}\right)\Big[-\lambda H_1^{(1)}(\eta) + 2\mu\left\{\left(\frac{3(x-x_s)^2-(y-y_s)^2}{r_s^2}\right)\frac{1}{\eta}\left(H_0^{(1)}(\eta) - \kappa^2 H_0^{(1)}(\kappa\eta)\right) - 2\left(\frac{3(x-x_s)^2-(y-y_s)^2}{r_s^2}\right)\frac{1}{\eta^2}\left(H_1^{(1)}(\eta) - \kappa H_1^{(1)}(\kappa\eta)\right) - \left(\frac{y-y_s}{r_s}\right)^2 H_1^{(1)}(\eta) - \left(\frac{x-x_s}{r_s}\right)^2 \kappa^3 H_1^{(1)}(\kappa\eta)\right\}\Big] - \text{S.T.}(+y_s) \quad \text{(C.13)}$$

Appendix D

Evaluation of the Inverse Fourier Transform

$$g^B(x,y) = -\frac{K_s}{2\pi}\int_{-\infty}^{\infty} h(\beta,y_s)\; g(\beta,y)\; \exp\left(i\beta K_s(x-x_s)\right)\, d\beta \qquad \text{(D.1)}$$

D.1 Functions $h(\beta, y_s)$ and $\hat{g}(\beta, y)$

Function $h(\beta, y_s)$ for $T_x^A(x, y=0)$

$$h(\beta,y_s) = (2\,\beta^2 - 1)\exp\left(y_s\,K_s\,\alpha\right) - 2\,\beta^2\,\exp\left(y_s\,K_s\,\gamma\right) \qquad \text{(D.2)}$$

Function $h(\beta, y_s)$ for $T_y^A(x, y=0)$

$$h(\beta,y_s) = (2\,\beta^2 - 1)\exp\left(y_s\,K_s\,\gamma\right) - 2\,\beta^2\,\exp\left(y_s\,K_s\,\alpha\right) \qquad \text{(D.3)}$$

Functions $\hat{g}(\beta, y)$ for $T_x(x, y=0) = \exp\left(i\beta K_s x\right)$

$$\hat{u}_x(\beta,y) = \frac{\alpha}{\mu K_s}\left[(2\,\beta^2 - 1)\;\exp(y\alpha K_s) - 2\,\beta^2\;\exp(y\gamma K_s)\right] \qquad \text{(D.4)}$$

$$\hat{u}_y(\beta,y) = \frac{i\beta}{\mu K_s}\left[2\,\alpha\,\gamma\;\exp(y\gamma K_s) - (2\,\beta^2 - 1)\;\exp(y\alpha K_s)\right] \qquad \text{(D.5)}$$

$$\hat{\sigma}_{xx}(\beta,y) = 2i\beta\alpha\left[(2\,\beta^2 - 1)\;\exp(y\alpha K_s) - (2\,\gamma^2 + 1)\;\exp(y\gamma K_s)\right] \qquad \text{(D.6)}$$

$$\hat{\sigma}_{xy}(\beta,y) = (2\,\beta^2 - 1)^2\;\exp(y\alpha K_s) - 4\,\beta^2\,\alpha\,\gamma\;\exp(y\gamma K_s) \qquad \text{(D.7)}$$

$$\hat{\sigma}_{yy}(\beta, y) = 2i\beta\alpha\,(2\,\beta^2 - 1)\,[\exp(y\gamma K_s) - \exp(y\alpha K_s)] \tag{D.8}$$

Functions $\hat{g}(\beta, y)$ for $T_y(x, y = 0) = \exp(i\beta K_s x)$

$$\hat{u}_x(\beta, y) = \frac{i\beta}{\mu K_s}\left[(2\,\beta^2 - 1)\,\exp(y\gamma K_s) - 2\,\alpha\,\gamma\,\exp(y\alpha K_s)\right] \tag{D.9}$$

$$\hat{u}_y(\beta, y) = \frac{\gamma}{\mu K_s}\left[(2\,\beta^2 - 1)\,\exp(y\gamma K_s) - 2\,\beta^2\,\exp(y\alpha K_s)\right] \tag{D.10}$$

$$\hat{\sigma_{xx}}(\beta, y) = 4\,\beta^2\,\alpha\,\gamma\,\exp(y\alpha K_s) - (2\,\beta^2 - 1)\,(2\,\gamma^2 + 1)\,\exp(y\gamma K_s) \tag{D.11}$$

$$\hat{\sigma}_{xy}(\beta, y) = 2i\beta\gamma\,(2\,\beta^2 - 1)\,[\exp(y\gamma K_s) - \exp(y\alpha K_s)] \tag{D.12}$$

$$\hat{\sigma}_{yy}(\beta, y) = (2\,\beta^2 - 1)^2\,\exp(y\gamma K_s) - 4\,\beta^2\,\alpha\,\gamma\,\exp(y\alpha K_s) \tag{D.13}$$

D.2 Form for integration

With symmetric transfer function $g(\beta, y)$

$$g^B(x, y) = -\frac{K_s}{\pi}\int_0^\infty h(\beta, y_s)\,g(\beta, y)\,\cos[\beta K_s(x - x_s)]\,d\beta \tag{D.14}$$

$$
\left.
\begin{aligned}
&= -\tfrac{K_s}{\pi}\left\{\int_0^{\beta_r-\Delta} h(\beta,y_s)\,g(\beta,y)\,\cos\left[\beta K_s(x-x_s)\right]\,d\beta\right. \\
&\quad \left. + \int_{\beta_r+\Delta}^{\beta_{max}} h(\beta,y_s)\,g(\beta,y)\,\cos\left[\beta K_s(x-x_s)\right]\,d\beta\right\} \\
&\quad -\tfrac{iK_s}{R}\,h(\beta_r,y_s)\,\hat{g}(\beta_r,y)\,\cos\left[\beta_r K_s(x-x_s)\right] \\
&\quad -\tfrac{K_s}{\pi R}\left\{h(\beta_r+\Delta,y_s)\,\hat{g}(\beta_r+\Delta,y)\,\cos\left[(\beta_r+\Delta)K_s(x-x_s)\right]\right\} \\
&\quad +\tfrac{K_s}{\pi R}\left\{h(\beta_r-\Delta,y_s)\hat{g}(\beta_r-\Delta,y)\,\cos\left[(\beta_r-\Delta)K_s(x-x_s)\right]\right\}
\end{aligned}
\right\} \qquad \text{(D.15)}
$$

With antisymmetric transfer function $g(\beta,y)$

$$
g^B(x,y) = -\frac{iK_s}{\pi}\int_0^{\infty} h(\beta,y_s)\,g(\beta,y)\,\sin\left[\beta K_s(x-x_s)\right]\,d\beta \qquad \text{(D.16)}
$$

$$
\left.
\begin{aligned}
&= -\tfrac{iK_s}{\pi}\left\{\int_0^{\beta_r-\Delta} h(\beta,y_s)\,g(\beta,y)\,\sin\left[\beta K_s(x-x_s)\right]\,d\beta\right. \\
&\quad \left. + \int_{\beta_r+\Delta}^{\beta_{max}} h(\beta,y_s)\,g(\beta,y)\,\sin\left[\beta K_s(x-x_s)\right]\,d\beta\right\} \\
&\quad +\tfrac{K_s}{R}\,h(\beta_r,y_s)\,\hat{g}(\beta_r,y)\,\sin\left[\beta_r K_s(x-x_s)\right] \\
&\quad -\tfrac{iK_s}{\pi R}\left\{h(\beta_r+\Delta,y_s)\,\hat{g}(\beta_r+\Delta,y)\,\sin\left[(\beta_r+\Delta)K_s(x-x_s)\right]\right\} \\
&\quad +\tfrac{iK_s}{\pi R}\left\{h(\beta_r-\Delta,y_s)\hat{g}(\beta_r-\Delta,y)\,\sin\left[(\beta_r-\Delta)K_s(x-x_s)\right]\right\}
\end{aligned}
\right\} \qquad \text{(D.17)}
$$

where

$$
R = 4\left[2\,\beta_r\,(2\,\beta_r^2-1) - \frac{4\,\beta_r^5 - 3\,\beta_r^3(1+\chi^2) + 2\beta_r\chi^2}{\sqrt{(\beta_r^2-1)}\,\sqrt{(\beta_r^2-\chi^2)}}\right] \qquad \text{(D.18)}
$$

Appendix E

Singularities in Solutions for Line Loads

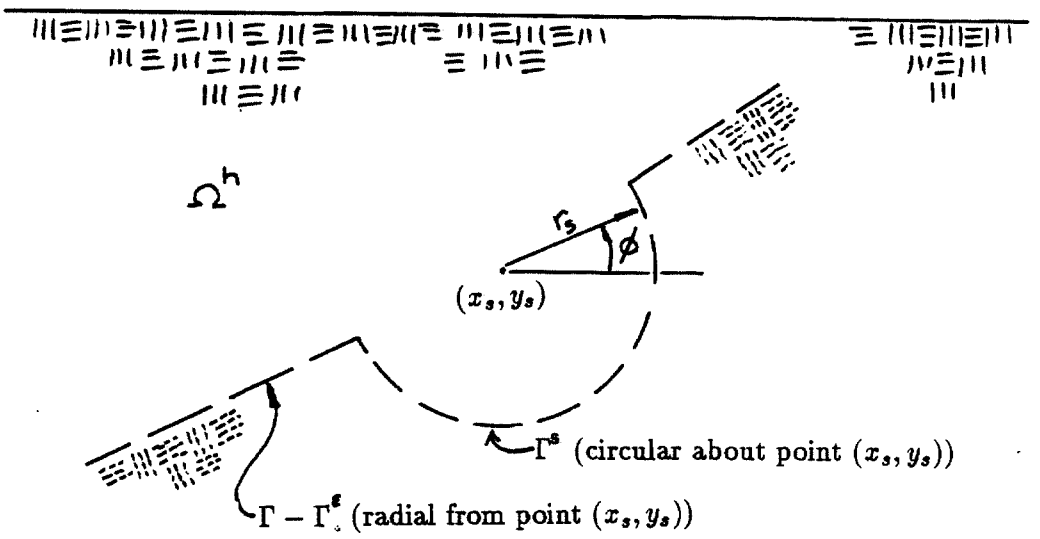

References [4,36].

Notes : $st(\ )$ denotes singular term in response quantity. $\pm$ means + when material is on the right when facing in the positive radial direction along $\Gamma - \Gamma^\epsilon$, and - when material is on the left.

E.1 Antiplane shear: $\delta_z(x - x_s, y - y_s)$

$$st(u_z) = -\frac{1}{4\mu} \ln(r_s) \tag{E.1}$$

$$st(T_z) = 0 \quad on\ \Gamma - \Gamma^\epsilon \tag{E.2}$$

$$st(T_z) = +\frac{1}{2\pi r_s} \quad on\ \Gamma^s \tag{E.3}$$

E.2 Plane strain: buried line source $\delta_x(x - x_s, y - y_s)$

$$st(u_x) = -\frac{(1+\kappa^2)}{4\pi C_p^2 \rho} \ln(r_s) \tag{E.4}$$

$$st(u_y) = 0 \tag{E.5}$$

$$st(T_x) = 0 \quad on\ \Gamma - \Gamma^\epsilon \tag{E.6}$$

$$st(T_y) = \pm\frac{-1}{2\,\pi\,\kappa^2\,r_s} \quad on\ \Gamma - \Gamma^\epsilon \tag{E.7}$$

$$st(T_x) = -\frac{C_1}{r_s}\left[C_2 + 2\cos^2\phi\right] \quad on\ \Gamma^s \tag{E.8}$$

$$st(T_y) = -2\frac{C_1}{r_s}\cos\phi\,\sin\phi \quad on\ \Gamma^s \tag{E.9}$$

E.3 Plane strain: buried line source $\delta_y(x - x_s, y - y_s)$

$$st(u_x) = 0 \tag{E.10}$$

$$st(u_y) = -\frac{(1+\kappa^2)}{4\pi C_p^2 \rho} \ln(r_s) \tag{E.11}$$

$$st(T_x) = \pm\frac{1}{2\,\pi\,\kappa^2\,r_s} \quad on\ \Gamma - \Gamma^\epsilon \tag{E.12}$$

$$st(T_y) = 0 \quad on\ \Gamma - \Gamma^\epsilon \tag{E.13}$$

$$st(T_x) = -2\frac{C_1}{r_s}\cos\phi\,\sin\phi \quad on\ \Gamma^s \tag{E.14}$$

$$st(T_y) = -\frac{C_1}{r_s}\left[C_2 + 2\sin^2\phi\right] \quad on\ \Gamma^s \tag{E.15}$$

E.4 Plane strain: line source $\delta_x(x - x_s, y - y_s)$ at horizontal surface of half-space

$$st(u_x) = -\frac{1-\nu}{\pi\mu}\ln(r_s) \tag{E.16}$$

$$st(u_y) = 0 \tag{E.17}$$

$$st(T_x) = 0 \quad on\ \Gamma - \Gamma^\epsilon \tag{E.18}$$

$$st(T_y) = 0 \quad on\ \Gamma - \Gamma^\epsilon \tag{E.19}$$

$$st(T_x) = \frac{2}{\pi r_s}cos^2\phi \quad on\ \Gamma^s \tag{E.20}$$

$$st(T_y) = \frac{2}{\pi r_s}\sin\phi\ \cos\phi \quad on\ \Gamma^s \tag{E.21}$$

E.5 Plane strain: line source $\delta_y(x - x_s, y - y_s)$ at horizontal surface of half-space

$$st(u_x) = 0 \tag{E.22}$$

$$st(u_y) = -\frac{1-\nu}{\pi\mu}\ln(r_s) \tag{E.23}$$

$$st(T_x) = 0 \quad on\ \Gamma - \Gamma^\epsilon \tag{E.24}$$

$$st(T_y) = 0 \quad on\ \Gamma - \Gamma^\epsilon \tag{E.25}$$

$$st(T_x) = \frac{2}{\pi r_s}\sin\phi\ \cos\phi \quad on\ \Gamma^s \tag{E.26}$$

$$st(T_y) = \frac{2}{\pi r_s}sin^2\phi \quad on\ \Gamma^s \tag{E.27}$$

Appendix F

Integrals Over Γ^s of Line Load Tractions

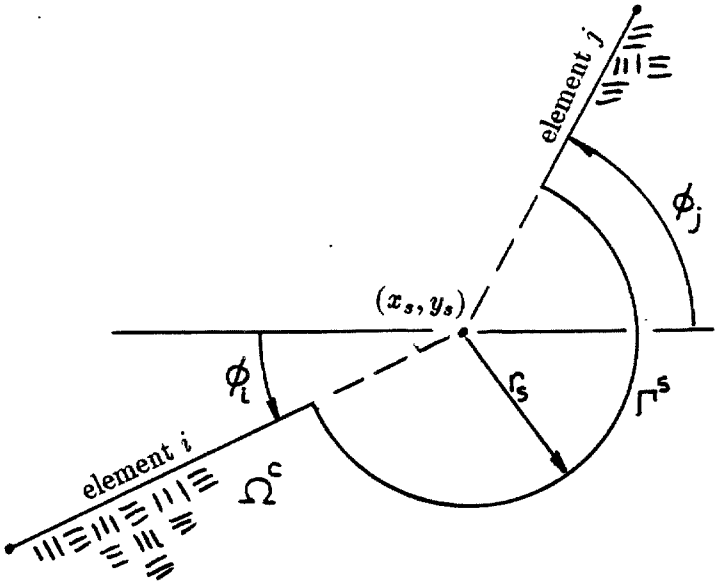

F.1 Antiplane shear: $\delta_z(x - x_s, y - y_s)$

$$\lim_{r_s \to 0} \int_{\Gamma^s} T_z \, d\Gamma^s = 0.5 + \frac{(\phi_j - \phi_i)}{2\pi} \tag{F.1}$$

F.2 Plane strain: buried line source $\delta_x(x - x_s, y - y_s)$

$$\lim_{r_s \to 0} \int_{\Gamma^s} T_x \, d\Gamma^s = 1.0 + C_1 \left[(C_2 + 1)(\pi + \phi_i - \phi_j) + \frac{1}{2}(\sin(2\phi_i) - \sin(2\phi_j)) \right] \tag{F.2}$$

$$\lim_{r_s \to 0} \int_{\Gamma^s} T_y \, d\Gamma^s = -C_1 \left(\sin^2 \phi_j - \sin^2 \phi_i \right) \tag{F.3}$$

F.3 Plane strain: buried line source $\delta_y(x - x_s, y - y_s)$

$$\lim_{r_s \to 0} \int_{\Gamma^s} T_x \, d\Gamma^s = -C_1 \left(\sin^2 \phi_j - \sin^2 \phi_i \right) \tag{F.4}$$

$$\lim_{r_s \to 0} \int_{\Gamma^s} T_y \, d\Gamma^s = 1.0 + C_1 \left[(C_2 + 1)(\pi + \phi_i - \phi_j) - \frac{1}{2}(\sin(2\phi_i) - \sin(2\phi_j)) \right] \tag{F.5}$$

F.4 Plane strain: line source $\delta_x(x - x_s, y - y_s)$ at top of canyon

$$\lim_{r_s \to 0} \int_{\Gamma^s} T_x \, d\Gamma^s = \frac{1}{\pi} \left[(\pi + \phi_1) + \frac{1}{2} \sin(2\phi_1) \right] \text{ at node 1} \tag{F.6}$$

$$= \frac{1}{\pi} \left(\pi - \phi_{n-1} - \frac{1}{2} \sin(2\phi_{n-1}) \right) \text{ at node } n-1 \tag{F.7}$$

$$\lim_{r_s \to 0} \int_{\Gamma^s} T_y \, d\Gamma^s = \frac{1}{\pi} \sin^2 \phi_1 \text{ at node 1} \tag{F.8}$$

$$= -\frac{1}{\pi} \sin^2 \phi_{n-1} \text{ at node } n-1 \tag{F.9}$$

F.5 Plane strain: line source $\delta_y(x-x_s, y-y_s)$ at top of canyon

$$\lim_{r_s \to 0} \int_{\Gamma^s} T_x \, d\Gamma^s = \frac{1}{\pi} \sin^2 \phi_1 \text{ at node 1} \tag{F.10}$$

$$= -\frac{1}{\pi} \sin^2 \phi_{n-1} \text{ at node } n-1 \tag{F.11}$$

$$\lim_{r_s \to 0} \int_{\Gamma^s} T_y \, d\Gamma^s = \frac{1}{\pi} \left[(\pi + \phi_1) - \frac{1}{2} \sin(2\phi_1) \right] \text{ at node 1} \tag{F.12}$$

$$= \frac{1}{\pi} \left(\pi - \phi_{n-1} + \frac{1}{2} \sin(2\phi_{n-1}) \right) \text{ at node } n-1 \tag{F.13}$$